Simulating Scalar Fields in Astrophysical and Cosmological Settings

Elley, Matthew

Awarding institution:
King's College London

Ph.D. Thesis

Simulating Scalar Fields in Astrophysical and Cosmological Settings

Matthew Elley

King's College London
Theoretical Particle Physics and Cosmology group
Department of Physics
Supervisor: Prof. Eugene Lim

This thesis is submitted for the degree of *Doctor of Philosophy*

28/06/2023

Acknowledgements

I am incredibly thankful to Eugene Lim for the support, assistance and discussions he provided as my supervisor during the final stages of my PhD. I am also grateful for assistance given by members of the GRChombo community, in particular Josu Aurrekoetxea and Katy Clough, in helping me get up to speed with the code (as well as advising on our project). I'd also like to thank my previous supervisor Helvi Witek for teaching me the fundamentals of Numerical Relativity and how to use the Einstein Toolkit, as well as Hector Silva and Nicolas Yunes for the discussions provided during our collaboration.
Many thanks to my TPPC colleagues - old and new - for making the PhD experience that much more entertaining, as well as my family, for providing their full love and support over the past five years of my doctorate.
I am grateful for funding provided by the STFC, as well as the provision of computer resources and the technical support provided by a range of organisations: the Leibniz Supercomputing Center via PRACE Grant No. 2018194669 "FunPhysGW: Fundamental physics in the era of gravitational waves"; the DiRAC Consortium via STFC DiRAC Grants No. ACTP186 and No. ACSP218; the Extreme Science and Engineering Discovery Environment (XSEDE) Expanse through the allocation TG-PHY210114, which is supported by NSF Grant No. ACI-1548562; the Blue Waters sustained-petascale computing project which was supported by NSF Award No. OCI-0725070 and No. ACI1238993; the Illinois Campus Cluster, a computing resource that is operated by the Illinois Campus Cluster Program (ICCP) in conjunction with the National Center for Supercomputing Applications (NCSA) and which is supported by funds from the University of Illinois at UrbanaChampaign; the Minerva cluster at the Max Planck Institute for Gravitational Physics; the Leibnitz Supercomputing Centre SuperMUC-NG under PRACE Grant No. 2018194669; the Jülich Supercomputing Center JUWELS HPC under PRACE Grant No. 2020225359; COSMA7 in Durham and Leicester DiAL HPC under DiRAC RAC13 Grant No. ACTP238 and the Cambridge Data Driven CSD3 facility which is operated by the University of Cambridge Research Computing on behalf of the STFC DiRAC HPC Facility.

Declaration

I hereby declare that - except where specific reference is made to the work of others - the contents of this dissertation are original and have not been submitted in whole or in part for consideration for any other degree or qualification in this, or any other university. This dissertation is my own work and contains nothing which is the outcome of work done in collaboration with others, except as specified in the text and Acknowledgements. This dissertation contains fewer than 65,000 words including appendices, bibliography, footnotes, tables and equations and has fewer than 150 figures.
The original work in this thesis is based on the scientific publications and software development below, representing the outcome of my doctoral studies:

- Hector O. Silva, Helvi Witek, Matthew Elley, and Nicol as Yunes. Dynamical Descalarization in Binary Black Hole Mergers. Phys. Rev. Lett., 127(3):031101, 2021.
- Matthew Elley, Hector O. Silva, Helvi Witek, and Nicol as Yunes. Spin-induced dynamical scalarization, descalarization, and stealthness in scalar-Gauss-Bonnet gravity during a black hole coalescence. Phys. Rev. D, 106(4):044018, 2022.
- Maria Babiuc-Hamilton, Steven R. Brandt, Peter Diener, Matthew Elley, Zachariah Etienne, Giuseppe Ficarra, Roland Haas, Helvi Witek, et al., "The EINSTEIN TOOLKIT (Mayer Release: 28 Oct 2019)
- Helvi Witek, Miguel Zilhao, Gabriele Bozzola, Matthew Elley, Giuseppe Ficarra, Taishi Ikeda, Nicolas Sanchis-Gual, Hector Silva, "CANUDA : a public numerical relativity library to probe fundamental physics" (Release: 08 Oct 2021)

Abstract

Numerical Relativity (NR) is an entire field of study that attempts to harness the power of supercomputers in order to solve complex problems within General Relativity (GR). Its original purpose was to provide a means to simulate the late-inspiral and merger of binary black holes and neutrons stars, and provide accurate templates of the resulting gravitational waves that can be employed to assist in their detection. However, Numerical Relativity has now flourished into a plethora of novel avenues. From boson stars to inflation - both within GR and modifications of it - NR is a pivotal tool in understanding a broad variety of physically-realistic (albeit sometimes hypothetical) gravitating systems. In this thesis, we use NR to explore two such intriguing scenarios: the merger of binary black holes within a particular modified theory of gravity, and the stability of inhomogeneous inflation.

Contents

List of Figures

List of Tables

Chapter 1

Introduction

This thesis is split into three main sections. We first describe the basics of NR: the 3+1 framework, whereby one decomposes spacetime into its spatial and temporal components; the reformulated versions of Einstein's equations within this setting, namely the ADM and BSSN equations; how one obtains initial data to be evolved; and the gauge (co-ordinate) choices necessary to acquire a stable evolution. This will provide the framework for later research sections.

The next chapter centres on modified gravity. We provide a brief background on the subject, focusing on scalar-tensor theories and the phenomenon of *scalarization*, in which a black hole or neutron star generates a non-trivial scalar-field profile. This leads us to our research on the *dynamical descalarization* and *spin-induced dynamical scalarization/descalarization* of binary black hole mergers, the former and latter having been published in *Physical Review Letters* [5] and *Physical Review D* [6] respectively.

Lastly, we move to a cosmological setting - inflation. After a review of the theory, we look at the (soon to be published) work on applying NR to investigate how inhomogeneities in the initial conditions affect the outcome of inflation. We see that one has to alter both the standard NR techniques used to generate initial data and those employed to evolve the gauge variables. This is a natural byproduct of NR originating as a tool for astrophysics, and we therefore explore first-hand its ongoing development in the field of Cosmology.

We end the thesis with a review of the aforementioned topics and results, and describe ideas for future work and possible novel directions of the field itself.

Chapter 2

Basics of Numerical Relativity

In this chapter I will give an outline of the theoretical basis of numerical relativity. The concepts described in this chapter are based on those given in the textbooks by Alcubierre [2]; Baumgarte and Shaprio [1]; and Shibata [7].

2.1 The 3+1 Formalism

Einstein's equations are traditionally written in their fully covariant form. That is, the equations are independent of all coordinate systems, thus they describe spacetime in a manner that is absent any clear distinction between space and time. It is clear that such a formulation is not just elegant, but absolutely fundamental; the universality of the theory hinges on its coordinate independence. However, from a practical standpoint, one may need to abandon this covariant formalism in order to achieve an intuitive analysis of a gravitating system. This intuition relies on having a clear distinction between space and time, such that one can picture the evolution of a system given some initial input, as is the case for most non-relativistic systems. More pertinently, re-framing spacetime in this manner provides a natural way of characterising a system as a Cauchy (initial value) problem. This particular formulation, called the ADM or 3+1 formalism, serves as the basis of our spacetime simulations.

In the 3+1 formalism, one transforms our 4-dimensional spacetime manifold M into an initial value formulation via foliating the spacetime into a series of spacelike hypersurfaces Σ parameterised by a global time function t (see Fig. 2.1).

Given that t is a scalar field, we can define a vector orthogonal to these hypersurfaces

$$\Omega^{\mu} = \nabla^{\mu} t \,, \tag{2.1}$$

with a norm that we define as

$$\Omega_{\mu}\Omega^{\mu} \equiv \frac{-1}{\alpha^2} \,. \tag{2.2}$$

Here α is called the *lapse* function and it is assumed $\alpha > 0$ such that Ω^{μ} is timelike. The lapse is a crucial gauge function in NR as it measures the proper time of observes moving normal to the spatial

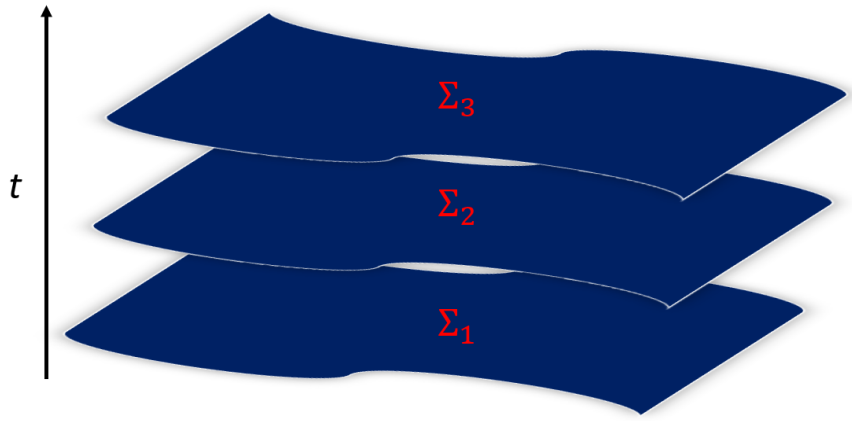

Figure 2.1: Foliation of a manifold M into a series of spacelike surfaces Σ parameterised by a scalar field t which acts as a global time function.

hypersurfaces. Subsequently, we introduce the normal vector

$$n^\mu = \alpha \Omega^\mu \,, \tag{2.3}$$

which is the normalized version of Ω^μ:

$$n_\mu n^\mu = -1 \,. \tag{2.4}$$

We would naturally want a metric purely for the spatial hypersurfaces. This spatial metric can be obtained using the normal vector

$$\gamma_{\mu\nu} = g_{\mu\nu} + n_\mu n_\nu \,, \tag{2.5}$$

where one has effectively used the timelike property of n^μ to remove the timelike parts of the 4D metric $g_{\mu\nu}$. One can see that the resultant spatial metric is indeed spacelike by contracting it with n^μ:

$$\gamma_{\mu\nu} n^\mu = g_{\mu\nu} n^\mu + n_\mu n^\mu n_\nu = 0 \,. \tag{2.6}$$

Say that we want to define a generic timelike vector field throughout the spacetime. In order to do this, we must also include a purely spatial vector living on each hypersurface in addition to the normal vector n^μ. Such a timelike vector field would then be given by

$$t^\mu = \alpha n^\mu + \beta^\mu \,, \tag{2.7}$$

where β^μ is the spatial *shift* vector constrained to the hypersurfaces by the condition

$$n^\mu \beta_\mu = 0 \,. \tag{2.8}$$

We can now adopt a coordinate system suitable for our setup. Namely, we choose our three spacelike basis vectors to reside on the spatial hypersurfaces, and our timelike basis vector to be the vector field t^μ. This means that t^μ is the congruence along which the spatial coordinates propagate, and so the shift measures

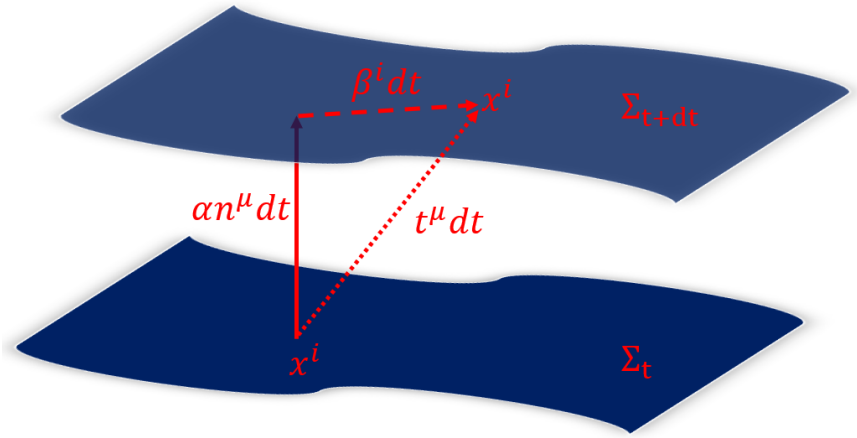

Figure 2.2: How the lapse function α and shift vector β^i structure the coordinate system in the 3+1 decomposition. The lapse quantifies the proper time measured by normal observers, effectively connecting hypersurfaces. The shift encodes the relative velocity between the normal observers and lines of constant spatial coordinates. [1].

how much the spatial coordinates are displaced with respect to the normal vector, as one progresses through the stack of hypersurfaces. Consequently, the coordinate freedom inherent in GR is entirely constrained by specifying the lapse function and the shift vector. This is illustrated in Fig. 2.2. One should note that in this adapted coordinate system (which still has degrees of freedom encoded in the lapse and shift gauge functions) the timelike component of all spatial tensors vanish. Henceforth, we will use Latin superscripts for both the spatial metric γ_{ij} and shift vector β^i in equations that consist of only spatial quantities.
Given that we have the spatial metric for the hypersurfaces, we can uniquely define spatial covariant derivatives. These are simply the 4D covariant derivatives projected onto the spatial hyperspaces, the projection operator being the raised spatial metric $\gamma_\mu^{\ \nu}$. For example, given a generic tensor $T_\mu^{\ \nu}$ the spatial covariant derivative is

$$D_\mu T_\nu^{\ \alpha} = \gamma_\mu^{\ \beta}\gamma_\delta^{\ \alpha}\gamma_\nu^{\ \kappa}\nabla_\beta T_\kappa^{\ \delta}\,. \tag{2.9}$$

The associated quantities, such as the spatial connection coefficients $\Gamma^\mu_{\nu\alpha}$ and 3D Riemann tensor $R_{\mu\nu\alpha\beta}$, then take the same form as their 4D counterparts, with D_μ replacing ∇_μ and $\gamma_{\mu\nu}$ replacing $g_{\mu\nu}$.

2.2 The Extrinsic Curvature

In classical mechanics, a collections of particles are defined by their positions and velocities (or momenta). After an initial specification, these quantities are then evolved through time using the corresponding evolution equations. In the 3+1 formalism, the quantity analogous to position is the spatial metric $\gamma_{\mu\nu}$ defined earlier. On the other hand, we have yet to establish the quantity loosely associated with velocity - the extrinsic curvature $K_{\mu\nu}$. There are a number of ways of to define the extrinsic curvature, though ultimately they are all equivalent.

Firstly, one can define the extrinsic curvature in relation to parallel transport. That is, the extrinsic curvature is a measure of the change of the normal vector under parallel transport

$$K_{\mu\nu} \equiv -\gamma_{\mu}{}^{\alpha}\gamma_{\nu}{}^{\beta}\nabla_{\alpha}n_{\beta}\,, \tag{2.10}$$

in which the second projection renders $K_{\mu\nu}$ purely spatial. Defined this way, one can easily picture the extrinsic curvature as a measure of the curvature of spatial hypersurfaces in relation to the 4D spacetime they are embedded in (see Fig. 2.3). However, though powerful as a geometric concept, the form given by (2.10) doesn't clearly reveal the extrinsic curvature as a 'velocity'.

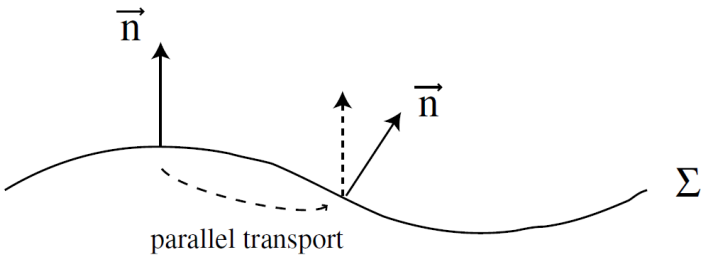

Figure 2.3: Extrinsic curvature quantifies how the normal vector n^{μ} changes under parallel transport [2].

Alternatively, one can write the extrinsic curvature as the Lie derivative of the spatial metric along the normal vector

$$\begin{aligned} K_{\mu\nu} &\equiv -\frac{1}{2}\mathcal{L}_{\mathbf{n}}\gamma_{\mu\nu} \\ &= \beta^{\alpha}\nabla_{\alpha}\gamma_{\mu\nu} + \gamma_{\mu\alpha}\nabla_{\nu}\beta^{\alpha} + \gamma_{\nu\alpha}\nabla_{\mu}\beta^{\alpha}\,. \end{aligned} \tag{2.11}$$

Roughly speaking, the Lie derivative measures how much a tensor (the spatial metric) changes along a vector (the normal vector) with respect to the corresponding coordinate change. Thus the idea that the extrinsic curvature acts as a 'velocity' becomes apparent, as it encodes how the spatial metric changes as one progresses through the stack of hypersurfaces. The trace of the extrinsic curvature K is called the *mean curvature*, it measures the change in the proper 3-volume along the normal vector

$$K = \gamma^{\mu\nu}K_{\mu\nu} = -\frac{1}{2}\gamma^{\mu\nu}\mathcal{L}_{\mathbf{n}}\gamma_{\mu\nu} = -\mathcal{L}_{\mathbf{n}}\ln\gamma^{1/2}\,. \tag{2.12}$$

2.3 The Constraint and Evolution Equations

Now that we have established the 3+1 framework, and have identified our dynamical variables $\gamma_{\mu\nu}$ and $K_{\mu\nu}$, we can recast Einstein's field equations as an initial value problem. This can be achieved by projecting the 4D Riemann tensor ${}^{(4)}R_{\mu\nu\alpha\beta}$ in (non-trivial) combinations of the spatial and normal directions, and then using these projections to re-write Einstein's equations in 3+1 form.
The possible projections of ${}^{(4)}R_{\mu\nu\alpha\beta}$ are given by the following equations

$$\gamma_\alpha{}^\delta \gamma_\beta{}^\kappa \gamma_\mu{}^\lambda \gamma_\nu{}^\sigma \, {}^{(4)}R_{\delta\kappa\lambda\sigma} = R_{\mu\nu\alpha\beta} + K_{\mu\alpha}K_{\nu\beta} - K_{\mu\beta}K_{\alpha\nu} \,, \tag{2.13}$$

$$\gamma_\alpha{}^\delta \gamma_\beta{}^\kappa \gamma_\mu{}^\lambda n^\nu \, {}^{(4)}R_{\delta\kappa\lambda\nu} = D_\beta K_{\alpha\mu} - D_\alpha K_{\beta\mu} \,, \tag{2.14}$$

$$\gamma_\mu{}^\delta \gamma_\nu{}^\kappa n^\lambda n^\sigma \, {}^{(4)}R_{\delta\lambda\kappa\sigma} = \mathcal{L}_{\mathbf{n}} K_{\mu\nu} + K_{\mu\lambda}K_\nu{}^\lambda + \frac{1}{\alpha} D_\mu D_\nu \alpha \,, \tag{2.15}$$

which are named the *Gauss-Codazzi*, *Codazzi-Mainardi* and *Ricci* equations respectively. For their full derivation, see [1]. All other combinations of the spatial and normal projections vanish as a result of the symmetries of the Riemann tensor. One should note that (2.15) contains the Lie derivative of the extrinsic curvature along the normal vector, whereas (2.13) and (2.14) do not. As in (2.11) for the extrinsic curvature, the nature of this Lie derivative is similar to that of a time derivative. As (2.13) and (2.14) do not contain this time derivative, we will use them to derive the Hamiltonian and momentum constraints. These constraint equations impose restrictions on the field data $(\gamma_{\mu\nu}, K_{\mu\nu})$ for each hypersurface. On the other hand, (2.15) is used to derive an evolution equation.

For the Hamiltonian constraint, we start by contracting the Gauss-Codazzi equation twice, which results in

$$\gamma^{\alpha\mu}\gamma^{\beta\nu} \, R_{\alpha\beta\mu\nu} = {}^{(3)}R + K^2 - K_{\mu\nu}K^{\mu\nu} \,, \tag{2.16}$$

the LHS of which can be expanded out to give

$$\gamma^{\alpha\mu}\gamma^{\beta\nu} \, {}^{(4)}R_{\alpha\beta\mu\nu} = \left(g^{\alpha\mu} + n^\alpha n^\mu\right)\left(g^{\beta\nu} + n^\beta n^\nu\right) \, {}^{(4)}R_{\alpha\beta\mu\nu} \tag{2.17}$$

$$= \, {}^{(4)}R + 2n^\mu n^\nu \, {}^{(4)}R_{\mu\nu} \tag{2.18}$$

$$= 2n^\mu n^\nu \, {}^{(4)}G_{\mu\nu} \,. \tag{2.19}$$

Then using Einstein's equation we obtain the Hamiltonian constraint

$$R + K^2 - K_{\mu\nu}K^{\mu\nu} = 16\pi\rho \tag{2.20}$$

where

$$\rho \equiv n_\mu n_\nu \, {}^{(4)}T^{\mu\nu} \,, \tag{2.21}$$

is the energy density measured by normal observers.

For the momentum constraint, we contract the Codazzi-Mainardi equation once to yield

$$\gamma_\mu{}^\delta \gamma^{\kappa\lambda} n^\sigma \, {}^{(4)}R_{\delta\kappa\lambda\sigma} = D_\nu K_\mu{}^\nu - D_\mu K \,. \tag{2.22}$$

Considering the LHS

$$\gamma_\mu{}^\delta \gamma^{\kappa\lambda} n^\sigma \, {}^{(4)}R_{\delta\kappa\lambda\sigma} = -\gamma_\mu^\delta n^\sigma \, {}^{(4)}R_{\delta\sigma}$$

$$= -\gamma_\mu^\delta n^\sigma \, {}^{(4)}G_{\delta\sigma} \,, \tag{2.23}$$

where we have expanded out the second projection operator and made use of the symmetries of the Riemann tensor in the first line, and invoked the definition of the Einstein tensor in the second line (noting that the Ricci term vanishes). Again we insert Einstein's equation to yield the momentum constraint

$$D_\nu K_\mu^{\ \nu} - D_\mu K = 8\pi S_\mu \,, \tag{2.24}$$

where S_μ is the momentum density measured by normal observers, defined as

$$S_\mu \equiv -\gamma_\mu^{\ \delta} n^\sigma \, {}^{(4)}T_{\delta\sigma} \,. \tag{2.25}$$

Lastly, to obtain a true evolution equation for the extrinsic curvature in terms of 3+1 quantities one must decompose the 4D Riemann tensor in (2.15):

$$\begin{aligned} \gamma_\mu^{\ \delta}\gamma_\nu^{\ \kappa} n^\lambda n^\sigma \, {}^{(4)}R_{\delta\lambda\kappa\sigma} &= \gamma^{\delta\kappa}\gamma_\mu^{\ \sigma}\gamma_\nu^{\ \lambda} \, {}^{(4)}R_{\delta\lambda\kappa\sigma} - \gamma_\mu^{\ \sigma}\gamma_\nu^{\ \lambda} \, {}^{(4)}R_{\lambda\sigma} \\ &= R_{\mu\nu} + KK_{\mu\nu} - K_{\mu\lambda}K_\nu^\lambda - \gamma_\mu^{\ \sigma}\gamma_\nu^{\ \lambda} \, {}^{(4)}R_{\lambda\sigma} \\ &= R_{\mu\nu} + KK_{\mu\nu} - K_{\mu\lambda}K_\nu^\lambda - 8\pi\gamma_\mu^{\ \sigma}\gamma_\nu^{\ \lambda}({}^{(4)}T_{\lambda\sigma} - \frac{1}{2}g_{\lambda\sigma}T) \,, \end{aligned} \tag{2.26}$$

where we substituted the Gauss-Codazzi (2.13) in the second line and Einstein's equation in the third. We then substitute this result into Ricci's equation (2.15) to obtain

$$\mathcal{L}_{\mathbf{n}} K_{\mu\nu} = R_{\mu\nu} + KK_{\mu\nu} - 2K_{\mu\lambda}K_\nu^\lambda - 8\pi(S_{\mu\nu} - \frac{1}{2}\gamma_{\mu\nu}(S-\rho)) - \frac{1}{\alpha}D_\mu D_\nu \alpha \,, \tag{2.27}$$

where $S_{\mu\nu}$ is the spatial stress tensor given by

$$S_{\mu\nu} \equiv \gamma_\mu^{\ \alpha}\gamma_\nu^{\ \beta} \, {}^{(4)}T_{\alpha\beta} \,, \tag{2.28}$$

and S is its trace.
(2.10) and (2.27) give the Lie derivatives of the spatial metric and extrinsic curvature along the normal vector, respectively. These are our evolution equations. However, given that we will use the adapted coordinate system in which t^μ is a basis vector, we would like to write these evolution equations so that Lie derivative of these quantities is directed along this time vector. We can use (2.7) and the properties of the Lie derivative to achieve this:

$$\mathcal{L}_{\mathbf{t}}\gamma_{\mu\nu} = -2\alpha K_{\mu\nu} + \mathcal{L}_\beta \gamma_{\mu\nu} \,, \tag{2.29}$$

$$\mathcal{L}_{\mathbf{t}} K_{\mu\nu} = \alpha(R_{\mu\nu} + KK_{\mu\nu} - 2K_{\mu\lambda}K_\nu^\lambda) - 8\pi\alpha(S_{\mu\nu} - \frac{1}{2}\gamma_{\mu\nu}(S-\rho)) - D_\mu D_\nu \alpha + \mathcal{L}_\beta K_{\mu\nu} \,. \tag{2.30}$$

Finally, we re-write the constraint and evolution equations in the adapted coordinate basis, in which purely spatial tensors have no timelike components and the Lie derivatives along the time vector t^μ reduce to the partial time derivative. These are summarised below:

The ADM equations

Metric

$$ds^2 = -\alpha^2 dt^2 + \gamma_{ij}(dx^i + \beta^i dt)(dx^j + \beta^j dt)\,. \tag{2.31}$$

Hamiltonian constraint

$$R + K^2 - K_{ij}K^{ij} = 16\pi\rho\,. \tag{2.32}$$

Momentum constraint

$$D_j(K^{ij} - \gamma^{ij}K) = 8\pi S^i\,. \tag{2.33}$$

Spatial metric evolution

$$\partial_t \gamma_{ij} = -2\alpha K_{ij} + D_i\beta_j + D_j\beta_i\,. \tag{2.34}$$

Extrinsic curvature evolution

$$\begin{aligned}\partial_t K_{ij} = \alpha(R_{ij} + KK_{ij} - 2K_{ik}K^k_j) - 8\pi\alpha(S_{ij} - \frac{1}{2}\gamma_{ij}(S-\rho)) - D_iD_j\alpha \\ + \beta^k\partial_k K_{ij} + K_{ik}\partial_j\beta^k + K_{kj}\partial_i\beta^k\,.\end{aligned} \tag{2.35}$$

One should note that the constraint equations, if satisfied initially, should remain so throughout the evolution. However, as we are dealing with numerics, errors tend to accumulate and thus the constraints will inevitably be violated. It is therefore crucial to monitor these violations throughout the evolution to ensure they do not grow to (relatively) large values. The only alternative would be to solve the constraints at each time step of the evolution, but due to their elliptic nature this is a computationally time-consuming enterprise and thus tends to be practically unfeasible.
More pertinently however is the issue of well-posedness in regard to the evolution equations, which we will now address.

2.4 The BSSN Equations

Unfortunately, full 3D simulations using the ADM equations quickly become unstable (unless one applies certain symmetries, which is of-course non-generic). This is the consequence of the fact that the ADM system of equation is not well-posed. A well-posed system of equations has a unique solution which depends continuously on the initial data. That is, the solution vector $\mathbf{u}$ (which consists of the n dependent-variables

of the system) has a norm bounded by

$$||\mathbf{u}(t, x^i)|| \leq ke^{\alpha t}||\mathbf{u}(0, x^i)||\,, \tag{2.36}$$

for which k and α are constants that are independent of the initial data.
For hyperbolic equations, the concept of well-posedness is intimately linked to the notion of hyperbolicity. Namely, a *strongly-hyperbolic* system of equations is well-posed, whereas a *weakly-hyperbolic* system is not. To demonstrate this, one uses the fact that hyperbolic equation can be formulated in a way similar to the source-less 3D wave equation, which in its first-order form is given by

$$\partial_t \mathbf{u} + \mathbf{M}^i \partial_i \mathbf{u} = 0\,, \tag{2.37}$$

where $\mathbf{M}^i$ is a collection of $n \times n$ matricess that depend smoothly on the spatial derivative operators. Considering an arbitrary unit vector n^i one can then construct the principal symbol of the system

$$\mathbf{P} \equiv \mathbf{A}^i n_i\,. \tag{2.38}$$

For all hyperbolic equations, $\mathbf{P}$ has real eigenvalues. Strongly-hyperbolic systems are defined as those for which $\mathbf{P}$ has a complete set of eigenvectors, whereas this is not the case for weakly-hyperbolic systems. One finds that the existence of a complete set of eigenvectors allows for the construction of a norm of the solutions which is constant in time, demonstrating that the system is well-posed. Furthermore, the eigenvectors provide the characteristics along which the wave-like solutions travel, with finite speeds given by the eigenvalues. Thus there exists a finite past domain of dependence (see [8] for more details).
The ADM evolution equations (2.34) and (2.35) can be shown to be weakly-hyperbolic. To remedy this, one notes that the principal symbol is dependent on the highest-order derivatives of the system. Thus, if we want to alter the ADM evolution equations so that they are strongly-hyperbolic, we need to address the form of the highest-order derivatives - the second-order derivatives of the gravitational fields - that are expressed. Fortunately, one can add multiples of the constraint equations to the evolution equations as they vanish identically. Since the constraints also contain these second-order derivatives, we can use them to alter the hyperbolic nature of the evolution equations.
The BSSN formalism, based on work by Baumgarte, Shapiro, Shibata and Nakamura [9,10], involves several modifications. Firstly, one decomposes the extrinsic curvature into its trace K and traceless component

$$A_{ij} = K_{ij} - \frac{1}{3}\gamma_{ij}K\,. \tag{2.39}$$

Then a conformal re-scaling is applied to the metric and traceless extrinsic curvature

$$\gamma_{ij} = \frac{1}{\chi}\tilde{\gamma}_{ij}\,, \tag{2.40}$$

$$A_{ij} = \frac{1}{\chi}\tilde{A}_{ij}\,, \tag{2.41}$$

where $\tilde{\gamma}_{ij}$ and $\tilde{A}_{ij}$ are the conformal spatial metric and conformal traceless extrinsic curvature, and the conformal factor χ is set such that $\tilde{\gamma}_{ij}$ has unit determinant [11]:

$$\chi = (\det\, \gamma_{ij})^{-\frac{1}{3}} \,. \tag{2.42}$$

We will see shortly how specifying the conformal factor in this way allows one to transform the evolution equations into a "wave-like" form. With the decompositions above we can find the evolution equations for χ and K by taking the trace of the evolution equations for the spatial metric (2.34) and extrinsic curvature (2.35) respectively:

$$\partial_t \chi = \frac{2}{3}\alpha\chi K - \frac{2}{3}\chi\partial_k\beta^k + \beta^k\partial_k\chi \,, \tag{2.43}$$

$$\partial_t K = -D_i D^i\alpha + \alpha\left(\tilde{A}_{ij}\tilde{A}^{ij} + \frac{1}{3}K^2\right) + \beta^i\partial_i K + 4\pi\alpha(\rho + S) \,, \tag{2.44}$$

where the Hamiltonian constraint (2.32) has been used to eliminate the Ricci scalar in the second equation. Subtracting (2.43) from (2.34) and (2.44) from (2.35) then yields the evolution equations for the conformal spatial metric and the conformal traceless extrinsic curvature:

$$\partial_t\tilde{\gamma}_{ij} = -2\alpha\tilde{A}_{ij} + \tilde{\gamma}_{ik}\partial_j\beta^k + \tilde{\gamma}_{jk}\partial_i\beta^k - \frac{2}{3}\tilde{\gamma}_{ij}\partial_k\beta^k + \beta^k\partial_k\tilde{\gamma}_{ij} \tag{2.45}$$

$$\begin{aligned}\partial_t\tilde{A}_{ij} = {} & \chi^2\left[-(D_iD_j\alpha)^{\mathrm{TF}} + \alpha\left(R_{ij}^{\mathrm{TF}} - 8\pi\alpha S_{ij}^{\mathrm{TF}}\right)\right] + \alpha\left(K\tilde{A}_{ij} - 2\tilde{A}_{il}\tilde{A}^l_j\right) \\ & + \tilde{A}_{ik}\partial_j\beta^k + \tilde{A}_{jk}\partial_i\beta^k - \frac{2}{3}\tilde{A}_{ij}\partial_k\beta^k + \beta^k\partial_k\tilde{A}_{ij} \,,\end{aligned} \tag{2.46}$$

where the superscript "TF" denotes the traceless part of the correspond tensor. Introducing the conformal factor - as well as the traceless and trace components of the extrinsic curvature - have been shown to improve the stability of simulations. However, the evolution equations are still not strongly-hyperbolic. To achieve this, one first introduces of the *conformal connection functions*

$$\begin{aligned}\tilde{\Gamma}^i &= \tilde{\gamma}^{jk}\tilde{\Gamma}^i_{jk} \\ &= -\partial_j\tilde{\gamma}^{ij} \,,\end{aligned} \tag{2.47}$$

i.e. the contraction of the Christoffel symbols of the conformal metric $\tilde{\Gamma}^i_{jk}$. The second equation is a consequence of setting the determinant of the conformal spatial metric to unity. The reason for introducing these functions is that they allow us to remove mixed second derivative terms present in the Ricci tensor. That is, we can decompose the Ricci tensor into two parts

$$R_{ij} = \tilde{R}_{ij} + R^{\chi}_{ij} \,, \tag{2.48}$$

in which $\tilde{R}_{ij}$ is the Ricci tensor associated with the conformal spatial metric and R^{χ}_{ij} only depends on the conformal factor. It is the former term which contain these mixed derivatives that spoil the clear hyperbolic "wave-like" nature of the corresponding evolution equations. By including these conformal connection functions one can write the conformal Ricci tensor as

$$\tilde{R}_{ij} = -\frac{1}{2}\tilde{\gamma}^{lm}\partial_m\partial_l\tilde{\gamma}_{ij} + \tilde{\Gamma}^k\tilde{\Gamma}_{(ij)k} + \tilde{\gamma}^{lm}\left(2\tilde{\Gamma}^k_{l(i}\tilde{\Gamma}_{j)km} + \tilde{\Gamma}^k_{im}\tilde{\Gamma}_{klj}\right) \,, \tag{2.49}$$

such that we only have Laplacian second-order derivatives. However, we now consider $\tilde{\Gamma}^i$ as independent variables, and so we need their evolution equation. This arises from combining their definition (2.47) with the evolution equation for the spatial metric (2.34):

$$\begin{aligned}\partial_t \tilde{\Gamma}^i = &\tilde{\gamma}^{jk}\partial_j\partial_k\beta^i + \frac{1}{3}\tilde{\gamma}^{ij}\partial_j\partial_k\beta^k + \beta^j\partial_j\tilde{\Gamma}^i - \tilde{\Gamma}^j\partial_j\beta^i + \frac{2}{3}\tilde{\Gamma}^i\partial_j\beta^j \\ &- 2\left(\alpha\partial_j\tilde{A}^{ij} + \tilde{A}^{ij}\partial_j\alpha\right). \end{aligned} \tag{2.50}$$

Crucially, to finally render the system strongly-hyperbolic we add the (conformally expanded) momentum constraint (2.33) which removes the divergence term $\partial_j\tilde{A}^{ij}$, giving the final form for the evolution of $\tilde{\Gamma}^i$:

$$\begin{aligned}\partial_t \tilde{\Gamma}^i = &-2\tilde{A}^{ij}\partial_j\alpha + 2\alpha\left(\tilde{\Gamma}^i_{jk}\tilde{A}^{jk} - \frac{2}{3}\tilde{\gamma}^{ij}\partial_j K - \frac{3}{2}\tilde{A}^{ij}\frac{\partial_j\chi}{\chi}\right) \\ &+ \beta^k\partial_k\tilde{\Gamma}^i + \tilde{\gamma}^{jk}\partial_j\partial_k\beta^i + \frac{1}{3}\tilde{\gamma}^{ij}\partial_j\partial_k\beta^k \\ &+ \frac{2}{3}\tilde{\Gamma}^i\partial_k\beta^k - \tilde{\Gamma}^k\partial_k\beta^i - 16\pi\alpha\tilde{\gamma}^{ij}S_j\,. \end{aligned} \tag{2.51}$$

Thus, we have established the stable BSSN formulation which is summarised below:

The BSSN evolution equations

$$\partial_t\chi = \frac{2}{3}\alpha\chi K - \frac{2}{3}\chi\partial_k\beta^k + \beta^k\partial_k\chi \tag{2.52}$$

$$\partial_t\tilde{\gamma}_{ij} = -2\alpha\tilde{A}_{ij} + \tilde{\gamma}_{ik}\partial_j\beta^k + \tilde{\gamma}_{jk}\partial_i\beta^k - \frac{2}{3}\tilde{\gamma}_{ij}\partial_k\beta^k + \beta^k\partial_k\tilde{\gamma}_{ij} \tag{2.53}$$

$$\partial_t K = -\gamma^{ij}D_iD_j\alpha + \alpha\left(\tilde{A}_{ij}\tilde{A}^{ij} + \frac{1}{3}K^2\right) + \beta^i\partial_i K + 4\pi\alpha(\rho + S) \tag{2.54}$$

$$\begin{aligned}\partial_t\tilde{A}_{ij} = &\chi^2\left[-(D_iD_j\alpha)^{\mathrm{TF}} + \alpha\left(R^{\mathrm{TF}}_{ij} - 8\pi\alpha S^{\mathrm{TF}}_{ij}\right)\right] + \alpha\left(K\tilde{A}_{ij} - 2\tilde{A}_{il}\tilde{A}_{jj}\right) \\ &+ \tilde{A}_{ik}\partial_j\beta^k + \tilde{A}_{jk}\partial_i\beta^k - \frac{2}{3}\tilde{A}_{ij}\partial_k\beta^k + \beta^k\partial_k\tilde{A}_{ij} \end{aligned} \tag{2.55}$$

$$\begin{aligned}\partial_t\tilde{\Gamma}^i = &-2\tilde{A}^{ij}\partial_j\alpha + 2\alpha\left(\tilde{\Gamma}^i_{jk}\tilde{A}^{jk} - \frac{2}{3}\tilde{\gamma}^{ij}\partial_j K - \frac{3}{2}\tilde{A}^{ij}\frac{\partial_j\chi}{\chi}\right) \\ &+ \beta^k\partial_k\tilde{\Gamma}^i + \tilde{\gamma}^{jk}\partial_j\partial_k\beta^i + \frac{1}{3}\tilde{\gamma}^{ij}\partial_j\partial_k\beta^k \\ &+ \frac{2}{3}\tilde{\Gamma}^i\partial_k\beta^k - \tilde{\Gamma}^k\partial_k\beta^i - 16\pi\alpha\tilde{\gamma}^{ij}S_j \end{aligned} \tag{2.56}$$

2.5 Initial Data

Now that we have established a formulation of Einstein's equations that can be used to evolve initial data in a numerically stable manner, we must address how one can sensibly specify this initial data in the first place. Indeed, the constraint equations (2.32) and (2.33) already impose restrictions on our initial fields

(γ_{ij}, K_{ij}). However, these are symmetric spatial tensors and thus they posses six independent components. The constraint equations determine four of these, and coordinate freedom further reduces these by another four. This leaves us with four final components - these are related to the two dynamical degrees of freedom characterising the gravitational field and their time derivatives. The crux of the matter is this: how does one determine which quantities are to be constrained and which are to be freely specified? In linearized GR, the dynamical degrees of freedom are encoded in the polarization modes of gravitational waves, identified as the transverse-traceless part of the perturbed metric. In the same spirit, we will decompose the constraint equations into transverse and longitudinal components in attempt to associate the former with the dynamical degrees of freedom and the latter with the constrained components.

This decomposition is very similar to that used to develop the BSSN equations, and even includes a conformal transformation. The extrinsic curvature of the initial data is decomposed into its trace and traceless components as in (2.39) and then a conformal transformation is applied to the spatial metric and traceless extrinsic curvature

$$\gamma_{ij} = \psi^4 \bar{\gamma}_{ij} \,, \tag{2.57}$$

$$A_{ij} = \psi^{-2} \bar{A}_{ij} \,, \tag{2.58}$$

where ψ is the conformal factor. As in the BSSN derivation, we can set the conformal factor such that the determinant of the conformal spatial metric is unity, thus reducing the number of degrees of freedom in the spatial metric itself. On the other hand, this conformal transformation is clearly quite different from that used to derive the BSSN equations, which is why we have used ψ instead of χ as the conformal factor and also stated conformal tensors using an over-bar rather than a tilde. The exponent of the conformal factor chosen in (2.58) is natural as it means that A_{ij} has zero divergence only when $\bar{A}_{ij}$ does, whereas the exponent of the conformal factor in (2.57) is convenient but somewhat arbitrary.

With these conformal quantities we can re-write the Hamiltonian (2.32) and momentum (2.33) constraints as

$$8\bar{D}^2\psi - \psi\bar{R} - \frac{2}{3}\psi^5 K^2 + \psi^{-7}\bar{A}_{ij}\bar{A}^{ij} = -16\pi\psi^5\rho \,, \tag{2.59}$$

$$\bar{D}_j\bar{A}^{ij} - \frac{2}{3}\psi^6\bar{\gamma}^{ij}\bar{D}_j K = 8\pi\psi^{10}S^i \,, \tag{2.60}$$

where $\bar{R}$ and $\bar{D}_i$ are the corresponding conformal Ricci scalar and conformal spatial covariant derivative, respectively. It should be noted that, when present, conformally rescaling the RHS (matter sources) is often necessary. Briefly put, this is to ensure that solutions are unique, a characteristic determined by the sign of the conformal factor exponent in the source term. This issue will be addressed later in regards to solving the constraints in an inhomogeneous inflationary spacetime.

We will perform one last decomposition - that of $\bar{A}_{ij}$. This can be done in a variety of ways, however we will focus on what is called the *conformal transverse-traceless* decomposition (CTT). For this method one splits $\bar{A}_{ij}$ into its transverse and longitudinal components

$$\bar{A}^{ij} = \bar{A}^{ij}_{TT} + (\bar{\mathbf{L}}W)^{ij} \,, \tag{2.61}$$

in which the first term is the transverse part and so has zero divergence

$$\bar{D}_j \bar{A}^{ij}_{TT} = 0\,, \tag{2.62}$$

and the second (longitudinal) term is defined by the action of the conformal longitudinal operator $\bar{\mathbf{L}}$ on a vector potential W^i:

$$(\bar{\mathbf{L}}W)^{ij} = \bar{D}^i W^j + \bar{D}^j W^i - \frac{2}{3}\bar{\gamma}^{ij}\bar{D}_k W^k\,. \tag{2.63}$$

Concordantly, we can re-write the momentum constraint (2.60) as

$$\left(\bar{\Delta}_{\bar{\mathbf{L}}}W\right)^i - \frac{2}{3}\psi^6\bar{\gamma}^{ij}\bar{D}_j K = 8\pi\psi^{10}S^i\,, \tag{2.64}$$

where

$$\left(\bar{\Delta}_{\bar{\mathbf{L}}}W\right)^i = \bar{D}_j(\bar{\mathbf{L}}W)^{ij} \tag{2.65}$$

$$= \bar{D}^2 W^i + \frac{1}{3}\bar{D}^i\left(\bar{D}_j W^j\right) + \bar{R}^i_j W^j \tag{2.66}$$

is called the *vector Laplacian*.

Thus (2.59) and (2.64) are our final constraint equations. To obtain consistent initial data, one follows the steps given below:

The conformal transverse-traceless decomposition

Hamiltonian Constraint

$$8\bar{D}^2\psi - \psi\bar{R} - \frac{2}{3}\psi^5 K^2 + \psi^{-7}\bar{A}_{ij}\bar{A}^{ij} = -16\pi\psi^5\rho\,, \tag{2.67}$$

Momentum Constraint

$$\left(\bar{\Delta}_{\bar{\mathbf{L}}}W\right)^i - \frac{2}{3}\psi^6\bar{\gamma}^{ij}\bar{D}_j K = 8\pi\psi^{10}S^i\,, \tag{2.68}$$

Method

1. Specify $\bar{\gamma}_{ij}$, K and $\bar{A}^{ij}_{TT}$ (and the matter terms ρ and S^i if present)
2. Solve the Hamiltonian (2.59) and momentum (2.64) constraints for ψ and W^i respectively
3. Use the results to assemble γ_{ij} and K_{ij} to be used in the evolution equations

One can choose to specify the free data such that the constraints are greatly simplified. For the case of setting up binary black hole initial data - which we will use in the modified gravity chapter - one chooses $K = 0$, as well as $\bar{\gamma}_{ij} = \eta_{ij}$ i.e. conformal flatness. The former assumption decouples the momentum constraint from the Hamiltonian constraint (as the second term on the LHS of (2.68) vanishes), whereas

the latter reduces the vector Laplacian to a simple operator of partial differentials. The Hamiltonian and momentum constraints are then simply given by

$$\bar{D}^2\psi + \frac{1}{8}\psi^{-7}\bar{A}_{ij}\bar{A}^{ij} = 0\,, \tag{2.69}$$

$$\partial^j\partial_j W^i + \frac{1}{3}\partial^i\partial_j W^j = 0\,. \tag{2.70}$$

One can solve the momentum constraint (2.70) analytically, yielding $\bar{A}_{ij}$ in terms of the initial linear and angular momentum of the black holes (to be specified). The solution of the Hamiltonian constraint (2.69) for the conformal factor can be written as

$$\psi = \frac{\mathcal{M}_1}{r_1} + \frac{\mathcal{M}_2}{r_2} + u\,, \tag{2.71}$$

where r_i is the coordinate distance to the centre of the i^{th} BH. The masses $\mathcal{M}_i$ are equivalent to the respective BH masses only at infinite separation. The *Brill–Lindquist* solution - given by the first two terms of (2.71) - solves the homogeneous (time-symmetric i.e.$K_{ij} = 0$) form of (2.69), which is simply Laplace's equation for ψ[1]. The singularities at $r_i = 0$ are coordinate rather than physical - they correspond to spatial infinity of two separate universe each connected to the original spacetime via Einstein-Rosen bridges (see Fig. 2.4). Given these singular points are technically not part of the manifold, they are referred to as *punctures*. For the inhomogeneous case, the inclusion of u in the solution (2.71) is a correction given the presence of the second term in (2.69). Substituting (2.71) into (2.69) yields an elliptic equation for u that is not only regular everywhere but also possesses a unique solution without requiring boundary conditions to be imposed on the punctures. Consequently, one can now calculate the conformal factor using only asymptotic flatness for the exterior boundary.
However, for other spacetimes the presence of non-vanishing matter terms in the constraint equations (2.67) and (2.68) can greatly complicate the process of obtaining solutions via CCT. For instance, when scalar fields are present one encounters issues obtaining unique solutions. This problem - and its solution - will be addressed in the chapter on inflation.

2.6 Gauge Conditions

The inherent coordinate freedom of GR is encoded in the lapse function α and shift vector β^i. The former quantifies the manner in which the spatial hypersurfaces are embedded in the 4D spacetime by measuring the proper time of observers moving normal to these hypersurfaces (with velocity n^μ). The latter dictates how spatial coordinates move as one progresses through the stack of spatial hypersurfaces, with respect to the normal observers. What values - or conditions - one chooses for these gauges is not arbitrary. They may simply encapsulate coordinate freedom, but this choice of coordinates when simulating any particular system can greatly affect the stability of the simulation and is therefore highly dependent on the character

[1] As Laplace's equation is linear one can superpose an arbitrary number of BH solutions $\psi_i = \mathcal{M}_i/r_i$

Figure 2.4: Diagram of the Brill-Lindquist solution for two BHs - the universe is connected to two separate spacetimes by Einstein-Rosen Bridges [1].

of the system itself. All simulations throughout this work employ the same conditions on the lapse and shift: *1+log slicing* for the lapse

$$\left(\partial_t - \beta^j \partial_j\right) \alpha = -2\alpha K \,, \tag{2.72}$$

and *Gamma-driver* for the shift

$$\partial_t \beta^i = \frac{3}{4} B^i \,, \tag{2.73a}$$

$$\partial_t B^i = \partial_t \bar{\Gamma}^i - \eta B^i \,. \tag{2.73b}$$

though a slight modification of the 1+log lapse condition will be necessary when we evolve inflationary spacetimes.

2.6.1 1+log slicing

The 1+log slicing condition (2.72) has a number of important (and useful) properties. First and foremost, it exhibits *strong singularity avoidance*. That is, the lapse goes to zero before coordinates ever reach a physical singularity. This behaviour of the lapse - vanishing as one approaches a singularity - is known as the *collapse of the lapse*. We can demonstrate this behaviour by considering 1+log slicing with a zero shift vector

$$\partial_t \alpha = -2\alpha K \,, \tag{2.74}$$

and then using the contracted form of the ADM evolution equation for the spatial metric (2.34) one can obtain

$$d \ln \gamma^{\frac{1}{2}} = \frac{1}{2} d\alpha \,. \tag{2.75}$$

One can now see where 1+log slicing gets its name, as integrating the equation above yields

$$\alpha = 1 + \ln \gamma \tag{2.76}$$

where we have set the integration constant to one. Alternatively, one can write

$$\gamma^{1/2} = Ce^{\alpha/2}\,, \tag{2.77}$$

in which C is an integration constant. Thus, we see that as the lapse collapses ($\alpha \to 0$) the volume element remains finite and so a singularity is not reached.
A second important property of (2.72) is that its hyperbolic - note its similarity to the wave-equation. It is possible to incorporate the gauge equations in elliptic form i.e. without involving a time parameter. For instance, setting $K = \partial_t K = 0$ on every hypersurface yields an elliptic equation for the lapse. This is called *maximal slicing* as it ensures that the volume of each hypersurface is always maximum with respect to perturbations of the hypersurfaces. Though physical singularities are avoided by construction, it is notoriously computationally expensive to solve elliptic equations on every hypersurface. This is why we do not solve the constraint equations at each stage of the evolution, settling for just monitoring constraint violation to ensure they do not grow too large. Therefore, employing a hyperbolic gauge condition is ideal in regards to efficiency, as one simply evolves the gauge functions along with the evolution variables. It is worth noting that, as a hyperbolic system, there is an associated finite gauge speed. Since the gauge functions are of a coordinate rather than a physical nature, a faster-than-light gauge speed is possible (arguably preferable in fact, as one may want to alter the coordinate system of a region long before physical signals reach it).

2.6.2 Gamma-driver shift

We have seen how the 1+log slicing condition prevents the occurrence of singularities in our computational domain. That is, it prevents spatial volume elements converging to zero. Similarly, the Gamma-driver condition for the shift vector uses the spatial coordinate freedom to retain numerical stability by preventing these volume elements from being distorted too strongly. In our highly dynamic spacetime simulations, one can expect such distortions e.g. from the presence of a black hole. If such distortions become excessive, they may result in unfeasibly large gradients in the spatial metric. We will show how the Gamma-driver shift condition (2.73) deals with this issue below.
We are trying to minimise certain changes in the spatial metric, specifically changes in the shape of the volume elements rather than their sizes (the latter being controlled by the lapse condition). Since the size of the volume elements is encoded in the conformal factor χ, we need only to ensure the conformal spatial metric components do not change. That is, the time derivative of $\tilde{\gamma}_{ij}$ is itself a measure of this distortion. Consequently, we would like to set its divergence to zero as a way of minimising the distortion over the hypersurface. This is effectively the purpose of the first term in the RHS of (2.80b)

$$\partial_t \tilde{\Gamma}^i = \partial_j \partial_t \tilde{\gamma}^{ij}\,, \tag{2.78}$$

which we could set to zero (*Gamma-freezing condition*) if we were fine with elliptic gauge conditions. However, as with the lapse conditions, we would like a hyperbolic formulation to reduce computational

cost. That is the reason for the other terms in (2.73) - they turn a strict elliptic equation into a hyperbolic one such that the system relaxes to $\partial_t \tilde{\Gamma}^i = 0$ in simulation time (though the second term on the RHS of (2.80b) is a damping term used to avoid strong oscillations in the shift vector).

2.6.3 The Moving Puncture Gauge

The combination of 1+log slicing and Gamma-driver shift is particularly effective in evolving stable binary black hole spacetimes for which the initial data is of puncture form (2.71). Consequently, this combination is known as the *moving puncture gauge*. As the name suggests, this gauge allows the punctures to propagate safely throughout the numerical domain without generating significant errors. The singularities associated with the punctures retain their coordinate nature - no physical singularities arise. However, their topological form is somewhat altered during the evolution; the punctures no longer represent spatial infinity of a separate asymptotically flat spacetime. Rather, the slicing causes the wormhole to stretch into an infinitely long cylinder of finite radius. Simultaneously, the shift condition effectively moves coordinate points away from the inner asymptotic region and into the throat. Ultimately, this leads to a 'trumpet' geometry in which the puncture is the throat itself.

The Moving Puncture Gauge

1+log slicing

$$\left(\partial_t - \beta^j \partial_j\right) \alpha = -2\alpha K \,, \tag{2.79}$$

Gamma-driver shift

$$\partial_t \beta^i = \frac{3}{4} B^i \,, \tag{2.80a}$$

$$\partial_t B^i = \partial_t \bar{\Gamma}^i - \eta B^i \,, \tag{2.80b}$$

where $\eta > 0$ is a parameter to be chosen.

Naturally one may worry about having singularities moving around the numerical domain, even if they are just coordinate rather than physical. This issue is remedied by comparing how we conformally transform the spatial metric for both BSSN and the initial data, given by (2.40) and (2.57) respectively. Thus we have $\chi = \psi^{-2}$, meaning the coordinate singularity in ψ is not present in our evolved χ. However, one usually places a lower limit on χ for the sake of numerical precision near the puncture.

Chapter 3

Modified Gravity

3.1 Background

Einstein's Theory of Relativity is arguably one of the most elegant theories of modern physics. The unification of the ostensibly disparate nature of time, space and gravity into a single conceptual framework, described by the mathematics of differential geometry, revolutionised our understanding of universe. The only conceivable rival in this regard would be Quantum Mechanics, the advent and development of which Einstein also gave a significant contribution. However, the elegance of a theory is more of a preferred subjective quality rather than an absolute necessity. The arbiter of all physical theories, including relativity, is experiment. In this regard, relativity again proves itself exceptional; it's predictive power has been demonstrated by countless observations [12]. From the perihelion shift of Mercury to the expansion of the universe itself, relativity has predicted a vast range of phenomena that have been validated by experiment and observation to a remarkable degree of accuracy. It is clear that the elegance of the theory is matched by its prowess as a description of truth. Nevertheless, despite this homage to the theory, we will address its shortcomings as a depiction of reality.

There are a plethora of reasons to believe GR is not the final theory of gravity. Firstly, the demand for a "theory of everything" necessitates a union between GR and quantum theory. Unfortunately, the success of such a unification has eluded theorists for several decades. Roughly speaking, if one were to probe the Planck scale in order to explore high-energy corrections to GR as a QFT, the high energies would result in the formation of a Planck-sized BH. Thus, the nature of a quantum theory of gravity appears quite distinct from its Standard Model counterparts. Furthermore, at the other end of the energy spectrum observations have confirmed the accelerated expansion of the universe. The unidentified mechanism behind this acceleration - coined "dark energy" - has been used as ammunition against the theory. Indeed, one can employ "Einstein's greatest blunder", the cosmological constant, into the Friedmann-Lemaître-Robertson-Walker (FLRW) metric used to model the universe's expansion to achieve this acceleration. The phenomenology of this constant can be identified with vacuum zero-point fluctuations, which can be calculated from standard quantum field theory. Unfortunately, such a calculation yields a value more than 120 magnitudes

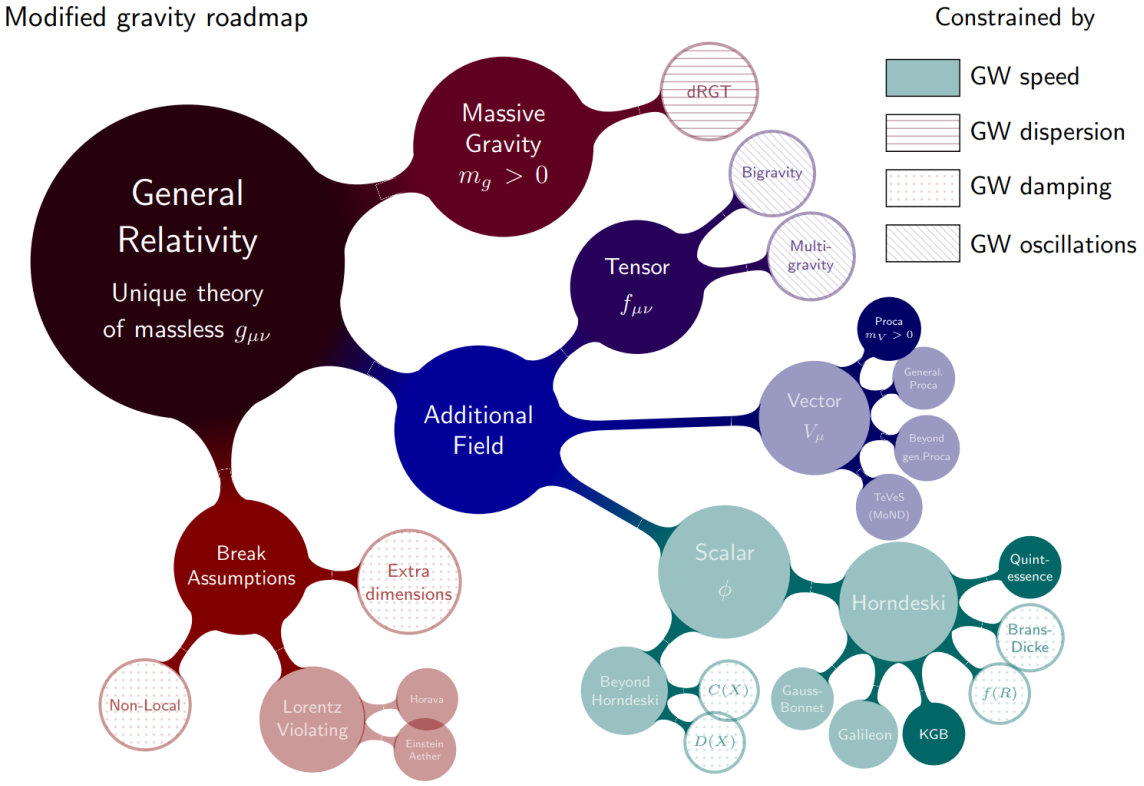

Figure 3.1: A roadmap of the suggested alternatives to general relativity, with their respective primary gravitational wave constraints [3].

larger than that required by observation. Thus standard GR cosmology appears to fail at explaining this phenomenon.
Ultimately, it is clear that there is apt motivation for a theory of gravity which appears as GR for scales where it has been well tested, but diverges from Einstein's theory in strong-field or large scale environments. Broadly named "Modified Gravity", there have been a vast number of alternative suggestions over the last several decades. A "road-map" of such suggestions is illustrated in Fig. 3.1.

3.2 Scalar-tensor theories

Lovelock's theorem states:
Einstein's equations are the only second order field equations which can be derived from a local action containing only the four-dimensional spacetime metric and its derivatives.
Thus we can use Lovelock's theorem to generate possible alternatives to GR - one simply bypasses the assumptions implicit in the theorem:

- **Include additional fields in the gravitational action**
- Allow higher than 2^{nd} order field equations

- Include more than 4 dimensions
- Abandon locality

For this work, we will focus on the inclusion of an additional field, namely a scalar-field. Theories of this kind are called scalar-tensor theories. It is important to note that the addition of a scalar field (the only confirmed case being the Higgs) is not somewhat ad-hoc. In fact, scalar fields often rise naturally via the compactification of higher dimensional string theories, and so there is indeed theoretical backing for their inclusion [13].
One finds that the general form of the Lagrangian for scalar-tensor theories can be written as [13]

$$\mathcal{L} = \frac{1}{16\pi}\sqrt{-g}\left[\phi R - \frac{\omega(\phi)}{\phi}\nabla_\mu\phi\nabla^\mu\phi - V(\phi)\right] + \mathcal{L}_m\left(\Psi, g_{\mu\nu}\right) , \tag{3.1}$$

where $\omega(\phi)$ is some function of the scalar-field, $V(\phi)$ is the scalar-field potential and $\mathcal{L}_m$ is the Lagrangian for the matter fields Ψ. One should note that the matter Lagrangian is of the usual form. That is, test particles will follow the geodesics given by the metric $g_{\mu\nu}$ (the weak equivalence principle is obeyed) and energy-momentum is conserved. Scalar-tensor theory Lagrangians that possess these qualities are in the *Jordan frame*. One can always perform a conformal transformation of the metric such that these properties no longer hold (but other convenient ones emerge). For example, one can transform the Lagrangian into the *Einstein frame* in which the non-minimal coupling of the scalar-field to the Ricci tensor is no longer present and one simply has Einstein's theory with a minimally-coupled canonical scalar field. This is achieved via the conformal transformation

$$g_{\mu\nu} = \frac{\tilde{g}_{\mu\nu}}{\phi} , \tag{3.2}$$

and scalar-field redefinition

$$\tilde{\phi} = \int \sqrt{3 + 2\omega(\phi)}d\phi , \tag{3.3}$$

to yield

$$\mathcal{L} = \frac{1}{16\pi}\sqrt{-g}\left[\tilde{R} - \tilde{\nabla}_\mu\tilde{\phi}\tilde{\nabla}^\mu\tilde{\phi} - U(\tilde{\phi})\right] + \mathcal{L}_m\left(\Psi, \tilde{g}_{\mu\nu}/\phi\right) , \tag{3.4}$$

where $U(\tilde{\phi}) = V(\phi)/\phi^2$ and we have used tildes to indicate that the corresponding quantities are now associated with the Einstein frame metric $\tilde{g}_{\mu\nu}$. Although the Lagrangian is now in a more familiar form, one should note that matter is now coupled directly to the scalar-field ϕ. Consequently, test particles will not longer follow the geodesics of the metric $\tilde{g}_{\mu\nu}$, so the weak equivalence principle is violated and energy-momentum is no longer conserved.
Theoretical underpinnings aside, our motivation for the addition of a scalar field implicitly includes observational consequences. However, the verification of GR to an extraordinary precision in the weak-field limit will naturally constrain any such deviations in this regime. Indeed, Brans-Dicke theory - for which one sets $\omega = const.$ - has been highly constrained by solar system experiments (see [12]). Fortunately, letting ω be ϕ-dependent allows the avoidance of weak-field constraints through the dynamical approach to GR in the weak-field regime (the GR limit being $\omega \to \infty$). In fact, in the cosmological (FLRW) setting

an attractor mechanism exists for these generalised scalar-tensor theories such that GR can be obtained at late times [14]. This allows for modification of early universe phenomenology, a classic example being scalar-tensor inflationary models [15, 16]. Furthermore, the possibility of scalar-tensor theories being used to explain late-time cosmology problems - namely dark energy - was also explored [17, 18]. Unfortunately, however, the binary neutron star merger GW170817 has imposed significant constraints on such theories via the observed speed of GWs [19].

The Lagrangian (3.1) is not, strictly-speaking, the most generalised version of a scalar-tensor theory. Rather, the introduction of a fundamental scalar-field allows for the inclusion of higher-curvature terms that play a non-trivial role in the subsequent field equations. In the absence of the scalar-field such higher-curvature terms can either be transformed into a topological (boundary) term that plays no role in the field dynamics, or will lead to higher than second-order field equations. Though not entirely non-rectifiable, such higher-order field equations can lead to solutions possessing Ostrogradsky instabilities - the presence of negative energy states rendering the system unstable[1] [20]. However, the combination of these higher-curvature terms and an additional scalar-field can lead to the field equations remaining second-order, thus avoiding this issue. This brings us to Horndeski's theory: the most general second-order scalar-tensor theory in four dimensions [21]. Horndeski's theory encompasses a broad range of scalar-tensor theories with (and without) higher-curvature terms through arbitrary functions of ϕ and $X = \nabla_\mu \nabla^\mu$ in the Lagrangian which one can specify to give a particular theory. The Lagrangian itself is rather extensive as the theory is so general, and has therefore been relegated to Appendix A.

Recently, one particular subset of Horndeski's theory has been the focal point of much interest. This subset is commonly known as scalar Gauss-Bonnet gravity (sGB). It is defined by the following Lagrangian

$$\mathcal{L} = \frac{1}{16\pi}\sqrt{-g}\left[R - \frac{1}{2}(\nabla\phi)^2 + \alpha f(\phi)\mathscr{G}\right], \tag{3.5}$$

where α is a coupling constant, $f(\phi)$ is a scalar-field coupling function and $\mathscr{G}$ is a particular combination of curvature terms known as the Gauss-Bonnet invariant

$$\mathscr{G} = R^2 - 4R_{\mu\nu}R^{\mu\nu} + R_{\mu\nu\rho\sigma}R^{\mu\nu\rho\sigma}. \tag{3.6}$$

In the absence of the scalar-field, the Gauss-Bonnet invariant is a purely topological term and so does not enter the field equations[2]. However, through a non-trivial coupling with the scalar-field $f(\phi)$ one retains this term in both the metric and scalar-field equations of motion, with significant phenomenological consequences.

[1] $f(R)$ theory is an exception - though it contains higher-order Ricci scalar terms leading to fourth-order equations of motion, the Ostrogradsky instability is avoided nonetheless. In fact, $f(R)$ theory can be re-written as a scalar-tensor theory via a conformal transformation [13].

[2] This is not true in higher dimensions. In fact, it is possible to recover the Gauss-Bonnet invariant in the 4D field equations without a scalar-field. This is done by re-scaling the Gauss-Bonnet coupling in the higher dimensional theory and then taking the limit $D \to 4$, though this is non-trivial and beyond the purview of this work (see [22]).

3.3 Scalarization

One consequence alluded to in the previous chapter is that of *scalarization* - the formation of a (stationary) scalar-field profile surrounding BHs and neutron stars. In GR, the no-hair theorem[3] states that all stationary, asymptotically flat BH solutions are determined by three parameters: mass, angular momentum and electromagnetic charge (for the more general case of Einstein-Maxwell theory) [23]. In other words, the solutions are of Kerr-Newman form. This result has been extended to Brans-Dicke theory [24] and even the whole set of general scalar-tensor theories given by the Lagrangian (3.1) [25, 26].
For the case of Horndeski's theory, a no-hair theorem has been established [27], though it comes with a range of caveats [28,29]. Firstly, the theorem assumes a static and spherically symmetric spacetime, rather than the more relaxed assumptions of stationarity and axisymmetry usually invoked. Furthermore, it only applies to the subset of Horndeski's theory that exhibits shift-symmetry - the field equations must be invariant under the transformation $\phi \to \phi + c$, where c is a constant. The Noether current generated from this symmetry is the crux of the theorem, and with it lies further assumptions which one can easily bypass. Indeed, sGB gravity (3.5) with a linear coupling function $f(\phi) = \phi$ is both shift-symmetric (as an isolated Gauss-Bonnet invariant in the action vanishes in the field equations) and only allows BHs with scalar hair [30]. One can demonstrate this by considering the scalar-field equation of motion for shift-symmetric sGB gravity

$$\Box\phi = -\alpha\mathscr{G}\,. \tag{3.7}$$

In order for a trivial scalar-field configuration to be allowed i.e. $\phi = const.$ (which we can set to zero using the shift-symmetry), the RHS of (3.7) must be zero in that region of spacetime. However, this cannot be the case for BH spacetimes as $\mathscr{G}$ reduces to the Kretschmann scalar (see (3.6)). Thus we are left with two possibilities: such a theory does not possess BH solutions or the BH solutions are dressed with a non-trivial scalar configuration i.e. scalar hair. In [30] scalarized BH solutions were constructed, thus confirming the latter option.
Moreover, by considering the scalar equation for the general sGB theory

$$\Box\phi = -\alpha f'(\phi)\mathscr{G}\,, \tag{3.8}$$

it is clear from the above logic that BHs in *any* sGB theory will be scalarized as long as the derivative of the coupling function $f'(\phi) \neq 0$ for all ϕ. A well-known example is dilaton Gauss-Bonnet gravity, for which $f(\phi) = e^{\phi}$. Arising from the low-energy limit of a higher-dimensional string theory, this effective theory was known to possess scalarized BH solutions since '95 [31].
Alternatively, one could have a coupling function such that $f'(\phi_0) = 0$, where ϕ_0 is some particular value of the scalar-field. For instance, the simplest example is quadratic sGB gravity, given by $f(\phi) = \phi^2$ and for which $\phi_0 = 0$. Such theories allow the familiar hairless GR (i.e. Kerr-Newman) solutions. However, these are not the only solutions - scalarized BHs also exist in these theories. The transition between GR

[3]Not to be confused with the *no-hair conjecture*, which makes the much more general statement that *all* BH solutions are determined by mass, angular momentum and electromagnetic charge.

and scalarized BHs is governed by a mechanism called *spontaneous scalarization* [32, 33]. A similar such mechanism was first discovered in some scalar-tensor theories for neutron stars - a coupling between the trace of the matter stress-energy tensor T and scalar-field ϕ leads to a non-trivial scalar configuration being generated around neutron stars which have a particular range of masses [34]. For the spontaneous scalarization mechanism we are considering, it is the scalar-Gauss-Bonnet coupling that generates the scalar configuration with no need for matter content (although neutron stars do scalarize as well). This mechanism can be identified by linearizing the scalar-field equation (3.8) about the trivial solution ($\phi = \phi_0$),

$$\Big(\Box + \alpha f''(\phi_0)\mathscr{G}\Big)\delta\phi = 0\,, \tag{3.9}$$

where $\delta\phi$ is the linear perturbation of the scalar-field and $f''(\phi_0)$ is the second derivative of the coupling function at the trivial solution. Clearly (3.9) is of Klein-Gordon form, and so the second term acts as the square of an effective mass:

$$m^2_{\text{eff}} \equiv -\alpha f''(\phi_0)\mathscr{G}\,, \tag{3.10}$$

which if sufficiently[4] negative leads to a tachyonic instability. For example, consider a non-spinning BH in quadratic sGB with a positive coupling constant. In this case, m^2_{eff} is negative throughout the spacetime, with a magnitude depending on the strength of the coupling α and the Gauss-Bonnet invariant which reduces to the Schwarzschild Kretschmann scalar

$$\mathscr{G}_{schw} = \frac{48m^2}{r^6}\,, \tag{3.11}$$

for which m is the BH mass and r is the radial coordinate from its centre. As the dependence on the radial distance goes by a much higher power than that of the mass, smaller BHs will exhibit larger Gauss-Bonnet curvatures about their horizons than their larger counterparts. Thus, for a given coupling strength, reducing the mass of a stable unscalarized BH will eventually trigger a tachyonic instability and subsequent exponential scalar field growth. The endpoint of this instability is a scalarized BH solution as identified in [32, 33]. An important property of these scalarized BHs is that they contain finite-area singularities [30]. Therefore, under the assumption of a regular horizon, these BH solutions have a minimum mass. This means that there is an upper and lower mass limit for these scalarized solutions - they form bands in the mass-coupling parameter space (this is extended to include BH spin for rotating solutions).

Naturally, the fact that sGB theories allows for scalarized BHs begs the question of whether such phenomenology is observable. A primary avenue of this possibility is via gravitational waves from a black hole binary merger. How would the presence of this scalarized state alter the subsequent waveform? For the case of shift-symmetric sGB, this questions was addressed in [35] by simulating binary black hole merger using numerical relativity. Unfortunately, at that time a well-posed formulation of sGB had not been discovered, and so the authors had to work perturbatively in the coupling constant i.e. with no backreaction on the metric. Although approximate, these simulations were able to forecast a constraint on the

[4] An imaginary effective mass is a necessary but not sufficient condition for the instability, rather the associated effective potential must be deep enough for an unstable mode to develop (see [32, 33] for details).

coupling α by calculating the dephasing of the gravitational waveform due to the emission of scalar dipole radiation. We now pose the following question: in sGB theories that allow both GR and scalarized BH states, what effect does this scalarization phenomenon have on the dynamics of binary black hole mergers and the resulting gravitational waves?

3.4 Research work I: Dynamical Descalarization in Binary Black Hole Mergers

This section contains the article "*Dynamical Descalarization in Binary Black Hole Mergers*" which was published in *Physical Review Letters* [5].

3.4.1 Abstract

Scalar fields coupled to the Gauss–Bonnet invariant can undergo a tachyonic instability, leading to spontaneous scalarization of black holes. Studies of this effect have so far been restricted to single black hole spacetimes. We present the first results on dynamical scalarization in head-on collisions and quasicircular inspirals of black hole binaries with numerical relativity simulations. We show that black hole binaries can either form a scalarized remnant or dynamically *descalarize* by shedding off its initial scalar hair. The observational implications of these findings are discussed.

3.4.2 Introduction

Despite the elegance of Einstein's theory, it presents several shortcomings: explaining the late-time acceleration of the Universe and providing a consistent theory of quantum gravity or the presence of spacetime singularities [e.g. in black holes (BHs)]. Candidate theories (of quantum gravity) that remedy these shortcomings typically predict the coupling to additional fields or higher curvature corrections [36]. Binary BHs, their gravitational wave (GW) emission, and the first GW detections by the LIGO-Virgo Collaboration [37,38] offer unique insights into the nonlinear regime of gravity that unfolds during the BHs' inspiral and merger and enable new precision tests of gravity [39, 40]. So far, these tests have been parametrized null tests against General Relativity (GR) [41, 42] or used a mapping between these parameters and those of specific theories [43–45]. To do the latter, however, requires GW predictions in specific theories.
One of the most compelling beyond-GR theories, scalar Gauss–Bonnet (sGB) gravity introduces a dynamical scalar field coupled to the Gauss–Bonnet invariant. sGB gravity emerges in the low-energy limit of quantum gravity paradigms such as string theory [46], through a dimensional reduction of Lovelock gravity [47] and is the simplest model that contains higher curvature operators. The most studied class of sGB gravity with a dilatonic or linear coupling to the scalar field gives rise to hairy BHs [28, 30, 31, 48–51]. This theory, however, has been strongly constrained with GW observations from binary BHs [44].

We turn our attention to another interesting class of sGB gravity that is both unconstrained by GW observations and gives rise to (spontaneously) scalarized BHs [32,33]. Spontaneous scalarization is a familiar concept in beyond-GR theories; e.g. it is well established for neutron stars in scalar-tensor theories [34,52]. In such theories, the neutron star matter itself can induce a tachyonic instability that spontaneously scalarizes the star [53]. When placed in a binary system, initially unscalarized neutron stars can scalarize dynamically near their merger or a scalarized neutron star can induce a scalar field in their unscalarized companion [54–57]. In sGB gravity, it is the spacetime curvature itself that induces scalarization of BHs [32,33], although this has only been shown for isolated BHs so far. In this Letter we investigate, for the first time, dynamical scalarization in *binary* BHs. We concentrate on head-on collisions of BHs, but also present the first binary black hole (BH) inspiral study. Before doing so, it is convenient to first review the basics of sGB gravity and spontaneous BH scalarization.

3.4.3 Scalar Gauss-Bonnet gravity and scalarization

sGB gravity is described by the action

$$S = \frac{1}{16\pi}\int \mathrm{d}^4x\sqrt{-g}\left[R - \frac{1}{2}\left(\nabla\Phi\right)^2 + \frac{\alpha_{\rm GB}}{4}f(\Phi)\,\mathscr{G}\right], \tag{3.12}$$

where a real scalar field Φ is coupled to the Gauss–Bonnet invariant $\mathscr{G} = R^2 - 4R_{\mu\nu}R^{\mu\nu} + R_{\mu\nu\rho\sigma}R^{\mu\nu\rho\sigma}$, through the function $f(\Phi)$ and a dimensionful coupling constant $\alpha_{\rm GB}$. We use geometrical units, $c = 1 = G$, in which $\alpha_{\rm GB}$ has units of [length]^2. The action (3.12) gives rise to the scalar field equation of motion

$$\Box\Phi = -(\alpha_{\rm GB}/4)f'(\Phi)\,\mathscr{G}\,, \tag{3.13}$$

where we defined $(\cdot)' = \mathrm{d}(\cdot)/\mathrm{d}\Phi$. The function $f(\Phi)$ selects different "flavors" of sGB gravity [58, 59]. One subset of these theories has $f' \neq 0$ everywhere. It includes variants of sGB gravity with dilatonic $f(\Phi) \propto \exp(\Phi)$ [31, 48, 49] or shift-symmetric $f(\Phi) \propto \Phi$ [28, 30, 60] couplings, in which BHs always have scalar hair [51, 61]. Another interesting class of sGB theories admits an extremum $f'(\Phi_0) = 0$ for a constant Φ_0. They give rise to an effective space-dependent mass term $m^2_{\rm eff} = -f''(\Phi_0)\mathscr{G}$. This class includes quadratic $f(\Phi) \propto \Phi^2$ [32, 62] and Gaussian $f(\Phi) \propto \exp(\Phi^2)$ [33] models.
The latter class still admits all vacuum (BH) solutions of GR together with $\Phi = \Phi_0 = $ const. In fact, if $f''(\Phi_0)\mathscr{G} < 0$ these solutions are unique due to a no-hair theorem [32]. A linear stability study of these $\Phi_0 = $ const. solutions around a Schwarzschild BH reveals that this condition is a requirement for the absence of a tachyonic instability ($m^2_{\rm eff} > 0$) for the scalar field perturbations [32]. If the effective mass $m^2_{\rm eff} < 0$, a tachyonic instability is triggered and the sGB scalar field is excited and *spontaneously scalarizes* the BH. This linear instability [63] is quenched at the nonlinear level, resulting in a scalarized BH as end-state [64]. The simplest theory that admits scalarized BHs is described by the quadratic coupling $f(\Phi) = \bar{\beta}_2\,\Phi^2$, where $\bar{\beta}_2 = $ const. The relevant parameter in this theory is the dimensionless constant $\beta_2 = (\alpha_{\rm GB}/m^2)\bar{\beta}_2$, where m is the characteristic mass of the system.

The onset of scalarization is fully determined by the scalar's linear dynamics on a given GR background. For a Schwarzschild BH of mass m, for which $\mathscr{G} \geqslant 0$ everywhere, scalarization first occurs for a spherically symmetric scalar field if $\beta_2 = \beta_c \sim 1.45123$, a result in agreement with nonlinear calculations [32,33]. For values below β_c the scalar perturbation decays monotonically at late times (we call them "subcritical"), precisely at β_c the scalar field forms a bound state around the BH ("critical"), and above it the scalar field grows exponentially with time ("supercritical"). This result was recently generalized to Kerr BHs, where spin-induced scalarization can take place for $\beta_2 < 0$, for dimensionless spin parameters $\chi \geqslant 0.5$ [65–68]. Nonlinear rotating scalarized BH solutions in sGB gravity were found for both positive [69,70] and negative values of β_2 [4,71]. So far studies of scalarization in sGB gravity focused on single BHs. We advance these studies to BH binaries, and expand upon [35], focusing on the quadratic theory $f(\Phi) = \bar{\beta}_2 \Phi^2$, as discussed next.

3.4.4 Numerical methods and simulations

We investigate BH scalarization in the decoupling limit, i.e., we numerically evolve the scalar field on a time-dependent background in vacuum GR that represents binary BH spacetimes. Unless stated otherwise, we follow the approach of [35] and refer to it for details. We foliate the spacetime into spatial hypersurfaces with 3-metric γ_{ij} and extrinsic curvature $K_{ij} = -(2\alpha)^{-1}\,\mathrm{d}_t\gamma_{ij}$, where $\mathrm{d}_t = \partial_t - \mathcal{L}_\beta$, $\mathcal{L}_\beta$ being the Lie derivative along the shift vector β^i, and α is the lapse function. We write Einstein's equations as a Cauchy problem and adopt the Baumgarte-Shapiro-Shibata-Nakamura formulation [9, 10] of the time evolution equations complemented with the moving-puncture gauge conditions [72, 73]. We prepare Brill-Lindquist initial data [74, 75] for head-on collisions or Bowen-York initial data [76, 77] for a quasicircular BH binary. To evolve the scalar field, we introduce its momentum $K_\Phi = -\alpha^{-1}\,\mathrm{d}_t\Phi$, and write its field equation (3.13) as

$$\begin{aligned} \mathrm{d}_t\Phi &= -\alpha K_\Phi\,, \\ \mathrm{d}_t K_\Phi &= -D^i\alpha D_i\Phi - \alpha\left(D^i D_i\Phi - K K_\Phi + \frac{\alpha_{\rm GB}}{4} f'\mathscr{G}\right)\,, \end{aligned} \tag{3.14}$$

where D_i is the covariant derivative associated with γ_{ij}, $K = \gamma^{ij}K_{ij}$, $f' = 2\bar{\beta}_2\,\Phi$, and $\mathscr{G}$ is the Gauss–Bonnet invariant of the background spacetime. We set the system's total mass to unit, i.e., $M = m_1 + m_2 = 1$, where $m = m_{1,2}$ is the component's mass. The scalar field is initialized either as a spherically symmetric Gaussian shell (G) located at $r_0 = 12M$ and with width $\sigma = 1M$ as in [35] or as a bound state (B) around each binary component,

$$\begin{aligned} &\Phi|_{t=0} = 0\,,\quad K_\Phi|_{t=0} = \frac{1}{\sqrt{4\pi}}\exp\left[\frac{(r-r_0)^2}{\sigma^2}\right]\,, \\ &\Phi|_{t=0} = \frac{mr}{\varrho^2}\left[c_1 + \frac{c_2 mr}{\varrho^2} + \frac{c_3(mr)^2}{\varrho^4}\right]\,,\quad K_\Phi|_{t=0} = 0\,. \end{aligned} \tag{3.15}$$

Here, $\varrho = m + 2r$, and $c_1 = 3.68375$, $c_2 = 4.972416$, $c_3 = 4.972416 \cdot 10^2$ are fitting constants to reproduce the numerical results in [32].

We perform our numerical simulations with CANUDA [35, 78–80], coupled to the open-source EINSTEIN TOOLKIT [81,82]. We extended the implementation of [35,79,80] to general coupling functions f, including the quadratic coupling. We employ the method of lines with fourth-order finite difference stencils to realize spatial derivatives and a fourth-order Runge-Kutta time integrator. We use box-in-box mesh refinement provided by CARPET [83]. The numerical grid contains seven refinement levels, with the outer boundary located at $256M$ and a grid spacing of $\mathrm{d}x = 1.0M$ on the outer mesh. To assess the numerical accuracy of our simulations we evolved case (b) in Fig. 3.2 with additional resolutions $\mathrm{d}x = 0.9M$ and $\mathrm{d}x = 0.8M$. We find second-order convergence and a relative discretization error of $\Delta\Phi_{00}/\Phi_{00} \lesssim 0.5\%$, where Φ_{00} is the $\ell = \mathfrak{m} = 0$ multipole of the scalar field. We present the corresponding convergence plot for the scalar monopole and for the gravitational wave $\ell = 2$, $\mathfrak{m} = 0$ mode in Fig. B.1 of the Supplemental Material.

3.4.5 Results

We performed a large set of BH head-on collisions with varying mass ratio $q = m_1/m_2 \leqslant 1$, total mass $M = 1$ and initial separation $d = 25M$, considering both initial data in (3.15). The BHs merge at $t_{\rm M} \sim 179.5M$, as estimated from the peak of the $\ell = 2, m = 0$ multipole of the gravitational waveform. To guide our choices of β_2, we recall that the critical coupling for the fundamental mode is $\beta_{2,\rm c} = \beta_{\rm c}\,(m/M)^2$ with $\beta_{\rm c} \sim 1.45123$, and m denotes either the individual BHs' mass $m_{1,2}$ or the total mass M. For example, for an equal-mass binary with $m_1 = m_2 = M/2$, the critical coupling for the individual holes is $\beta^{(1)}_{2,\rm c} = \beta^{(2)}_{2,\rm c} = \beta_{\rm c}/4 = 0.36275$ and that of the final hole is approximately $\beta^{\rm f}_{2,\rm c} = \beta_{\rm c}$ where we neglected the small mass loss in the form of GWs during the collision [84, 85].

Here we present a selection of our results, illustrated in Fig. 3.2, to highlight our most important findings. We vary the initial state by setting the coupling parameter β_2 such that (a) none of the BHs are initially scalarized, (b) the smaller-mass BH initially carries a bound-state scalar field, both BHs carry initially a bound-state scalar that leads either to a nonscalarized final BH [case (c)] or a scalarized final BH [case (d)].

In Fig. 3.3 we show the $\ell = m = 0$ scalar field multipole extracted on a sphere of fixed radius $r_{\rm ex} = 50M$, as a function of time, and we present snapshots of the scalar's profile in the Supplemental Material. In case (a), the scalar perturbation is not supported at all (since $m_{\rm eff} = 0$) and, indeed, after a brief interaction at early times it decays already before the BHs collide. In cases (b) and (c) we find a constant scalar field before the BHs collide, that is consistent with a bound state around the individual ($q = 1$) or smaller-mass BH ($q = 1/2$). After the merger the scalar field decays since the curvature (and thus $m_{\rm eff}$) decreases and the system no longer supports a bound state – the final BH dynamically *descalarizes*. In case (d), the scalar field grows exponentially before the merger because it is supercritical for the individual BHs and settles to a constant in time that is consistent with a bound state around the final BH.

In Fig. 3.4 we show two-dimensional snapshots of the scalar field and spacetime curvature for case (b) which illustrates the dynamical descalarization phenomenon. The color map is shared among all panels and shows the amplitude of $\log_{10}|\Phi|$, while the curves are isocurvature levels of $\mathscr{G}M^4 = \{1, 10^{-1}, 10^{-2}, 10^{-3}\}$. Initially,

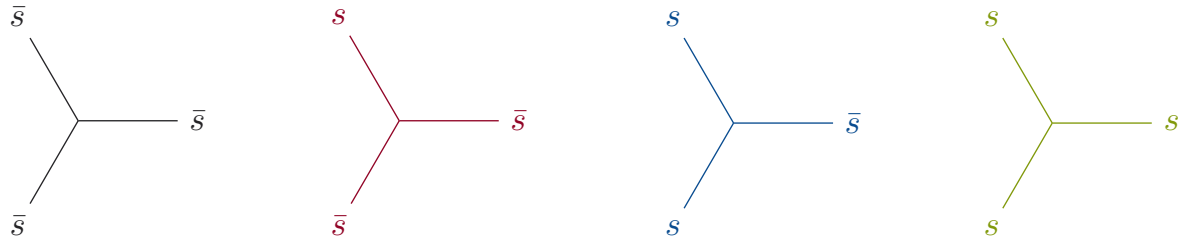

(a) – {G, 1, 0} (b) – {B, 1/2, 0.16125} (c) – {B, 1, 0.36281} (d) – {B, 1, 1.45123}

Figure 3.2: Summary of simulations of BH head-on collisions, where $\bar{s}$ and s stand for initial or final states that are either nonscalarized or scalarized respectively. Each diagram is labeled by the initial data (Gaussian shell "G" or bound state "B"), the mass ratio $q = m_1/m_2$ (1 or 1/2) and the coupling parameter β_2. In case (a) (first diagram) two nonscalarized BHs produce a nonscalarized remnant. In case (b) (second diagram) a scalarized and a nonscalarized BH produce a nonscalarized remnant. This initial configuration is possible when q is different from one. In case (c) (third diagram) two scalarized BHs produce a nonscalarized remnant. Finally, in case (d) (fourth diagram) two scalarized BHs produce a scalarized remnant.

at $t = 1M$, both BHs (whose locations are revealed by the isocurvature levels) are surrounded by nontrivial scalar field profiles given by (3.15). At $t = 50M$, the smaller BH hosts a bound state scalar that is dragged along the hole's motion, inducing scalar dipole radiation that would impact the GWs emitted. In contrast, the scalar field around the larger BH disperses because its curvature is too small to sustain a bound state for a coupling of $\beta_2 = 0.16125$. The system thus evolves as a $s + \bar{s}$ process in the notation of Fig. 3.2. At

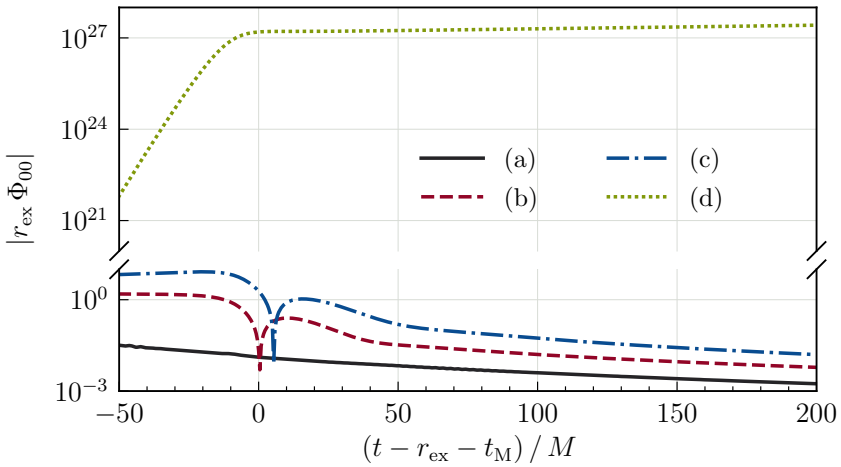

Figure 3.3: Time evolution of the scalar field $\ell = m = 0$ multipole in the background of a BH head-on collision with initial separation $d = 25M$. It is rescaled by the extraction radius $r_{\rm ex} = 50M$ and shifted in time such that $(t - r_{\rm ex} - t_{\rm M})/M = 0$ corresponds to the BHs' merger. The labels refer to the four cases summarized in Fig. 3.2.

$t = 160M$, the BHs are about to merge, as indicated by the two lobes in the isocurvature contours, the curvature of the combined system decreases and the scalar field starts dissipating. At $t = 182M$, which is shortly after the collision, the system has descalarized since for the final BH $\beta^{\rm f}_{2,{\rm c}} > \beta_2$.

We also simulated the inspiral of an equal-mass, nonspinning BH binary with initial separation of $d = 10M$, $\beta_2 = 0.36281$, and bound state scalar field initial data. This corresponds to an initial configuration in which both BHs are scalarized, and then, after merger, the remnant is not scalarized, which is analogous to case (c) of Fig. 3.2 in the head-on case. In Fig. 3.5, we show the gravitational quadrupole waveform (bottom panel), as characterized by the $\ell = \mathfrak{m} = 2$ mode of the Newman-Penrose scalar Ψ_4, together with the scalar field's monopole (top) and quadrupole (middle). The scalar's monopole Φ_{00} exhibits the distinctive signature of descalarization: the increase in the field's amplitude during the inspiral of scalarized BHs is followed by a complete dissipation of the scalar field after the merger ($t_{\rm M} \sim 917M$) as the curvature of the remnant BH no longer supports a bound state. In addition, the dynamics of the BH binary sources scalar quadrupole radiation (of the initially spherically symmetric scalar). The field's amplitude grows exponentially during the inspiral and decays after the BHs have merged. The origin of this excitation is not direct scalarization of the $\ell = 2$ scalar bound state, but due to the inspiral of two scalarized (or "hairy") BHs. This interpretation is further supported by the observation that the phase of the $\ell = \mathfrak{m} = 2$ scalar mode is driven by the binary's orbital frequency. We also observed this for the $\ell = \mathfrak{m} = 4$ mode and expect it to happen for all even $\ell = \mathfrak{m}$ modes. For $q = 1$, the odd $\ell = \mathfrak{m}$ modes are suppressed due to symmetry, whereas they would be excited in the general case $q \neq 1$. The descalarization during the merger is reminiscent of the decrease in scalar charge observed in the shift-symmetric theory [35], however, with the striking difference that here the remnant BH is a rotating GR solution.

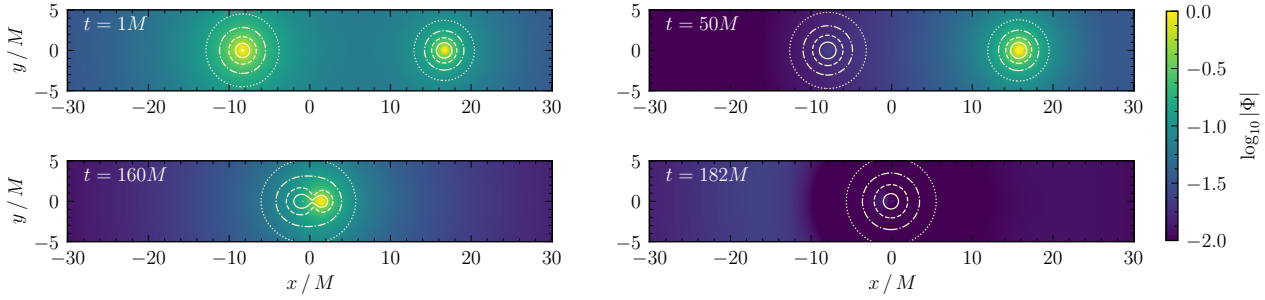

Figure 3.4: Scalar field and Gauss–Bonnet dynamics on the xy–plane for case (b). We show the amplitude of $\log_{10}|\Phi|$ (color map) together with the Gauss–Bonnet invariant (isocurvature levels) at the beginning of the evolution (top left), during the BHs' approach (top right), shortly before the collision (bottom left) and shortly after the merger (bottom right). The isocurvature levels correspond to $1M^{-4}$ (solid line), $10^{-1}M^{-4}$ (dashed line), $10^{-2}M^{-4}$ (dot-dashed line) and $10^{-3}M^{-4}$ (dotted line).

3.4.6 Discussion

We presented the first numerical relativity simulations of the scalar field dynamics in binary BH spacetimes in quadratic sGB gravity [32]. We found that the interplay between mass ratio q and β_2 can result in different scenarios for the scalar field dynamics. Most notably, it can lead to a *dynamical descalarization*

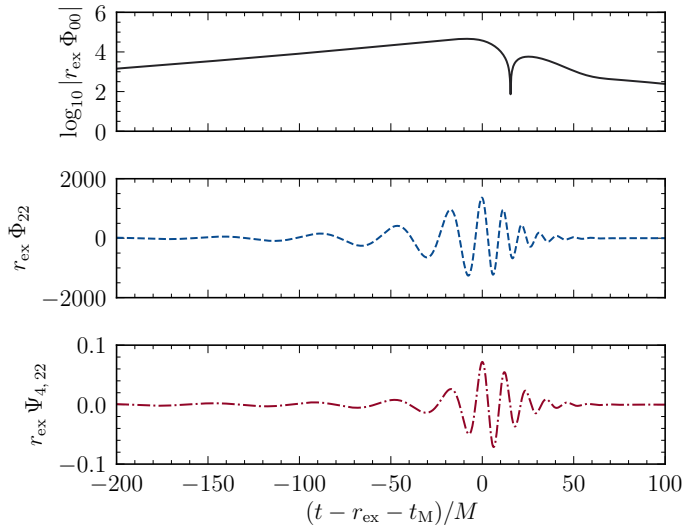

Figure 3.5: Scalar and gravitational waveforms, rescaled by the extraction radius $r_{\rm ex} = 50M$, sourced by an equal-mass BH binary with bound state initial data on each BH. This system is the inspiral counterpart of case (c) and shows dynamical descalarization in action.

of the binary, which we observed in both head-on and quasicircular inspiral simulations. Here we focused on $\beta_2 \geqslant 0$, but the case $\beta_2 < 0$ would be particularly interesting to study in inspiral simulations. More specifically, the spinning remnant of a binary BH merger typically has a dimensionless spin $\chi \sim 0.7$ [86], sufficient to trigger a spin-induced tachyonic instability of the scalar field [65]. It would be interesting to frame this effect within the effective field theory (EFT) of [87] or in a post-Newtonian framework [88–90], although the latter may not be suitable for the modeling of a nonlinear dynamical scalarization process.
The scalar excitations we have discovered during binary BH coalescence in this class of sGB theories have important implications to GW observations and tests of GR. In particular, the scalar excitations will drain the binary of energy as they propagate away from the system, the monopole scalar piece inducing dipole losses, and the quadrupole piece correcting the quadrupole GW losses of GR, which, based on [91], are expected to only have the same "plus" and "cross" polarizations. This enhanced dissipation of energy and angular momentum, in turn, will force the binary to inspiral faster than in GR, and therefore, leave an imprint in the GWs emitted through corrections to the rate at which the GW frequency increases during the inspiral. This GW phase shift will enable us to project bounds on sGB gravity that are similar in spirit but complementary to the analysis of [35]. In fact, because the merger leaves behind a "bald" Kerr black hole due to dynamical descalarization, the (scalar) energy flux is, in general, larger as compared to shift-symmetric sGB, where the remnant black hole always retains some of its hair. This suggests that strong observational bounds might be placed on this theory.
Having worked in the decoupling limit, a question naturally arises: what would we expect in the fully nonlinear regime of sGB gravity? It is known that nonlinear effects set an upper bound on the scalar field magnitude at the BH horizon [58], so that the domain of existence of scalarized BHs exhibits a very

narrow bandlike structure in the phase space spanned by BH mass and coupling β_2; see Fig. 2 of [32]. This means that case (d) would only occur for sufficiently small mass ratios such that both the initial binary and its final state remain in band. In general, however, comparable mass BH binaries could undergo an $\bar{s} + \bar{s} \to s$ process, in which two unscalarized BHs would merge, forming BH within the scalarization band, i.e., a dynamical BH scalarization. The descalarization of the BH remnant would also impact the GW emission during the ringdown. Specifically, the waveforms in Fig. 3.5 show that the ringdown time scales of scalar and tensorial modes are comparable. This suggests that one should expect to see the imprint of the descalarization onto the quasinormal mode spectra of the Kerr black hole in the nonlinear case. Performing these studies in practice would require a general, well-posed formulation of the time evolution equations outside the EFT approach [35, 92], small values of the coupling parameter [93, 94], or spherical symmetry [64, 95–97]. Finding such a formulation has proven challenging [98–101], although first results in this direction were presented in [102]. Our work motivates and paves the way for future studies of nonperturbative, beyond-GR effects in BH binaries, with potential implications to tests of GR with GW astronomy.

3.5 Research work II: Spin-induced dynamical scalarization, descalarization, and stealthness in scalar-Gauss-Bonnet gravity during a black hole coalescence

This section contains the article "*Spin-induced dynamical scalarization, descalarization, and stealthness in scalar-Gauss-Bonnet gravity during a black hole coalescence*" which was published in *Physical Review D* [6].

3.5.1 Abstract

Particular couplings between a scalar field and the Gauss-Bonnet invariant lead to spontaneous scalarization of black holes. Here we continue our work on simulating this phenomenon in the context of binary black hole systems. We consider a negative coupling for which the black-hole spin plays a major role in the scalarization process. We find two main phenomena: (i) dynamical descalarization, in which initially scalarized black holes form an unscalarized remnant, and (ii) dynamical scalarization, whereby the late merger of initially unscalarized black holes can cause scalar hair to grow. An important consequence for the latter case is that modifications to the gravitational waveform due to the scalar field may only occur post-merger, as its presence is hidden during the entirety of the inspiral. However, with a sufficiently strong coupling, we find that scalarization can occur before the remnant has even formed. We close with a discussion of observational implications for gravitational-wave tests of general relativity.

3.5.2 Introduction

The detection of GW produced by coalescing compact binaries by the LIGO-Virgo-Kagra Collaboration [37, 38, 103] have opened a new avenue to test GR in its strong-field, nonlinear regime [43, 104, 105]. In fact, the first three catalogs of observations have already been used to perform several null tests of GR [41–43, 106–112], as well as theory-specific tests [44, 113–120]. The latter have placed constraints on quadratic gravity theories [44, 116–119].

In these theories, a scalar field couples to a curvature scalar, which is quadratic in the Riemann tensor (see e.g. Ref. [61] for an overview). Well-known examples include coupling to the Pontryagin density or the Gauss-Bonnet (GB) invariant. The latter theories are often named sGB gravity. They can emerge in the low-energy limit of string theory (see, for instance, Refs. [46, 121, 122]), as well as through a dimensional reduction of Lovelock gravity [47], and belong to the wider class of Horndeski gravity theories [123, 124].

BH solutions in this theory have long been known to have a nontrivial scalar field (i.e., a "hair"), to which we can associate a monopole scalar charge that depends on the BH's mass and spin. When the BHs are found in a binary, their motion can lead to the emission of scalar dipole radiation, which in turn modifies the system's orbital dynamics and the GW signal with respect to GR's prediction. Such phenomenology has been explored with both post-Newtonian (PN) [88–90, 125–128] and numerical relativity [5, 35, 92, 102, 129, 130] techniques. The scalar field can also affect the post-merger signal, modifying the remnant BH's ringdown [131–136]. In sGB gravity, the presence of scalar hair depends on the functional form of the coupling between scalar field and the GB invariant.

More specifically, if the functional form of the coupling always has a non-vanishing first derivative, such as for a linear or exponential coupling, BHs are known to invariably have scalar hair [28–31, 49–51, 58, 59, 79, 80, 137–140]. Hence, the observation of GWs from BH binaries and mixed neutron star (NS)-BH binaries have allowed us to constrain the length scale at which the scalar-field-GB interaction becomes relevant to less than approximately one kilometer [44, 117–119].

In contrast, if the first derivative of the coupling function vanishes for some constant background scalar field, both scalarized and unscalarized BH solutions can exist [32, 33]. Depending on the length scale associated with the scalar-field-GB interaction, and the BH's mass [32, 33, 62] and spin [4, 65–67, 69–71, 141], the BH solutions of GR become unstable to scalar field perturbations, and the end-state of this instability is a *scalarized* BH [64]. This process is similar to spontaneous scalarization of NSs in scalar-tensor gravity [34, 52]. The difference lies in the fact that for NSs the scalar field is sourced by matter, while for BHs the scalar is sourced by the spacetime curvature alone. Thus, one could envision that the aforementioned GW constraints (such as e.g. [116]) can be avoided if scalarization occurs *right before merger, or possibly only after merger.*

Can such a scenario happen? Here we continue our previous work [5] and explore how the onset of scalarization plays out during binary BH mergers. As in our previous paper, we work in the decoupling approximation, i.e., we evolve the scalar field on a time-depenedent GR background. In Ref. [5], we studied a variety of possible processes for head-on BH collisions, as well as a quasi-circular inspiral-merger of equal mass non-spinning binaries using a positive sign of the scalar-field-GB coupling. We demonstrated the

existence of a process we coined *dynamical descalarization*, whereby initially scalarized BHs merged to form a larger remnant that descalarized because its GB curvature was too small to sustain the scalar hair. The alternative, the dynamical scalarization of the remnant, was not possible because its larger mass (compared to the initial BHs' masses) inevitably leads to a smaller GB curvature near the horizon.
However, for a negative sign of the coupling, the scalar field instability happens only for sufficiently rapidly-spinning BHs ("spin-induced scalarization") [4, 65–67, 71]. This leads to the following questions: (1) Does the formation of a highly spinning remnant cause spin-induced dynamical scalarization? If so, at what stage in the binary's evolution is the scalar hair excited? (2) Can the process of dynamical descalarization found in Ref. [5] be generalized to the negative coupling case? Here we address these questions with a new suite of binary BH simulations and negative sign of the coupling constant.
We find that indeed spin-induced descalarization and scalarization of the BH remnant are both possible. The spin-induced descalarization of initially scalarized, spinning BHs, extends and completes the work in Ref. [5]. The spin-induced scalarization of the remnant is a new result. For values of the coupling constant close to the scalarization threshold, the growth of the scalar field has a large instability time-scale. Therefore, scalarization only becomes significant significantly after the remnant BH's ringdown begins. We therefore now coin the term *stealth dynamical scalarization*, whereby the scalar field remains hidden throughout the full inspiral, merger and early ringdown evolution of the BH binary and is thus unconstrainable with GW observations.
In the remainder of this work we explain how we arrived at these conclusions. In Sec. 3.5.3 we review both scalarization and descalarization of BHs in sGB gravity. Next, in Sec. 3.5.4 we discuss our numerical methods and our numerical relativity simulations designed to answer our previously stated questions. In Sec. 3.5.5 we present our findings and we finish by discussing some of their observational implications in Sec. 3.5.6. We work with geometric units $G = 1 = c$.

3.5.3 Scalar Gauss–Bonnet gravity

Action and field equations

sGB gravity modifies GR via a nonminimal coupling between a real scalar field Φ and the GB invariant $\mathscr{G}$, as described by the action

$$S = \frac{1}{16\pi}\int \mathrm{d}^4x\sqrt{-g}\left[R - \frac{1}{2}\left(\nabla\Phi\right)^2 + \frac{\alpha_{\rm GB}}{4}f(\Phi)\,\mathscr{G}\right], \tag{3.16}$$

where R is the Ricci scalar, $g = \det(g_{\mu\nu})$ the metric determinant, $(\nabla\Phi)^2 = g^{\mu\nu}\nabla_\mu\Phi\nabla_\nu\Phi$ the scalar field kinetic term, and

$$\mathscr{G} = R^2 - 4R_{\mu\nu}R^{\mu\nu} + R_{\mu\nu\rho\sigma}R^{\mu\nu\rho\sigma}\,, \tag{3.17}$$

is the GB invariant, where $R_{\mu\nu\rho\sigma}$ and $R_{\mu\nu}$ are the Riemann and Ricci tensor respectively. The particular form of the theory is parametrized by the coupling function $f(\Phi)$ and the coupling constant $\alpha_{\rm GB}$ with units of [Length]^2.

As in our previous study [5], we work in the decoupling limit. That is, we neglect the backreaction of the scalar field onto the spacetime metric: the scalar field evolves on a dynamical, vacuum background spacetime of GR. The action (3.16) gives rise to the field equation for Φ

$$\Box\Phi = -\tfrac{1}{4}\alpha_{\rm GB} f'(\Phi)\mathscr{G}\,, \tag{3.18}$$

where a prime denotes a derivative with respect to Φ. Since we work in the decoupling limit, the d'Alembertian and the GB invariant are those of the time-dependent GR background.
The choice of the coupling function $f(\Phi)$ determines specific sGB models. As we already alluded to in Sec. 3.5.2, the models can be classified into two types depending on the properties of their BH solutions. We label models as *type I* if the derivative of the coupling function $f'(\Phi) \neq 0$. In this case, BH solutions always have scalar hair [28–31,49–51,58,59,79,80,137–140]. Examples of type I models include the dilatonic $f(\Phi) \propto \exp(\Phi)$ [31, 48, 49, 138] and shift-symmetric $f(\Phi) \propto \Phi$ [28–30, 50] coupling functions. We label models as type II if the derivative of the coupling function $f'(\Phi_0) = 0$, for some constant Φ_0. In this case, the theory admits the stationary vacuum BH solutions of GR, as proved by the no-hair theorem of [32], but also admits, when the theorem is violated, scalarized BHs. Examples include quadratic $f(\Phi) \propto \Phi^2$ [32] and Gaussian $f(\Phi) \propto \exp(\Phi^2)$ [33] coupling functions. Here we consider type II models only.

Scalarization of isolated black holes

In the second type of sGB model the onset of scalarization is found by linearizing (3.18) around the background BH spacetime, i.e., $\Phi = \Phi_0 + \delta\Phi$, where Φ_0 is a constant. This results in the scalar-field evolution equation

$$\left(\Box - m^2_{\rm eff}\right)\delta\Phi = 0\,, \tag{3.19}$$

with an effective mass squared

$$m^2_{\rm eff} := -\tfrac{1}{4}\alpha_{\rm GB} f''(\Phi_0)\,\mathscr{G}\,, \tag{3.20}$$

which can become tachyonically unstable; in other words, the BH can scalarize if $m^2_{\rm eff} < 0$ [32, 33]. This, however, is a necessary, but not sufficient condition for scalarization. The scalarization threshold can be calculated by finding a bound state solution, i.e, a time independent solution of (3.19) which is regular at the BH horizon and that vanishes at spatial infinity. By imposing these boundary conditions on $\delta\Phi$, the calculation of the scalarization threshold is reduced to a boundary value problem, with the dimensionless ratio between $\alpha_{\rm GB}$ and the BH's mass squared playing the role of the eigenvalue. The smallest eigenvalue provides the scalarization threshold for the "fundamental" (i.e., the nodeless solution) family of scalarized BHs, while the other eigenvalues determine the threshold for the formation of "excited states" (i.e., solutions with one or more nodes). We focus on the latter here. See Fig. 1 in Ref. [32] or Sec. 4.3 of Ref. [142] for further details. To be more concrete, here we consider a quadratic coupling function,

$$f(\Phi) = \Phi^2\,. \tag{3.21}$$

The coupling strength is determined by the dimensionless constant[5]

$$\beta = \alpha_{\rm GB}/\mathscr{M}^2\,, \tag{3.22}$$

where $\mathscr{M}$ is the characteristic mass of the system. The effective mass then becomes

$$m_{\rm eff}^2 = -\tfrac{1}{2}\beta\,\mathscr{M}^2\,\mathscr{G}\,. \tag{3.23}$$

If $\mathscr{G}$ is positive-definite in the BH exterior, then the instability can only happen for positive β. However, if $\mathscr{G}$ is negative, at least in some regions outside the horizon, then the instability can also be triggered with a negative β. For example, consider the Kerr metric, for which the GB invariant in Boyer-Lindquist coordinates $(t, \bar{r}, \theta, \varphi)$ is given by

$$\mathscr{G}_{\rm Kerr} = \frac{48m^2}{(\bar{r}^2+\sigma^2)^6}\left(\bar{r}^6 - 15\bar{r}^4\sigma^2 + 15\bar{r}^2\sigma^4 - \sigma^6\right)\,, \tag{3.24}$$

where $\sigma = a\cos\theta$ and $a = J/m$ is the angular momentum per unit mass of the BH. When the dimensionless spin $\chi = a/m < 0.5$, $\mathscr{G}$ is positive everywhere outside the event horizon and so scalarization can only take place if β is positive. This also holds true in the limiting case of a Schwarzschild BH. However, for sufficiently rapidly rotating BHs (i.e., those with $\chi = a/m \geqslant 0.5$), the GB invariant can become negative in the exterior of the outer BH horizon in regions along the rotation axis [143]. Hence, spin can induce scalarization of BHs if β is negative and $\chi \geqslant 0.5$ [4, 65–67, 71, 141] and suppress it if β is positive [69, 70]. One may note that scalarized solutions in quadratic sGB gravity with a positive coupling constant, $\beta > 0$, are unstable to radial perturbations [144]. Although this is true, such BHs can be stabilized by including higher-order scalar terms in the coupling $f(\Phi)$ [145,146], through the addition of scalar field self-interactions while retaining the quadratic form of $f(\Phi)$ [62], or through the addition of a coupling of scalar field to the Ricci scalar [147, 148]. Since we are investigating the onset of scalarization, it is unnecessary to include such terms and so we focus only on the quadratic coupling case here.

Scalarization and Descalarization in black hole binaries

What could be the consequences of scalarization in BH binaries? To answer this question, in Ref. [5] we performed the first numerical relativity simulations of both head-on collisions and quasi-circular inspirals of BHs in quadratic sGB gravity with a positive coupling β. We identified a new effect, that we named *dynamical descalarization*, in which initially non-spinning scalarized BHs shed-off completely their scalar hair after the merger. This is a result of the comparatively weaker curvature generated near the horizon of the resulting larger remnant BH. Consequently, several possible dynamical processes were discovered for particular combinations of mass ratio and coupling strength, as illustrated in Fig. 1 of Ref. [5]. We can contrast this with similar simulations in type I theories in which the remnant BH always retains some scalar hair [35].

[5]With respect to the notation of Ref. [5], we are omitting the subscript "2" and fixing $\bar{\beta} = 1$.

Here we extend our previous work by considering negative coupling $\beta < 0$ values. For this case the spins of the initial and/or remnant BHs play a crucial role in the development of the scalar field of the system due the possibility of spin-induced scalarization. Specifically, the formation of negative GB regions close to merger causes the remnant to scalarize, a process that we call *spin-induced dynamical scalarization*. Additionally, we also demonstrate *spin-induced dynamical descalarization* – the spin analogue of the aforementioned dynamical descalarization mechanism – as high-spinning binary components merge to produce a lower spin remnant that cannot support the instability.

3.5.4 Simulating binary black holes in sGB gravity – Methods and setup

Time evolution formulation

We investigate the dynamics of the sGB scalar field, determined by its equation of motion (3.18), and sourced by a binary BH background spacetime. We perform a series of time evolution simulations in $3+1$ dimensions by adopting standard numerical relativity techniques; see e.g. Ref. [8]. That is, we foliate the four-dimensional spacetime into three-dimensional spatial hypersurfaces Σ_t, parametrized by a time parameter t, with an induced spatial metric γ_{ij}. We introduce the timelike vector n^μ that is orthonormal to the hypersurface. Then, the spacetime metric $g_{\mu\nu}$ can be decomposed as

$$\begin{aligned} \mathrm{d}s^2 &= g_{\mu\nu}\mathrm{d}x^\mu \mathrm{d}x^\nu \\ &= -\left(\alpha^2 - \beta^k\beta_k\right)\mathrm{d}t^2 + 2\gamma_{ij}\beta^i \mathrm{d}t\mathrm{d}x^j + \gamma_{ij}\mathrm{d}x^i\mathrm{d}x^j \,, \end{aligned} \tag{3.25}$$

where α is the lapse function (not to be confused with the dimensional coupling constant $\alpha_{\rm GB}$) and β^i is the shift vector (not to be confused with the dimensionless coupling constant β). Finally, we introduce the extrinsic curvature $K_{ij} = -\frac{1}{2\alpha}\left(\partial_t - \mathcal{L}_\beta\right)\gamma_{ij}$, where $\mathcal{L}_\beta$ is the Lie-derivative along the shift vector β^i.
To simulate the background BH binary we write Einstein's equations as a Cauchy problem and adopt the Baumgarte-Shapiro-Shibata-Nakamura formulation [9, 10] together with the moving puncture gauge conditions [72, 73]. We prepare initial data describing a quasi-circular binary of two spinning BHs with the Bowen-York approach [76, 77].
To evolve the scalar field Φ in this time-dependent GR background, we write its field equation (3.18) as a set of time evolution equations. Therefore, we introduce the scalar field's momentum $K_\Phi = -\frac{1}{\alpha}\left(\partial_t - \mathcal{L}_\beta\right)\Phi$ and we apply the spacetime decomposition to (3.18). This procedure gives the equations

$$\left(\partial_t - \mathcal{L}_\beta\right)\Phi = -\alpha K_\Phi \,, \tag{3.26a}$$

$$\begin{aligned} \left(\partial_t - \mathcal{L}_\beta\right)K_\Phi &= -D^i\alpha D_i\Phi \\ &\quad - \alpha\left(D^i D_i\Phi - K K_\Phi + \tfrac{1}{4}\alpha_{\rm GB} f'\mathscr{G}\right) \,, \end{aligned} \tag{3.26b}$$

where D_i, $\mathscr{G}$ and $K = \gamma^{ij}K_{ij}$ are the covariant derivative with respect to the induced metric, the four-dimensional GB invariant and the trace of the extrinsic curvature of the background spacetime.
We initialize the scalar field to represent multiple scalarized BHs. For simplicity, we neglect the scalar field's initial linear and angular momentum, because it relaxes to its equilibrium configuration within about

$100M$ from the start of the evolution, i.e., within approximately one orbit [35, 101]. Since the scalar field equation (3.18) is linear, we can superpose the static bound-state solution anchored around an isolated BH. For N BHs, we then have

$$\Phi|_{t=0} = \sum_{a=1}^{N} \Phi_{(a)}\,, \quad K_\Phi|_{t=0} = 0\,, \tag{3.27}$$

where the subscript (a) labels the a-th BH. The bound state of the sGB scalar field around an isolated, non-spinning BH with a coupling of the form (3.21) was obtained numerically in Ref. [32]. We approximate this solution with the fit

$$\Phi_{(a)}\big|_{t=0} = \frac{m_{(a)} r_{(a)}}{\varrho^2_{(a)}} \left[c_1 + c_2 \frac{m_{(a)} r_{(a)}}{\varrho^2_{(a)}} + c_3 \frac{(m_{(a)} r_{(a)})^2}{\varrho^4_{(a)}} \right] , \tag{3.28}$$

where $\varrho_{(a)} = m_{(a)} + 2\, r_{(a)}$, $r_{(a)}$ is field point distance from the location of the a-th BH in quasi-isotropic radial coordinates of the background spacetime, $m_{(a)}$ is the mass of the a-th BH, and $c_1 = 3.68375$, $c_2 = 4.97242$, $c_3 = 2.29938 \times 10^2$ are fitting constants, where we corrected a misprint in c_3 in Ref. [5].

Code description

We performed the simulations with Canuda [149], our open-source numerical relativity code for fundamental physics [5, 35, 150, 151]. Canuda is fully compatible with the Einstein Toolkit [82, 152, 153], a public numerical relativity software for computational astrophysics. The Einstein Toolkit is based on the Cactus computational toolkit [154, 155] and uses the Carpet driver [83, 156] to provide boxes-in-boxes adaptive mesh refinement (AMR) as well as MPI parallelization. To evolve the field equations we employ the method-of-lines. Spatial derivatives are typically realized by fourth-order finite differences (with sixth order also being available) and for the time integration we use a fourth-order Runge-Kutta scheme.

The background spacetime, consisting of two spinning BHs in a quasi-circular orbit, is initialized with the TwoPunctures spectral code [157] that solves the constraint equations of GR with the Bowen-York approach [76, 77]. We evolve Einstein's equations using Canuda's modern version of the Lean thorn [158] that implements the Baumgarte-Shapiro-Shibata-Nakamura equations with the moving puncture gauge. The sGB scalar field evolution equations (3.26) and its initial data (3.28) are implemented in Canuda's arrangement Canuda_EdGB_dec. Details of the implementation are described in Refs. [5, 35, 80]. To analyse the numerical data, we compute the Newman-Penrose scalar Ψ_4 as a measure for gravitational radiation and we extract the gravitational and scalar field multipoles on spheres of constant extraction radius $r_{\rm ex}$ using the QuasiLocalMeasures thorn [159]. We find the BHs' apparent horizons and compute their properties with the AHFinderDirect thorn [160, 161].

Setup of simulations

To investigate spin-induced dynamical scalarization or descalarization in binary BH mergers, we have performed a series of simulations of equal-mass, quasi-circular inspirals for the negative coupling case, $\beta < 0$. The initial BHs have either zero spin or a spin (anti-)aligned with the orbital angular momentum. To choose the values of the coupling constant β in our simulations, we used the numerical data found in Ref. [4] (cf. Supplemental Material, Table I) to obtain a fitting formula that returns the value of β at the threshold for spin-induced scalarization as a function of the dimensionless spin χ; we will refer to this threshold value as the *critical value* of the dimensionless coupling constant. The critical value for the coupling constant satisfies the scaling

$$\beta_{\rm c}(m/M,\chi) = (m/M)^2\,\beta_{\rm c}(1,\chi)\,, \tag{3.29}$$

where m is a place-holder for either the individual masses of the binary $m_{(a)}$ or the final remnant mass m_f, while $M = m_1 + m_2$ is the initial total mass of the binary. The quantity $\beta_{\rm c}(1,\chi)$ is the critical value of the coupling that leads to scalarization for a BH of mass $1M$ and dimensionless spin χ, namely

$$\beta_{\rm c}(1,\chi) = -\frac{0.422}{(|\chi|-1/2)^2} + 1.487\,|\chi|^{7.551}\,, \tag{3.30}$$

where $\beta_{\rm c}(1,\chi)$ diverges as $|\chi|$ tends to 0.5, in agreement with Ref. [66]. For instance, if we wish to scalarize the initial components of the binary, and if the mass ratio is unity, then $m_{(a)} = M/2$, and $\beta_{{\rm c},\,(a)}(1/2,\chi_{(a)}) = (1/4)\,\beta_{\rm c}(1,\chi_{(a)})$. In Fig. 3.6, we show (3.30) and compare it against the numerical results of Ref. [4]. We obtain relative errors smaller than 15% in the range $0.5 \leqslant \chi < 1$ and less than 5% for $\chi \lesssim 0.74$. We use (3.29) as reference to choose the values of β to probe scalarization of either one (or both) of the initial binary components or of the remnant BH.

Run	d/M	χ_1	χ_2	χ_f	β	$\beta_{{\rm c},1}$	$\beta_{{\rm c},f}$	process
Setup A	10	0	0	0.68	-14.30	–	-12.96	$\bar{s} + \bar{s} \to s_\uparrow$
Setup B	10	-0.6	-0.6	0.48	-11.00	-10.55	–	$s_\downarrow + s_\downarrow \to \bar{s}_\uparrow$

Table 3.1: Setup of the simulations of equal-mass, quasi-circular BH binaries. We show the initial separation d/M, the initial dimensionless spins χ_1 and χ_2 of each binary component, the dimensionless spin χ_f of the remnant, and the dimensionless coupling constant β used in the simulations. For reference, we also show the critical values to scalarize the initial ($\beta_{{\rm c},1} = \beta_{{\rm c},2}$) or final ($\beta_{{\rm c},f}$) BHs, calculated using Eqs. (3.29) and (3.30). The last column summarizes the process that unfolds during the simulation. We use $\bar{s}$ and s to denote unscalarized and scalarized states, respectively, and the subscript $\uparrow$ ($\downarrow$) indicates spin aligned (anti-aligned) with the orbital angular momentum, which is assumed to be $\uparrow$. See Fig. 3.7 for additional details.

Here, we present two key simulations, listed in Table 3.1 and illustrated in Fig. 3.7, with the following setups:

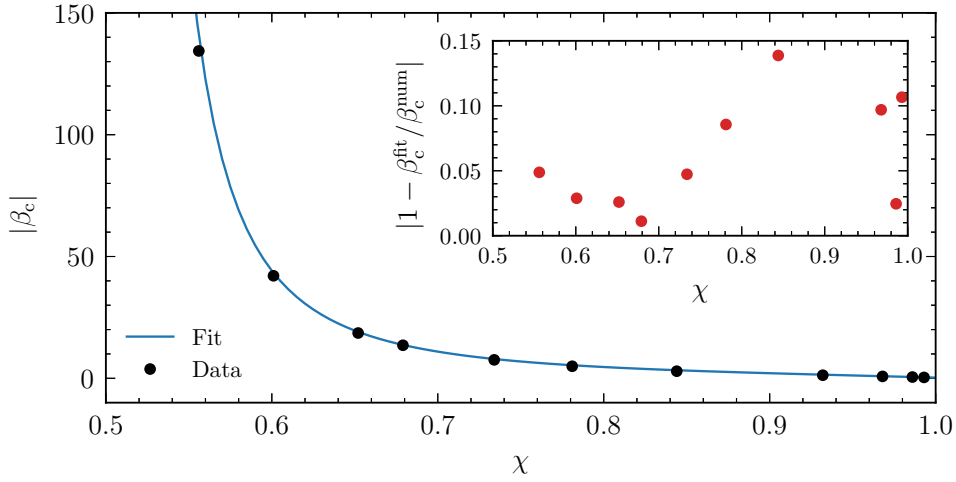

Figure 3.6: Absolute value of the critical coupling, β_c, for spin-induced scalarization of a single BH as a function of the dimensionless spin χ. We show the numerical data of Ref. [4] and the fitting formula (3.30). The inset shows the relative error between the fit and the data. We see that the error is less than 15% in the range $0.5 \leqslant \chi < 1$ and less than 5% for $\chi \lesssim 0.74$.

Setup A in Table 3.1 is designed to address our first question: does the formation of a highly spinning remnant cause spin-induced dynamical scalarization? Here, we consider a binary of initially non-spinning, unscalarized BHs that merges into a spinning, scalarized remnant as illustrated in Fig. 3.7. The BHs complete 10 orbits prior to their merger at $t_M = 927M$, as estimated from the peak in the gravitational (quadrupole) waveform; see the bottom panel of Fig. 3.8. When the coupling β is negative, the squared effective mass (3.20) of the initial BHs (with $\chi = 0$) is positive definite everywhere outside their horizons, and so they are initially not scalarized. The final BH has a dimensionless spin of $\chi_f = 0.68$ and mass $m_f \sim M$. For a BH with these parameters, the critical coupling is $\beta_{c,f} \approx \beta_c(1, 0.68) \approx -12.96$; cf. (3.29). In our simulation we chose $|\beta| > |\beta_{c,f}|$ such that the remnant BH is indeed scalarized. In this simulation, we initialize the scalar field according to (3.28) around each binary component. The scalar field disperses early in the simulation, leaving each BH unscalarized and a negligible, but nonvanishing ambient scalar field in the numerical grid. Notice that if we had set $\Phi|_{t=0} = 0$, there would be no scalar field dynamics [see (3.18)].

Setup B in Table 3.1 is designed to address our second question: is the dynamical descalarization found in Ref. [5] a general phenomenon? Is there a spin-induced dynamical descalarization? Here we consider a binary of initially rotating, scalarized BHs with spins $\chi_1 = \chi_2 = -0.6$, anti-aligned with the orbital angular momentum as illustrated in the RHS of Fig. 3.7. Each of the components of the binary has a mass $m_1 = m_2 = M/2$. Inserting these parameters in ((3.29)), we find $\beta_{c,1} = \beta_{c,2} = \beta_c(1/2, -0.6) \approx -10.55$. In our simulations, we set $|\beta| \gtrsim |\beta_c(1/2, -0.6)|$ such that the initial BHs are scalarized. The initial BHs merge into a final rotating BH that has a spin aligned with the orbital angular momentum of the previously inspiralling system, with a spin magnitude $\chi_f = 0.48$. This value is below the threshold for spin-induced

scalarization, and so the remnant BH does not support scalar hair.

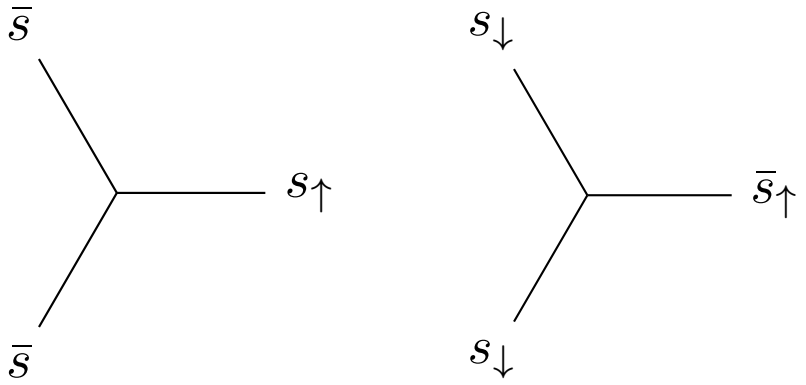

Figure 3.7: Binary BH simulations, where s ($\bar{s}$) stands for initial or final BH states that are scalarized (unscalarized) and with spin along the positive ($\uparrow$) or negative ($\downarrow$) z-direction (i.e., aligned or anti-aligned with the orbital angular momentum, assuming the latter is $\uparrow$). BH states without an arrow are non-spinning. The LHS of Fig. 3.7 illustrates a process of spin-induced dynamical scalarization: two initially unscalarized BHs produce a spinning, scalarized remnant. The RHS of Fig. 3.7 illustrates a process of dynamical descalarization: two initially rotating, scalarized BHs whose spin is anti-aligned with the orbital angular momentum merge into a rotating BH with a smaller spin magnitude. Consequently, the remnant descalarizes.

To show that our qualitative results are robust for a large variety of BH spin parameters, we have performed a series of additional simulations listed in Table C.1 of Appendix C. All simulations presented in Tables 3.1 and C.1 have the same grid setup: the numerical domain was composed of a Cartesian box-in-box AMR grid structure with seven refinement levels. The outer boundary was located at $255.5M$. We use a grid spacing of $\mathrm{d}x = 0.7M$ on the outermost refinement level to ensure a sufficiently high resolution in the wave zone. The region around the BHs has a resolution of $\mathrm{d}x = 0.011M$. To validate our code and estimate the numerical error of our simulations, we performed convergence tests for our most demanding simulation with $\chi_{1,2} = -0.6$, corresponding to Setup B in Table 3.1. The relative error in the gravitational quadrupole waveform is $\Delta\Psi_{4,22}/\Psi_{4,22} \leqslant 0.8\%$, while the relative error of the scalar charge accumulates to $\Delta\Phi_{00}/\Phi_{00} \leqslant 30\%$ in the last orbits before merger; the latter is $\Delta\Phi_{00}/\Phi_{00} \leqslant 15\%$ in the merger and ringdown phase. The large error in the scalar field, close to the BHs merger, is a consequence of the exponential growth of the scalar field during inspiral. As our investigation is of a qualitative nature, this cumulative error is not a cause of concern for our results. However, a future quantitative analysis would have to address this issue. See Appendix C.1 for details.

3.5.5 Results

Spin-induced dynamical scalarization

Here we present key results obtained with simulation Setup A (see Sec. 3.5.4), corresponding to the LHS of Fig. 3.7. In particular, we show that an initially unscalarized BH binary can indeed form a hairy, rotating remnant.

This process is illustrated in the top panel of Fig. 3.8, where we present the time evolution of the scalar field's monopole charge, $r_{\rm ex}\Phi_{00}$, measured at $r_{\rm ex} = 100M$, and shifted in time such that $(t-r_{\rm ex}-t_{\rm M})/M = 0$ indicates the time of merger. The scalar field perturbation that is initially present in our simulations remains small during the entire inspiral. See, for instance, the amplitudes $r_{\rm ex}\Phi_{\ell m}$ at $(t - r_{\rm ex} - t_{\rm M})/M < 0$ which are of $\mathcal{O}(10^{-4})$ or $\mathcal{O}(10^{-6})$. Yet, we see an exponential growth of the scalar charge, $r_{\rm ex}\Phi_{00} \sim e^{\omega_{\rm I,00}t}$, that exceeds the background fluctuations, approximately $100M$ after the merger. We estimate the growth rate (for our choice of β) to be $M\omega_{\rm I,00} \sim 0.062$ by fitting to the numerical data. We show this with the dotted red line in the top and middle panels.

We find a similar behavior in the scalar field quadrupole, as shown in the middle panel of Fig. 3.8. That is, both the axisymmetric $(\ell, m) = (2, 0)$ and the $(\ell, m) = (2, 2)$ multipoles are excited and grow exponentially with a rate of $M\omega_{\rm I} \sim 0.062$. For the form of the coupling function considered here, the rate appears to be independent of the (ℓ, m) multipole and is determined by the coupling constant β, as we further discuss later. The quadrupole scalar field is absent in the initial data because we initialized the scalar field with a spherically symmetric distribution around each of the BHs. Hence, the scalar field quadrupole we observe is caused by the "stirring" of the ambient scalar field due to the dynamical binary BH spacetime, which has a quadrupole moment. These Φ_{2m} multipoles also become unstable eventually, but at a later time relative to the monopole, as is evident by comparing the top and middle panels of Fig. 3.8. The exponential growth of the Φ_{2m} multipoles is consistent with the findings in Refs. [65, 67], showing that higher-ℓ and $m \neq 0$ scalar field multipoles can also become unstable.

All of these results beg for the following questions: at what stage in the binary's evolution is the scalar field instability induced? Is it due to the orbital angular momentum at the late inspiral or is it due to the angular momentum of the remnant BH? As we discussed in Sec. 3.5.3, a necessary (but not sufficient) condition for the tachyonic instability to occur is for the GB invariant to become negative outside the BH horizon in the $\beta < 0$ case; see (3.23). To address these questions, we inspect the behavior of the GB invariant at different stages throughout the evolution.

In Fig. 3.9 we show a close-up of the GB invariant's (top panel) and the scalar field's (bottom panel) profiles along the z-axis, parallel to the orbital angular momentum, at different time snapshots throughout the evolution. In Fig. 3.10 we show the GB invariant $\mathscr{G}$ together with snapshots of the scalar field Φ in the xz-plane, perpendicular to the orbital plane of the binary. The snapshots correspond to time instants during the inspiral (top left), half an orbit before merger (top right), at the formation of the common apparent horizon (CAH) (bottom left) and about $200M$ after the merger (bottom right). The color map represents the scalar field amplitude and is shared among all panels, while the contours are isocurvature

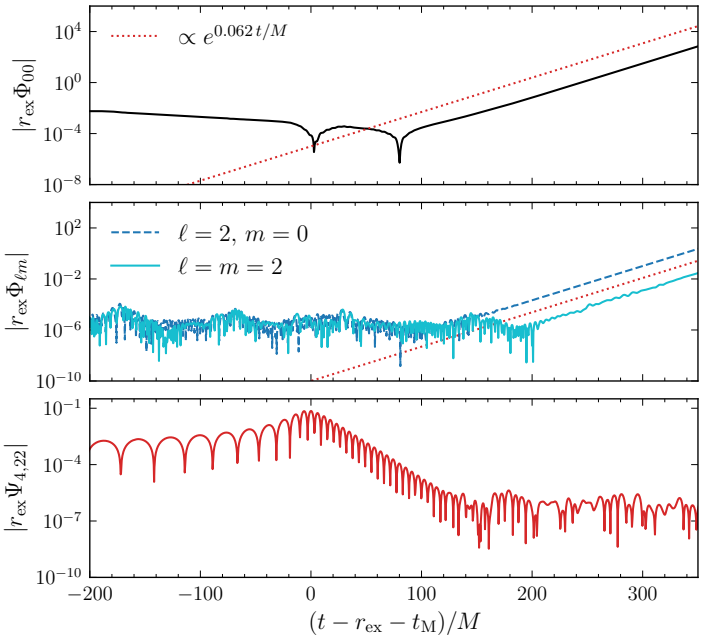

Figure 3.8: Evolution of the scalar field monopole (top panel), scalar field $\ell = 2$ multipoles (middle panel) and the gravitational waveform of the background spacetime (bottom panel) for Setup A in Table 3.1. We rescale the multipoles by the extraction radius $r_{\rm ex} = 100M$, and shift them in time such that $(t - r_{\rm ex} - t_{\rm M})/M = 0$ indicates the time of merger, determined by the peak of the gravitational waveform.

levels $|\mathscr{G}M^4| = \{1, 10^{-1}, 10^{-2}, 10^{-3}\}$, with positive (negative) values of $\mathscr{G}$ in black (red). We also show the location of the individual BHs using their apparent horizons, represented as ellipses with center, semi-major and semi-minor axes given by the centroid, maximum and minimum radial directions as obtained with the AHFinderDirect thorn [160, 161]. We do not show the evolution of $\mathscr{G}$ in the equatorial plane because we did not observe negative regions forming on this plane throughout the entire simulation.

During the early inspiral, the GB invariant is positive around the individual, non-spinning BHs, and the scalar field remains small across the numerical grid as can be seen in the top left panel of Fig. 3.10. However, about half an orbit before merger, we see the formation of regions between the two BHs where the GB invariant is negative; see top right panel of Fig. 3.10 and top panel of Fig. 3.9, $t = 904M$ curve. By the time $t = 904M$, the effective mass squared defined in (3.23) has become negative and this, we re-emphasize, is a necessary, but not sufficient condition for the tachyonic instability to occur.

As the BHs merge and the system settles to a final, rotating BH, the GB invariant remains negative along the z-axis, which now coincides with the remnant BH's rotation axis. This is illustrated in the bottom panels of Fig. 3.10, which correspond to the instant of the formation of the CAH (bottom left) and to about $200M$ after the merger (bottom right). In response, the scalar field grows exponentially as can be seen in its profiles shown in the bottom panel of Fig. 3.9 for different times after the CAH has formed. The scalar field assumes a predominantly dipolar spatial distribution along the BH's spin axis, a consequence of the regions where the GB invariant is negative. We note that the scalar field continues to grow instead

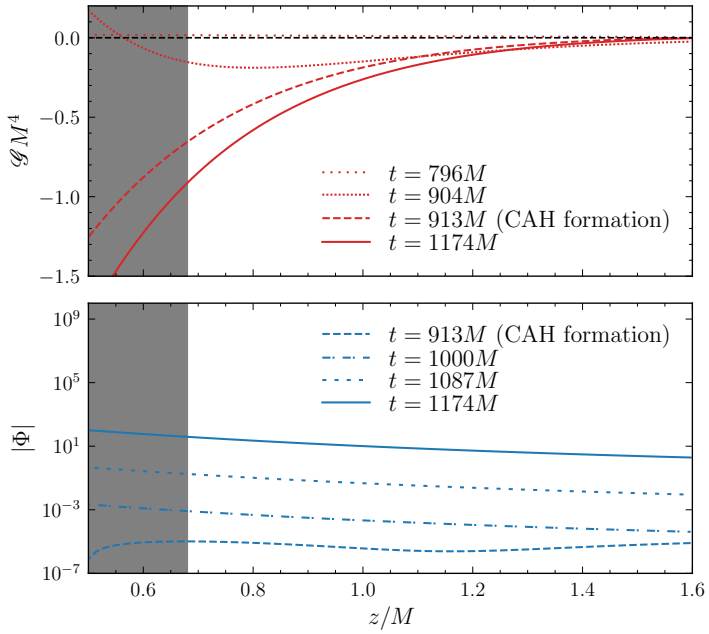

Figure 3.9: Profiles of the GB invariant (top panel) and of the scalar field (bottom panel), corresponding to Setup A in Table 3.1, along the z-axis in a close-up region near the CAH. The curves correspond to different times throughout the evolution. The shaded region indicates the CAH, shown $t = 100M$ after its formation when the final BH has relaxed to its stationary state. The GB invariant becomes negative during the BHs' last orbit before merger, and settles to its profile around the final rotating BH with dimensionless spin $\chi_f = 0.68$. In response, the scalar field becomes unstable.

of settling to a stationary bound state because the magnitude of the coupling is larger than the critical value for spin-induced scalarization for the final BH with spin $\chi_f = 0.68$; see Table 3.1.

To verify that the regions of negative GB curvature before the merger can induce the instability, we repeated the simulation of Setup A with a smaller initial BH separation of $d = 6M$ and a large-in-magnitude coupling constant $\beta = -10^3$; see Setup A1 in Table C.1. Although this choice of coupling, with $|\beta| \gg |\beta_{c,f}| = |\beta_c(1, 0.68)|$, may appear unphysical[6] it has the desired effect of being able to cause the instability before the merger and with a short time-scale; both effects are controlled by $|\beta|$.

This can be seen in Fig. 3.11, where we show the evolution of the scalar field multipoles, and in Fig. 3.12, where we show the field's profile along the rotation axis. Indeed, shortly after the GB invariant becomes negative, the scalar field grows exponentially and exceeds the magnitude of its background fluctuations at about $t = 20M$ before the CAH is first found.

In summary, if $|\beta|$ is large enough, the BHs' late inspiral and merger may be affected by the sGB scalar field. However, for $|\beta|$-values near the scalarization threshold, the inspiral and merger of initially unscalarized

[6]Such a large value of $|\beta|$ may be unphysical because the phase space of nonlinear BH solutions (i.e., including backreaction) has a band structure [32]: given a fixed value of M there is a maximum value of $|\beta|$ for which scalarized BHs exist.

The domain of existence of scalarized BHs depends on $f(\Phi)$, the BH mass, and its spin. Thus, if this β is physical requires a careful, nonlinear analysis. Here we focus only on the scalarization threshold.

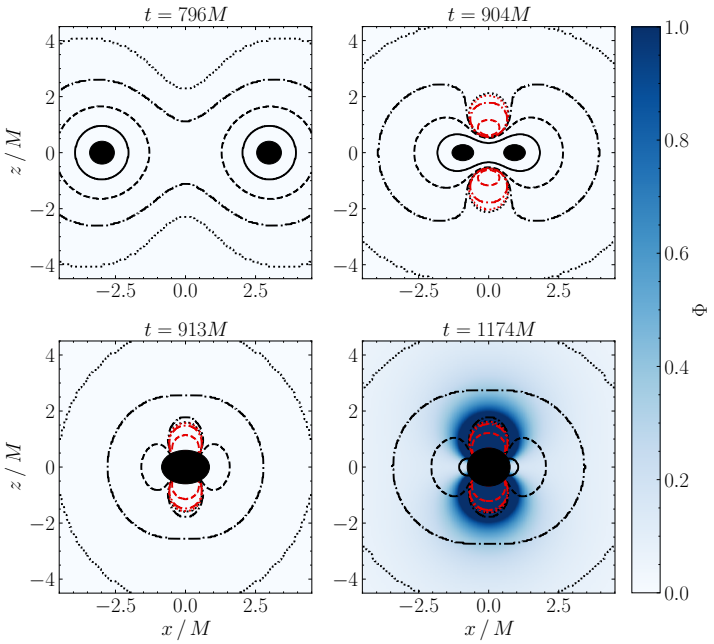

Figure 3.10: Snapshots of the scalar field, Φ, and the GB invariant in the xz-plane corresponding to Setup A in Table 3.1. The color map indicates the amplitude of the scalar field. The isocurvature contours of the GB invariant correspond to $|\mathscr{G}M^4| = 1$ (solid line), $|\mathscr{G}M^4| = 10^{-1}$ (dashed line), $|\mathscr{G}M^4| = 10^{-2}$ (dot-dashed line), $|\mathscr{G}M^4| = 10^{-3}$ (dotted line), Black (red) lines correspond to positive (negative) values of $\mathscr{G}$. We show the inspiral (top left), half an orbit before merger (top right), formation of the first CAH (bottom left) and about $200M$ after the merger.

BH binaries, and their GW emission, are identical to that of GR and imprints of the sGB scalar field only appear during the late ringdown. Such effects may be very difficult (if not impossible) to detect, and this is what we refer to as *stealth scalarization*.

Spin-induced dynamical descalarization

In this section we present our key results obtained with simulation Setup B in Table C.1 (see Sec. 3.5.4), illustrated in Fig. 3.7. The setup corresponds to two initially rotating, scalarized BHs (whose spin is anti-aligned with the orbital angular momentum) that produce a unscalarized remnant with a spin magnitude below the scalarization threshold for any choice of the coupling constant.

In Fig. 3.13 we show snapshots of the scalar field and the GB invariant in the xz-plane, perpendicular to the binary's orbital plane, during the inspiral (top left), half an orbit before the merger (top right), at the merger (bottom left) and about $t = 100M$ after the merger (bottom right). We illustrate the location of the BHs by their apparent horizons. The color-coding represents the amplitude of the scalar field and is shared among all panels. The contours represent the isocurvature lines $|\mathscr{G}M^4| = \{1, 10^{-1}, 10^{-2}, 10^{-3}\}$, with positive (negative) values shown in black (red). The spin magnitude of the two inspiraling BHs is sufficiently large to yield a GB invariant that has negative regions outside the BHs' horizon. Combined

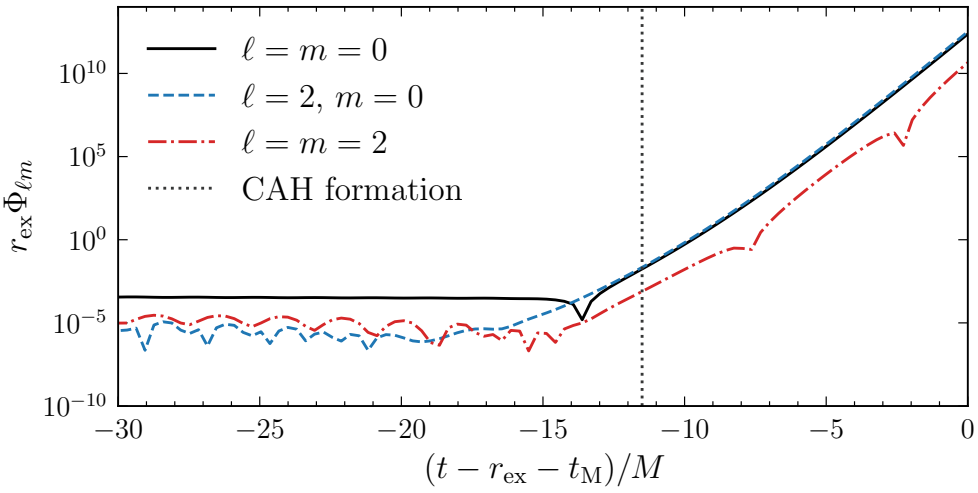

Figure 3.11: Evolution of the $\ell = m = 0$ (solid line), $\ell = 2$, $m = 0$ (dashed line) and $\ell = m = 2$ (dot-dashed line) scalar field multipoles for the coupling $\beta = -10^3$; cf. Setup A1 in Table C.1. We rescale the multipoles by the extraction radius $r_{\rm ex} = 50M$ and shift them such that $(t - r_{\rm ex} - t_{\rm M})/M = 0$ indicates the time of merger determined by the peak in the gravitational waveform. For comparison we also show the formation of the CAH (dotted line). We observe that the scalar field grows exponentially about $20M$ prior to the merger.

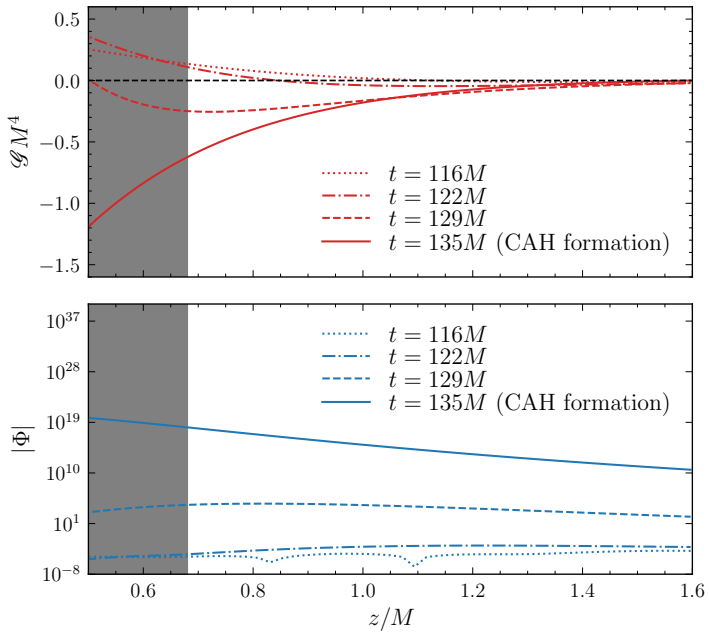

Figure 3.12: Same as Fig. 3.9, but for Setup A1 in Table C.1. We see that the GB invariant (top panel) becomes negative and triggers the excitation of the scalar field (bottom panel) before the formation of the CAH, indicated by the gray region.

with our choice of $|\beta|$, the BHs sustain a scalar field bound state, as shown in the top left panel of Fig. 3.13 and the BHs carry a scalar "charge" during the inspiral. As the BHs merge, they form a single, rotating

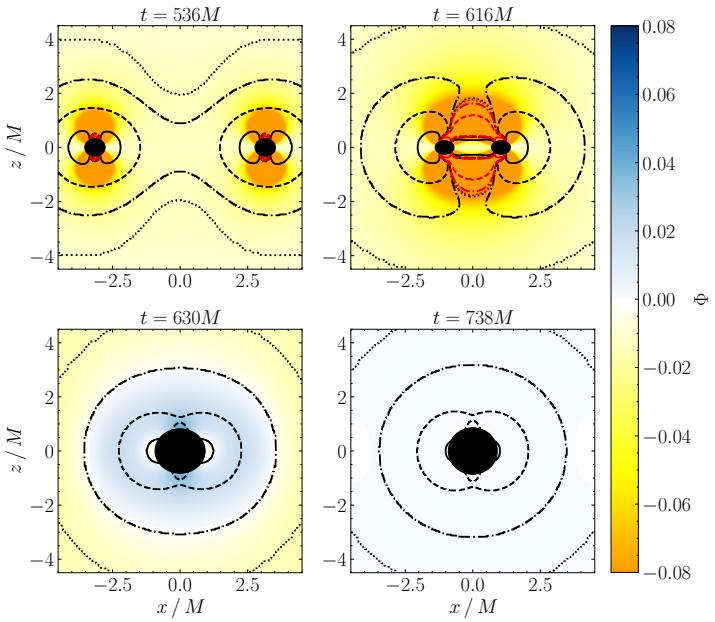

Figure 3.13: Snapshots of the scalar field, Φ, and the GB invariant, $\mathscr{G}$, in the xz-plane, corresponding to Setup B in Table C.1. The color map represents the amplitude of the scalar field. The isocurvature contours indicate the magnitude of the GB invariant with $|\mathscr{G}M^4| = 1$ (solid line), $|\mathscr{G}M^4| = 10^{-1}$ (dashed line), $|\mathscr{G}M^4| = 10^{-2}$ (dot-dashed line), $|\mathscr{G}M^4| = 10^{-3}$ (dotted line), with positive (negative) values shown in black (red). We show the inspiral (top left), half an orbit before merger (top right), $10M$ after the CAH formation (bottom left) and about $100M$ after the merger (bottom right).

BH which has a spin aligned with the orbital angular momentum and a magnitude of $\chi_f = 0.48$. For this spin magnitude, the GB invariant is positive everywhere outside the BH's horizon, as shown in the bottom row of Fig. 3.13. As a consequence, the effective mass-squared becomes positive everywhere in the BH's exterior and the scalar field bound states are no longer supported. That is, the scalar field dissipates, and the BH dynamically descalarizes, in agreement with the no-hair theorem of Ref. [32][7].

These phenomena can also be seen in Fig. 3.14, where we show the profiles of the GB invariant (top panel) and of the scalar field (bottom panel) along the z-axis (parallel to orbital angular momentum) for several instants during the evolution. The shaded region indicates the apparent horizon of the final BH. The GB invariant remains negative outside the individual BHs during their (late) inspiral. Only when the CAH first forms, does the GB invariant become positive everywhere outside the remnant BH's horizon. At this point, the effective mass-squared becomes positive, the tachyonic instability that kept each BH scalarized switches off, and the scalar field dissipates as shown in the bottom panel of Fig. 3.14.

[7] One might wonder if the final rotating BH may become superradiantly unstable due to the presence of an effective mass for the scalar field Φ. While the necessary conditions are satisfied [162–164], the instability for a BH of $\chi_f \lesssim 0.5$ would evolve on e-folding timescales much longer than those studied here [165, 166]; see Ref. [65] for a comparison against spin-induced scalarization. Moreover, if backreaction of Φ onto the metric was included, the BH mass and spin would decrease until the superradiance condition is saturated and the instability is turned off. Then, the scalar decays and the end-state is a BH with no scalar field.

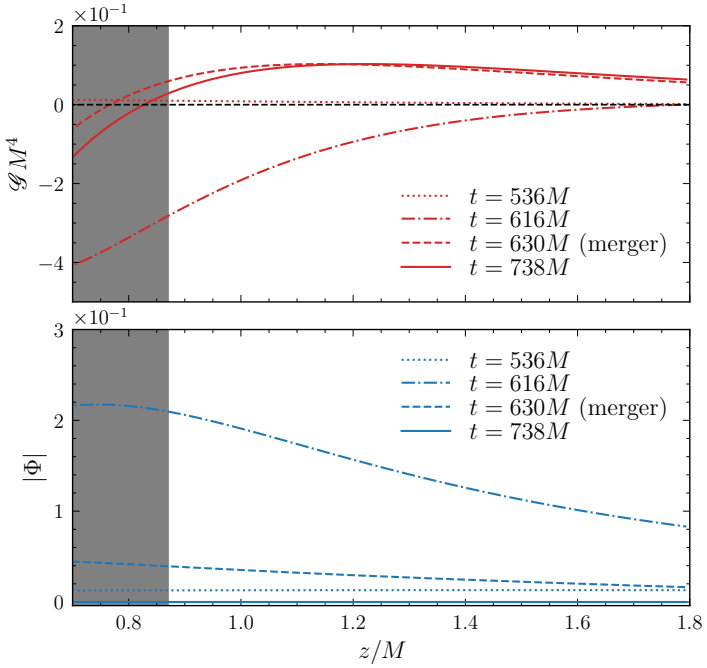

Figure 3.14: Profiles of the GB invariant (top panel) and of the scalar field (bottom panel) for Setup B in Table C.1 along the z-axis. The lines correspond to different times during the evolution. The shaded region indicates the CAH, shown $100M$ after its formation. The GB invariant becomes positive outside the horizon when the CAH is first formed. Consequently, the scalar field magnitude decreases and the remnant BH descalarizes.

Does the presence of scalar charges during the inspiral produce scalar radiation? The answer is affirmative as can be seen in Fig. 3.15 where we show the time evolution of the scalar field monopole (top panel) and quadrupole (middle panel). For comparison, we also display the gravitational quadrupole waveform of the background spacetime (bottom panel). The scalar field monopole quantifies the development of the combined scalar charge of the BH binary measured on spheres of radius $r_{\rm ex} = 100M$, i.e., enclosing the entire binary.

The total scalar charge remains approximately constant during the inspiral as the coupling is close to its critical value. Its magnitude increases about $10M$ before the merger which coincides with the formation of a joined region in which the GB invariant is negative due to the proximity of the two BHs. As the BHs merge into a single rotating remnant with a spin below the threshold for the spin-induced scalarization, the scalar charge decays as illustrated in the inset of Fig. 3.15 (top panel). Because the scalar charges anchored around each BH follow the holes' orbital motion, they generate scalar radiation. In general, one would expect the scalar dipole to dominate the signal, as is also the case for shift-symmetric sGB gravity [35, 90, 127]. In the simulations shown here, however, the scalar dipole is suppressed due to the symmetry of the system (equal mass and spin of the companions), and the $\ell = m = 2$ multipole dominates. The scalar waveform is displayed in the middle panel of Fig. 3.15 and shows the familiar chirp pattern: its amplitude and frequency increase as the scalar charges inspiral (following the inspiraling BHs in the background), and culminates in a peak as the BHs merge. The phase of the scalar field quadrupole clearly

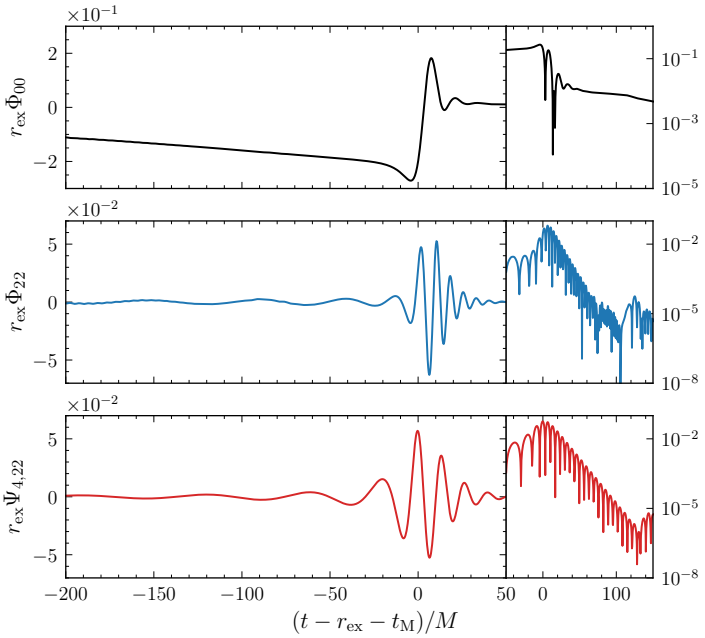

Figure 3.15: Evolution of the scalar field monopole (top panel) and quadrupole (middle panel) and gravitational quadrupole (bottom panel) for Setup B in Table 3.1. The waveforms are rescaled by the extractions radius $r_{\rm ex} = 100M$ and shifted in time such that $(t - r_{\rm ex} - t_{\rm M})/M = 0$ at the merger. In the insets we show the absolute values of the multipoles, in logarithmic scale, during the merger and ringdown.

tracks its gravitational counterpart. Therefore, we deduce that the morphology (phase evolution) of the observed scalar quadrupole radiation is a result of the orbital dynamics of the system. A sufficiently large magnitude of the coupling constant may lead to an additional scalarization of the $\ell = 2$ mode, which would become manifest as an exponential growth of the signal superposed with the chirp. This situation is analogous to the evolutions with positive coupling shown in our previous work [5].

After the merger, the scalar quadrupole exhibits a quasi-normal ringdown pattern, i.e., an exponentially damped sinusoid, shown in the inset of Fig. 3.15 (middle panel). Here, in contrast to Ref. [5], descalarization occurs due to the vanishing of negative GB regions outside the remnant BH (because its final spin is $|\chi_f| < 0.5$), rather than due to a reduction of positive curvature (because of an increase in mass). We note that the scalar field rings down on similar timescales as the GW signal shown in the bottom panel of Fig. 3.15 for comparison. Therefore, one might expect a modification to the GW ringdown if backreaction onto the spacetime is included.

3.5.6 Discussion

In this paper, we continued our study of dynamical scalarization and descalarization in binary BH mergers in sGB gravity by extending our previous work [5]. The latter focused on a positive coupling constant between the scalar field and the GB invariant, yielding dynamical descalarization in binary BH mergers. As a natural continuation, here we studied a negative coupling for which the BHs' spins play a major role

in determining the onset of scalarization. In particular, we have shown that the merger remnant can either dynamically scalarize or dynamically descalarize depending on its spin and mass.

Spin-induced dynamical scalarization occurs when the merger remnant grows a scalar charge during coalescence due to the large spin of the remnant. In cases like this, the initial binary components lack a charge because their spins are not large enough to support one [4,65–67,71,141]. However, after the objects merge, the remnant BH spins faster than either component, allowing for a charge to grow. We found that it is possible for the scalar charge to grow as early as 1–2 orbits before a CAH has formed if the coupling $|\beta|$ is extremely large. This occurs because there are spacetime regions before merger (and near the poles of the future remnant) with a negative GB invariant, and a sufficient large value of $|\beta|$ allows bound states to form fast enough. We also found that if the coupling $|\beta|$ is close to the threshold, then scalarization occurs only in the late ringdown, because of the timescale required for the bound states to form.

Is such spin-induced scalarization detectable with current or future GW observatories? For values of $|\beta|$ near the scalarization threshold the instability timescale is large and the effects of the scalar field growth would only appear at times much later than the merger and, more importantly, after the start of the ringdown. Hence, the inspiral-merger-ringdown of such a binary would be indistinguishable from one in GR, and scalarization would be a hidden or "stealth" effect, i.e., the remnant BH would acquire a charge, but its formation would not lead to an easily measurable effect. For instance, during the GW ringdown, which is dominated by the fundamental $(\ell, m) = (2, 2)$ quasinormal mode (QNM) frequency, we know that at a spin of $\chi \approx 0.68$, the decay time is approximately $\tau \approx 12.3M$ [167]. Hence, after $100M$ from the peak in the waveform, the dominant mode has decayed by roughly $\exp(-t/\tau) \approx \exp(-100/12.3) \approx 10^{-4}$. If the dominant QNM frequency begins to be modified only after $100M$, the GW has decayed so much that detecting this change or constraining it would be essentially impossible.

Is there no hope to detect such late times scalarization? Not necessarily. If we were to include the scalar field backreaction onto the spacetime, one could entertain the possibility that the late time growth of the scalar field (in particular of Φ_{22}) and the subsequent readjustment of the spinning remnant BH to its scalarized counterpart could result in a *second* GW signal. Confirming this possibility and, if confirmed, characterizing such a GW signal is left for future work.

Spin-induced dynamical descalarization occurs when the merger remnant loses its scalar charge during coalescence due to the low spin of the remnant. In cases like this, the initial binary components are spinning fast enough that each of them has a scalar charge and the remnant descalarizes if it has spin $\chi_f \leqslant 0.5$. Here we demonstrated this effect in a example in which the initial binary components have their spin angular momenta anti-aligned with the orbital angular momentum. The merger produces a remnant BH with $\chi_f = 0.48$, for which no scalar field bound states are supported and the field is radiated away shortly ($\sim 10M$) after the CAH formation.

Is such spin-induced descalarization detectable with current or future GW observatories? For such descalarization to be detectable, one must first detect that the binary components were scalarized during the inspiral. Our simulations showed that the scalar charges lead to scalar quadrupole radiation because of the highly symmetric configurations (equal mass, equal spin magnitude) we chose to evolve. More

realistic astrophysical configurations (with unequal masses and unequal spin magnitudes) forces the binary to emit scalar dipole radiation. Such emission of dipole or quadrupole radiation accelerates the inspiral, and thus affect the GW phase at -1PN and 0PN respectively, as shown in shift-symmetric theories [88–90, 125–127]. These effects in the inspiral are observable and can thus be constrained with current ground-based [43, 44, 117–119] and future detectors [168, 169] within the parameterized post-Einsteinian framework [170–173], provided the binary is of sufficiently low mass such that enough of the inspiral is observed [169]. In fact, a constraint of this type was recently obtained using the GW190814 event [174] in [116].

Let us then assume, for the sake of argument, that some future event reveals a scalar charge in the inspiraling binary components. Our results then indicate that descalarization may be detectable, if there is enough signal-to-noise ratio in the merger and ringdown [35, 92]. This is because this process occurs at the same time and with the same timescales as the GW merger and ringdown, see Fig. 3.15. Future work could study the backreaction of the scalar field onto the metric to determine the magnitude of these modifications in the transient phase, without which one cannot assess detectability confidently. Our results indicate that descalarization might be best probed with a full inspiral-merger-ringdown analysis of the GW signal.

Chapter 4

Inflation

4.1 Background

The large-scale, homogeneous universe is well-approximated by the FLRW metric

$$\mathrm{d}s^2 = -\mathrm{d}t^2 + a^2(t)\Big[\frac{\mathrm{d}r^2}{1-kr^2} + r^2\mathrm{d}\Omega^2\Big]\,, \tag{4.1}$$

where a is the scale factor and k is a parameter characterising the overall curvature. Using Einstein's equations, one obtains the Friedmann equations that govern the universe's evolution

$$H^2 = \frac{8\pi G\rho}{3} - \frac{k}{a^2}\,, \tag{4.2}$$

$$\frac{\ddot{a}}{a} = -\frac{4\pi G}{3}\Big(\rho + 3p\Big)\,, \tag{4.3}$$

for which $H \equiv \dot{a}/a$ is the Hubble parameter, ρ is the (total) energy density of matter/radiation/vacuum energy and p is the associated pressure. During the mid 20th century, it was believed that the evolution of the universe evolved according to the Friedmann equations regular matter or radiation. However, during the second-half of the 20th century, the standard Hot Big Bang model of the early universe became fraught with observational inconsistencies. Firstly, it was realised that if the expansion of the universe was dominated by matter/radiation throughout its history, then any regions of the CMB that are separated by more than 2° would be causally disconnected [175]. This is in stark contradiction to the observed homogeneity at such scales, which suggests a causally connected history. Put in a more formal framework, consider the comoving distance between times t_0 and t given by

$$d_h = \int_{t_0}^{t} \frac{\mathrm{d}t}{a(t)}\,, \tag{4.4}$$

which is equivalent to the comoving particle horizon if one sets $t_0 = 0$ as the beginning of time. The particle horizon determines whether events are in causal contact. For the standard matter/radiation dominated universe, one finds that this is approximately the comoving Hubble distance

$$d_h \sim (aH)^{-1}\,, \tag{4.5}$$

which grows under these conditions. Consequently, the comoving horizon between now and the time of photon decoupling is larger than the particle horizon at that time, and so we should observe a plethora of causally disconnected regions in the CMB. This is called the *horizon problem*.

A related problem concerns the overall curvature of the universe. The critical density of the universe ρ_{crit} is the energy density required for the universe to be flat. It is obtained by substituting $k = 0$ into (4.2) and rearranging:

$$\rho_{\text{crit}} = \frac{3H^2}{8\pi G}\,. \tag{4.6}$$

Defining the density parameter

$$\Omega = \frac{\rho}{\rho_{\text{crit}}}\,, \tag{4.7}$$

and curvature density parameter

$$\Omega_k = -\frac{k}{a^2H^2}\,, \tag{4.8}$$

one can use (4.2) to obtain the relation

$$\Omega = 1 - \frac{(aH)^{-2}}{(a_0H_0)^{-2}}\Omega_{k,0}\,, \tag{4.9}$$

where the $\Omega_{k,0}$ is the curvature density parameter today, which is bounded by observations to be $|\Omega_{k,0}| < 0.005$ [175]. This means that the universe today is very nearly flat (as Ω is close to unity) and given that the comoving Hubble radius $(aH)^{-1}$ grows with time, it was therefore extraordinarily flat at early times. This apparent fine-tuning of curvature to unity is known as the *flatness problem*.

Perhaps the most significant issue however, is that of *superhorizon correlations*. That is, there are density correlations in the CMB that exist over acausal distances. One may be justified in explaining the horizon and flatness problems purely as a consequence of symmetries in an unknown theory that dictates the initial conditions of the universe. On the other hand, it is not so feasible to relegate the mysterious origin of such correlations to "peculiar" initial conditions, and thus a more conventional explanation within current theory is required. This is the role played by inflation.

Given the crucial role played by the (growing) comoving Hubble horizon in the problems above, a possible solution to these problems would be the introduction of a decreasing comoving Hubble horizon

$$\frac{\mathrm{d}}{\mathrm{d}t}(aH)^{-1} < 0\,, \tag{4.10}$$

during some stage of the universe's history. Given the definition of the Hubble parameter, we see that (4.10) is simply a phase of accelerated expansion $\ddot{a} > 0$ i.e. inflation. If this phase of accelerated expansion lasts sufficiently long, then the particle horizon becomes much larger than the Hubble radius, and thus ostensibly disconnected regions on the CMB were in fact causally connected. To quantify the necessary requirements, we expand (4.10)

$$\frac{\mathrm{d}}{\mathrm{d}t}(aH)^{-1} = -\frac{\dot{a}H + a\dot{H}}{(aH)^2}\,, \tag{4.11}$$

$$= \frac{\epsilon_H - 1}{a}\,, \tag{4.12}$$

where

$$\epsilon_H \equiv -\frac{\dot{H}}{H^2} = -\frac{\mathrm{d}\ln H}{\mathrm{d}N}\,, \tag{4.13}$$

is the first Hubble slow-roll parameter and $\epsilon_H < 1$ is required for inflation to occur. To ensure that inflation lasts for a sufficient amount of time, we also define a second Hubble slow-roll parameter

$$\eta_H \equiv \frac{\mathrm{d}\ln\epsilon_H}{\mathrm{d}N} = \frac{\dot{\epsilon}_H}{\epsilon_H H}\,, \tag{4.14}$$

for which one requires $|\eta_H| < 1$.

Ever since the concept of inflation was suggested as a solution to fix the aforementioned issues, a variety of mechanisms to generate the necessary accelerated expansion were proposed (see [176] for a summary of the history). The simplest - and arguably most effective - is that of a scalar-field ϕ, called the inflaton, slowly rolling down its potential $V(\phi)$. Originally coined "chaotic inflation" [176], this is now commonly regarded as the standard inflationary scenario. Consider the scalar-field action

$$S = \int \mathrm{d}^4x\sqrt{-g}\Big[-\frac{1}{2}g^{\mu\nu}\partial_\mu\phi\partial_\nu\phi - V(\phi)\Big]\,, \tag{4.15}$$

from which in an FLRW background, one obtains the Klein-Gordon equation

$$\ddot{\phi} + 3H\dot{\phi} = -\frac{\mathrm{d}V}{\mathrm{d}\phi}\,. \tag{4.16}$$

In the presence of the inflaton, the Friedmann equation becomes

$$H^2 = \frac{1}{3M_{\mathrm{P1}}^2}\Big(\frac{1}{2}\dot{\phi}^2 + V\Big)\,, \tag{4.17}$$

where we have introduced the reduced Planck mass $M_{\mathrm{P1}} = (8\pi G)^{-1/2}$ and ignored the curvature term (which will flatten out regardless). Substituting (4.17) into the equations for the Hubble slow-roll parameters (4.13) and (4.14) yields

$$\epsilon_H = \frac{\frac{3}{2}\dot{\phi}^2}{\frac{1}{2}\dot{\phi}^2 + V}\,, \tag{4.18}$$

$$\eta_H = 2\Big(\epsilon_H + \frac{\ddot{\phi}}{H\dot{\phi}}\Big)\,, \tag{4.19}$$

from which we see that the conditions $\{\epsilon_H \ll 1, |\eta_H| \ll 1\}$ imply $\{\dot{\phi}^2 \ll V, |\ddot{\phi}| \ll |3H\dot{\phi}|\}$. Consequently, from the Friedmann equation (4.17) one now has

$$H^2 \approx \frac{V}{3M_{\mathrm{P1}}^2}\,, \tag{4.20}$$

meaning that we achieve exponential expansion governed by an approximately constant potential. Furthermore, using the inflaton field equation (4.16) we also obtain

$$3H\dot{\phi} \approx -\frac{\mathrm{d}V}{\mathrm{d}\phi}\,, \tag{4.21}$$

which states that the Hubble friction (LHS) roughly balances the pull from the potential gradient (RHS), maintaining a very small, approximately constant inflaton velocity. It is useful to express the slow-roll conditions as statements about the potential. For the first slow-roll condition, this is achieved by substituting the approximations (4.20) and (4.21) into the equation for ϵ_H (4.13) to give the first potential slow-roll parameter

$$\epsilon_V \equiv \frac{M_{\rm P1}^2}{2}\Big(\frac{V'}{V}\Big)^2 . \tag{4.22}$$

The second potential slow-roll parameter η_V is obtained by taking the time-derivative of (4.21)

$$\begin{aligned} 3(\dot{H}\dot{\phi} + H\ddot{\phi}) &= -\frac{\mathrm{d}^2 V}{\mathrm{d}\phi^2}\dot{\phi}\,, \\ \frac{\dot{H}}{H^2} + \frac{\ddot{\phi}}{H\dot{\phi}} &= -M_{\rm P1}^2\frac{V''}{V}\,, \\ -\epsilon_H + \frac{\ddot{\phi}}{H\dot{\phi}} &= -M_{\rm P1}^2\frac{V''}{V} \end{aligned} \tag{4.23}$$

in which we divided by $H^2\dot{\phi}$ and employed (4.20) in the second line. Hence we have

$$\eta_V \equiv M_{\rm P1}^2\frac{V''}{V}\,. \tag{4.24}$$

Thus, with an appropriate potential one can define inflation as the period in which $\{\epsilon_V \ll 1,\, |\eta_V| \ll 1\}$. Defining the total number of e-folds of accelerated expansion

$$N_{tot} \equiv \int_{a_0}^{a_f} \mathrm{d}\ln a = \int_{t_0}^{t_f} H\mathrm{d}t\,, \tag{4.25}$$

one requires $N_{tot} \geq 60$ in order to resolve the issues discussed earlier [175].
Inflation offered a (somewhat) natural and simple solution of all three aforementioned problems which riddled the standard Hot Big Bang cosmology. Moreover, quantum fluctuations of the inflaton field provides a mechanism to seed density perturbations which aggregate to form large-scale structure. Inflation predicts an almost scale-invariant spectrum of these perturbations, consistent with CMB observations. Thus, it has proven to be apt on both the conceptual and observational fronts. Unfortunately, however, inflation is not without its own problems (and criticisms). Putting the origin of the inflaton itself to the side, we summarise the major difficulties below:

1. *Eta problem* - describing the inflationary mechanism in terms of an effective field theory one finds that higher energy corrections will naturally alter the potential. Although small, they can be significant enough to cause $\eta_V > 1$, thus ending the slow-roll phase. A variety of solutions have been proposed, for example via a non-minimal coupling between the inflaton and gravity [177].

2. *Trans-Planckian problem* - if inflation lasts greater than 60 e-folds, it is possible for inflaton fluctuations of wavelengths shorter than the Planck scale to be magnified to that of large-scale structure.

This puts serious doubts on the validity of the semi-classical calculations of the power spectrum for these modes [178,179]. Even more damning, it was conjectured that such a problem can never occur in a valid string theory framework, thus imposing a significant constraint on the energy-scale of such inflationary models [180].

3. *Measure problem* - for some inflationary models, quantum fluctuations can keep the inflaton in the slow-roll region of the potential perpetually (at least in some parts of the spacetime). Known as *eternal inflation*, one is left with a multiverse of "pocket universes", each of which being governed by its own laws of physics (if string theory is accurate). Though this may solve a variety of fine-tuning problems through the anthropic principle, it renders the predictive capability of eternal inflation rather uncertain. This is because one must base predictions on relative probabilities that involve infinities, the regulation of which are determined by what measure one uses. However, this choice is plagued with ambiguity, making it unclear how useful eternal inflation is as a (presumably falsifiable) scientific theory.

4. *Initial conditions* - the primary goal of inflation was to provide a natural mechanism to generate the homogeneous, flat universe we observe today. One then presumes that the power of inflation lies in its ability to transform a generic initial state to the unique one described. However, this means that inflation should survive despite inhomogeneities in the inflaton field *itself*. Arriving at such a conclusion is not a trivial matter, given the complexity of the possible interactions of a highly inhomogeneous field with itself and the surrounding spacetime. It is entirely possible that the presence of large gradients or high velocities in the inflaton field ruins its inflationary capability.

It is this last problem - the sensitivity of inflation to initial conditions - that we will now address. In particular, we use the power of numerical relativity to investigate how the combination of an inhomogeneous initial scalar-field with a non-uniform initial velocity affects the robustness of a (small-field) inflationary model.

4.2 Research work III: the effect of non-uniform scalar-field momenta on inhomogeneous small-field inflation

In this section we present a draft version of our work on *the effect of non-uniform scalar-field momenta on inhomogeneous small-field inflation*. Collaborators include: Matthew Elley, Josu Aurrekoetxea, Eugene Lim, Katy Clough and Panagiotis Giannadakis.

4.2.1 Abstract

We study the robustness of single-field inflation against initial inhomogeneities in both the field and its momentum for a small-field α-attractor model. We find that the introduction of a relatively small

inhomogeneous momentum profile results in the failure of inflation for this model, though only in certain regions of the spacetime. Furthermore, we investigate how varying the wavelength and phase of the momentum profile affects the sensitivity to inflationary failure. We conclude that higher modes are less effective at inducing failure, and that the larger the relative phase difference between the field and its momentum profile the less likely failure will occur.

4.2.2 Introduction

The theory of cosmological inflation [181–185] is regarded as the conventional explanation of several problems which once plagued the hot Big Bang model. Briefly put, the accelerated expansion of the early universe resolves the stark contradiction between the observations of a flat, homogeneous universe with super-horizon correlations and the expected inhomogeneous, causally disconnected universe likely to arise from a steady expansion since the beginning of time. Furthermore, it even provides a natural mechanism to seed structure formation, with one of its most remarkable successes being the observation of the predicted nearly scale-invariant and Gaussian spectrum of primordial perturbations [186].

The standard mechanism driving inflation is a scalar field slowly rolling down its potential. For this to occur, two conditions must be satisfied. Firstly, the potential must possess a region which obey certain slow-roll criteria. This is dependent on what one uses as an overarching physical theory of the early universe, usually a low-energy limit of a quantum theory of gravity. The validity of theories containing such a potential is a source of contention, however we will simply assume certain models without addressing these issues. Secondly, there must exist trajectories in phase space which lead to a slow-rolling scalar field - that is, dominated by an approximately constant (positive) potential energy. Moreover, one expects the initial configuration that leads to these trajectories to be quite general i.e. not fine-tuned to generate inflation. This second condition is the subject of our investigation.

A major factor in determining the initial state of inflation is the associated energy scale. One can split this into two regimes: high-scale inflation, in which the energy density of the scalar field potential $V(\phi) \sim M_{\rm Pl}^4$ and low-scale inflation, where $V(\phi) \ll M_{\rm Pl}^4$. Examples of the former include power-law models, such as the classic quadratic potential $V(\phi) = m^2\phi^2$, whereas both hilltop and plateau models are members of the low-scale family. For the high-scale case, one can readily see how inflation can naturally occur [185, 187–189]. The universe would consist of a plethora of Planck-sized causally disconnected regions. Within these regions, all components of energy - such as the potential, gradient and kinetic - would roughly be of the same (Planck) scale. Thus, in some of these regions one would expect the inflaton take values within the slow-roll regime of the potential, and that the potential will quickly begin to dominate as the other components dilute away with expansion. Recent simulations of high-scale inflation models have confirmed their robustness to these inhomogeneous initial conditions [190–193], though one should note that they are currently disfavoured over low-scale scale inflation from CMB observations [194, 195].

On the other hand, the robustness of the favoured low-scale scale inflationary models to inhomogeneous initial conditions is less clear-cut. As the characteristic inflationary scale is smaller, the size of the causally

disconnected patches is larger, and the potential energy will likely be magnitudes smaller than other components. Consequently, it is possible that large inhomogeneities could spoil inflation before it even begins. This has motivated a wealth of studies on the effects of initial conditions on low-scale inflation, many of which involve simulating the inflating spacetime with numerical relativity in full 3+1D [190–193, 196, 197]. A significant conclusion from these investigations is that it is the distance $\delta\phi$ that the inflaton must travel in field space in order to generate the requisite number of e-folds which determines its sensitivity to inhomogeneous initial conditions. In particular, small-field inflation is defined as $\delta\phi < M_{\rm Pl}$. The slow-roll region is so limited in these models that even minimal excursions of the field can end up in the potential minimum. Moreover, the highly concave nature of the potential can prevent such excursions from being pulled back up the potential by gradient pressure. The field stuck in the minimum can then pull the rest down, quickly ending inflation. On the other hand, large-field inflationary models - for which $\delta\phi \sim M_{\rm Pl}$ - have potentials that are significantly less concave and possess a long (Planck-sized) slow-roll region. They are therefore resistant to the aforementioned effects which spoil inflation in small-field models [190, 192].

Here we extend the work of [190–192] in investigating the effect of inhomogeneous initial conditions to the case of a non-uniform initial inflaton momentum. We consider a small-field member of the (plateau-type) α-attractor family [198,199]. For our simulations we use GRChombo, a multipurpose numerical relativity code [200]. We briefly summarise our results below:

- The introduction of uniform/inhomogeneous initial momentum profiles generally reduces the robustness of our inflationary model (i.e causes some regions to fall into the potential minimum)
- Smaller wavelength fluctuations in the initial momentum profiles are less effective in ending inflation (require greater energies)
- The closer the maxima of the momentum profile is to the maxima of the initial field profile, the more likely inflation will end (but not everywhere)
- For non-uniform initial momentum, inflation ends in some regions but appears to continue (high up the plateau) in others, separated by a sharp field gradient. Thus it is possible inflation survives in these "bubbles", though more work is required to verify this statement

4.2.3 Theory and Methodology

Model

Considering single-field inflation with scalar-field Lagrangian

$$\mathcal{L}_\phi = -\frac{1}{2} g^{\mu\nu}\partial_\mu\phi\partial_\nu\phi - V(\phi)\,, \tag{4.26}$$

inflation is achieved in a homogeneous spacetime when the slow-roll parameters satisfy

$$\epsilon = \frac{M_{\rm Pl}^2}{16\pi}\left(\frac{V'}{V}\right)^2 \ll 1,\ \eta = \frac{M_{\rm Pl}^2}{8\pi}\left(\frac{V''}{V}\right) \ll 1\,, \tag{4.27}$$

where $M_{\rm Pl}^2 = \hbar c/G$. We use the α-attractor potential given by

$$V(\phi) = \Lambda^4 \left(1 - e^{\phi/\mu}\right)^2 , \tag{4.28}$$

in which case the potential approaches the plateau exponentially, governed by the parameter μ (see Fig. 2.2). Thus it is μ that determines if a model is large or small field, whereas Λ determines the energy-scale.

One should note that the property of being either a large or small field model is tied with the associated scale of inflation via the scalar power spectrum

$$\Delta_R^2 = \frac{H^2}{\pi M_{\rm Pl}^2 \epsilon} \approx 2 \times 10^{-9} , \tag{4.29}$$

where H is the Hubble constant and ϵ is the first slow-roll parameter given in (4.27). Since $H^2 \propto V$, a lower energy of inflation requires a smaller ϵ in order to be consistent with the observed value of the scalar power spectrum. Consequently, the field velocity is slower and so the inflaton must travel a shorter distance in field space in order to generate the expected number of e-folds $\mathcal{N}$, which can be approximated by

$$\delta\phi \approx \frac{\mathcal{N}}{2} \frac{H}{M_{\rm Pl}} 10^5 M_{\rm P1} , \tag{4.30}$$

assuming a constant H and ϵ. Hence viable small-field models have a characteristic energy lower than that of their large-field counterparts.

To understand the evolution of an inhomogeneous inflaton field, consider the scalar-field evolution equation - from the Lagrangian (4.26) - on an FLRW background

$$\ddot{\phi} = \nabla^2 \phi - 3H\dot{\phi} - \frac{dV(\phi)}{d\phi} , \tag{4.31}$$

each term on the RHS representing a mechanism that govern the dynamics of an inhomogeneous scalar-field:

1. Scalar-field gradient pressure - spatial inhomogeneities in the field result in gradients which act to homogenize the it, dilutes with expansion

2. Hubble friction - expansion of spacetime decreases the velocity of the field

3. Potential gradient - accelerates the field to its minimum, ending inflation

The form and magnitude of the initial scalar-field momentum will influence which of the above mechanisms dominate the evolution throughout the spacetime, and ultimately its inflationary fate.

Set-up

We investigate the effects of inhomogeneities in the scalar-field initial data by superposing sinusoidal perturbations of the scalar-field and its momentum in the three spatial directions:

$$\phi_{init}(\mathbf{x}) = \phi_0 + \frac{\Delta\phi}{3}\sum_{i=1}^{3}\cos\left(k_\phi x_i\right), \tag{4.32}$$

$$\Pi_{init}(\mathbf{x}) = \Pi_0 + \frac{\Delta\Pi}{3}\sum_{i=1}^{3}\cos\left(k_\Pi x_i + \theta\right). \tag{4.33}$$

Here ϕ_0 (Π_0) is the initial background value for the scalar field (momentum) and $\Delta\phi$ ($\Delta\Pi$) is the amplitude of the scalar field (momentum) perturbation. Additionally, we include a phase θ in the Π perturbation. The size of the perturbations are determined by wavenumber $k_\phi = 2\pi N_\phi/L$, where N is a natural number and L is set as the initial Hubble length H_0^{-1} in the absence of inhomogeneities

$$L = \frac{3M_{\rm Pl}}{\sqrt{24\pi V\left(\phi_0\right)}}. \tag{4.34}$$

We use subscripts on k and subsequently N to identify if the quantity refers to the ϕ or Π perturbation. For all our simulations we set $N_\phi = 1$.

One should note that we do not superpose a series of modes. This is such that the given (gradient/kinetic) energy density is focused in the amplitude of the singular mode rather than shared amongst many modes. This is in accordance with the findings of [190,191,196] which demonstrated the importance of inflationary success on the local dynamics of the scalar field, this being dependent on the amplitude of the perturbations. We set our computational domain to be a cube of length $L_{com} = 32M$, with a grid size of 128^3. Here M is the geometrized mass unit, which is a fraction of the Planck mass M_{Pl} as determined by setting L_{com} equal to the Hubble length L given by (4.34). Periodic boundary conditions are enforced.

We consider a small-field α-attractor model given by the potential (4.28) with parameters $\mu = 0.005M_{\rm Pl}$ and $\Lambda^4 = 1.18\times10^{-18}M_{\rm Pl}^4$. Setting $\phi_0 = -6.33\times10^{-2}$, this would yield 100 e-folds for the standard case of homogeneous inflation and generate the observed scalar power given by (4.30). We fix the perturbation of the scalar-field for all runs, setting $\Delta\phi = 4.50\times10^{-2}$ so that in the absence of Π_{init} the scalar-field homogenises into a slow-roll inflating state i.e. it does not fall into the potential minimum for at least the first several e-folds (see the first plot of Fig. 4.2).

Initial data

In the Arnowitt-Deser-Misner (ADM) formulation, one foliates spacetime into a stack of spatial hypersurfaces such that the metric can be written as

$$ds^2 = -\left(\alpha^2 - \beta^i\beta_i\right)dt^2 + 2\beta_i dx^i dt + \gamma_{ij}dx^i dx^j, \tag{4.35}$$

where γ_{ij} is the spatial metric on the hypersurfaces, α is the lapse function and β^i is the shift vector. These quantities must be specified on the initial hypersurface, along with the extrinsic curvature which is

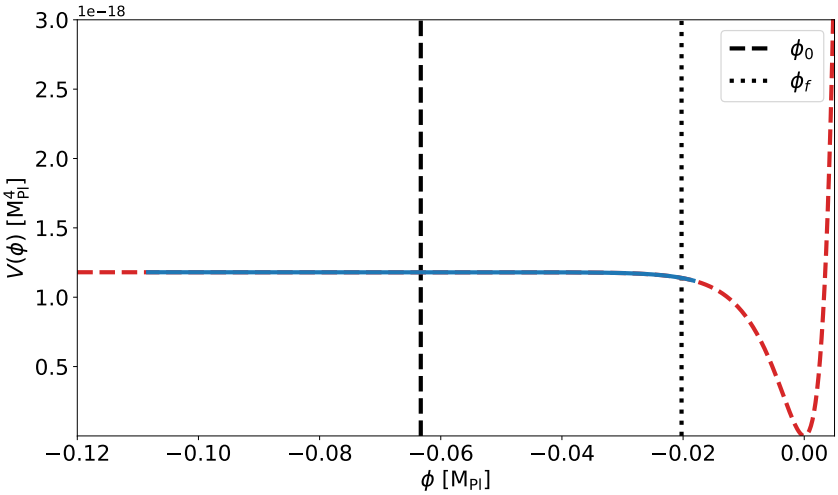

Figure 4.1: Our small-field α-attractor potential with $\mu = 0.005 M_{\rm Pl}$ and $\Lambda^4 = 1.18 \times 10^{-18} M_{\rm Pl}^4$. The solid blue line represents the region of the potential initially spanned by the scalar-field. The vertical dashed line is the background scalar-field value ($\phi_0 = -6.33 \times 10^{-2} M_{\rm Pl}$) and the vertical dotted line shows where the slow-roll parameter $\epsilon = 1$ ($\phi_f = -2.03 \times 10^{-2} M_{\rm Pl}$).

the Lie derivative of the spatial metric along the vector normal to the hypersurfaces

$$K_{ij} = -\frac{1}{2}\mathcal{L}_{\mathbf{n}}\gamma_{ij}\,. \tag{4.36}$$

For the gauge functions, we simply choose $\alpha = 1$ and $\beta_i = 0$. On the other hand, γ_{ij} and K_{ij} must satisfy the Hamiltonian and momentum constraint equations

$$\mathcal{H} \equiv {}^{(3)}R + K^2 - K_{ij}K^{ij} - 16\pi\rho = 0\,, \tag{4.37}$$

$$\mathcal{M}^i \equiv D_j\left(K^{ij} - \gamma^{ij}K\right) - 8\pi S^i = 0\,, \tag{4.38}$$

where ${}^{(3)}R$ is the spatial Ricci scalar, K is the trace of the extrinsic curvature and D_j is the spatial covariant derivative. The energy and momentum densities are obtained from the stress-energy tensor $T^{\mu\nu}$ via normal and spatial projections:

$$\rho = n_\mu n_\nu T^{\mu\nu}\,, \tag{4.39}$$

$$S^i = -n^\mu\left(\gamma^{\nu i} + n^\nu n^i\right)T_{\mu\nu}\,. \tag{4.40}$$

Following the Conformal Transverse Traceless (CTT) method for solving the initial data problem, we perform a conformal re-scaling of the spatial metric and decompose the extrinsic curvature such that

$$\gamma_{ij} = \psi^4\bar{\gamma}_{ij}\,, \tag{4.41}$$

$$K_{ij} = \psi^{-2}\bar{A}_{ij} + \frac{1}{3}\gamma_{ij}K\,, \tag{4.42}$$

in which ψ is the conformal factor, $\bar{\gamma}_{ij}$ is the conformal spatial metric and $\bar{A}_{ij}$ is the conformal traceless extrinsic curvature. Assuming conformal flatness ($\bar{\gamma}_{ij} = \delta_{ij}$) one can then write the Hamiltonian (4.37) and momentum (4.38) constraints as

$$8\bar{D}^2\psi - \psi\bar{R} - \frac{2}{3}\psi^5 K^2 + \psi^{-7}\bar{A}_{ij}\bar{A}^{ij} = -16\pi\psi^5\rho\,, \tag{4.43}$$

$$\left(\bar{\Delta}_{\mathrm{L}}W\right)^i - \frac{2}{3}\psi^6\bar{\gamma}^{ij}\bar{D}_j K = 8\pi\psi^{10}S^i\,, \tag{4.44}$$

$$\bar{D}_j\bar{A}^{ij}_{\mathrm{TT}} = 0\,, \tag{4.45}$$

where $\bar{\Delta}_{\mathrm{L}}$ is the conformal vector Laplacian, $\bar{R}$ is the conformal Ricci scalar, $\bar{D}$ is the conformal covariant derivative and $\bar{A}_{ij}$ has been split into its transverse ($\bar{A}^{ij}_{TT}$) and longitudinal (given by vector potential W^i) components

$$\bar{A}^{ij} = \bar{A}^{ij}_{\mathrm{TT}} + \bar{D}^i W^j + \bar{D}^j W^i - \frac{2}{3}\bar{\gamma}^{ij}\bar{D}_k W^k\,. \tag{4.46}$$

In the CTT method, one specifies $\bar{\gamma}_{ij}$ and K as free data - which decouples the momentum constraint from the Hamiltonian constraint - and then solves the constraints for ψ and W^i. However, as we are simulating an inflationary spacetime we invoke periodic boundary conditions - one can think of the simulation domain as one of many identical cells filling the universe. This BC, along with the ψ-dependent form of the energy density for a scalar field

$$\rho = \frac{1}{2}\psi^{-4}\left(\partial_i\phi\right)^2 + \frac{1}{2}\Pi^2 + V(\phi)\,, \tag{4.47}$$

can render the possibility of converging on a unique solution for ψ extremely difficult. Instead we employ the CTTK method, as introduced in [201]. Here one specifies an initial profile for ψ and solves (4.43) algebraically for K. For an FLRW spacetime with scale factor a we have $\psi = a^2$, and so we can set $\psi = 1$. One must also solve the momentum constraints (4.44) sourced by gradients in K and the scalar field momentum density

$$S_i = -\Pi\partial_i\phi\,. \tag{4.48}$$

For a detailed look at the CTTK method, see [201].

Evolution

We evolve the spacetime using the BSSN [9, 10, 202] formulation of Einstein's equations. Under this formalism we conformally re-scale the spatial metric using the (evolved) conformal factor χ

$$\gamma_{ij} = \frac{1}{\chi}\tilde{\gamma}_{ij}\,, \tag{4.49}$$

with

$$\chi = \left(\det\gamma_{ij}\right)^{-\frac{1}{3}}\,, \tag{4.50}$$

such that the determinant of the conformal spatial metric is unity. Consequently, in an FLRW spacetime with scale factor a one has

$$\chi = a^{-2}\,. \tag{4.51}$$

For our inhomogeneous spacetime we can define an average number of efolds as

$$\langle \mathcal{N} \rangle = -\frac{1}{2} \ln\langle \chi \rangle \,, \tag{4.52}$$

where we have used physical volume averaging

$$\langle \kappa \rangle = \frac{1}{\mathcal{V}} \int \kappa \mathrm{d}\mathcal{V} \,, \tag{4.53}$$

over the entire physical volume $\mathcal{V}$ for an arbitrary spacetime function κ (here $\kappa = \chi$).
To evolve the lapse and shift, we use a modified form of the moving puncture gauge [72, 73]

$$\partial_t \alpha = -\mu\alpha(K - \langle K \rangle) + \beta^i \partial_i \alpha \,, \tag{4.54}$$

$$\partial_t \beta^i = B^i \,, \tag{4.55}$$

$$\partial_t B^i = \frac{3}{4} \partial_t \Gamma^i - \eta B^i \,, \tag{4.56}$$

with $\mu = \eta = 1.0$. The modification $K \to K - \langle K \rangle$ is a useful adaptation given that K measures the local expansion rate. Thus, if the standard moving puncture gauge is employed one finds that the lapse grows rapidly in areas of expansion (i.e. negative K) ruining the time resolution and developing significant gradients. Allowing the lapse to grow (or shrink) as a result of the local difference from the average expansion rate resolves this issue, as long as the variations in K are not too large. However, this change is not without its disadvantages. A major issue results from the fact that the lapse now continually shrinks in regions that are expanding at a lower rate than the average. Moreover, collapsing regions will essentially become frozen, even if they do not form BHs. To remedy this problem, we set a minimum value for the lapse $\alpha_{min} = 0.4$. One may be concerned that this will allow the spacetime to evolve too close to the punctures (no "collapse of the lapse"), causing significant error growth and likely crash the simulation. We did not find this to be the case - collapsing regions would simply diminish below the grid resolution as a result of the expanding neighbourhood.
Using (4.26), one obtains the evolution equation for the scalar-field

$$-\nabla_\mu \nabla^\mu \phi + \frac{dV(\phi)}{d\phi} = 0 \,, \tag{4.57}$$

which decomposes into 3+1 form to yield

$$\partial_t \phi = \alpha\Pi + \beta^i \partial_i \phi \,, \tag{4.58}$$

$$\partial_t \Pi = \beta^i \partial_i \Pi + \alpha \partial_i \partial^i \phi + \partial_i \phi \partial^i \alpha + \alpha \left(K\Pi - \gamma^{ij} \Gamma^k_{ij} \partial_k \phi - \frac{dV}{d\phi} \right) . \tag{4.59}$$

4.2.4 Results I

Uniform initial scalar-field momentum

We first investigate how the scalar-field dynamics - and subsequently inflationary growth - is affected by a spatially constant initial scalar-field momentum $\Pi_{\text{init}} = \Pi_0$ (towards the potential minimum). In

particular, we see how the scalar-field evolves with $\langle N \rangle$ for increasing $\Pi_{\rm init}$. These runs are characterised by the ratio of their average kinetic and potential energies

$$r_{kin} = \langle \rho_{kin} \rangle / \langle \rho_{pot} \rangle \,, \tag{4.60}$$

at $t = 0$. In Fig. 4.2, we illustrate the evolution of the scalar-field at the corner (red line) and centre (blue line) of our numerical domain. These correspond to the global minimum and maximum of the field initially (and remain so throughout the evolution, though they may swap with each other).

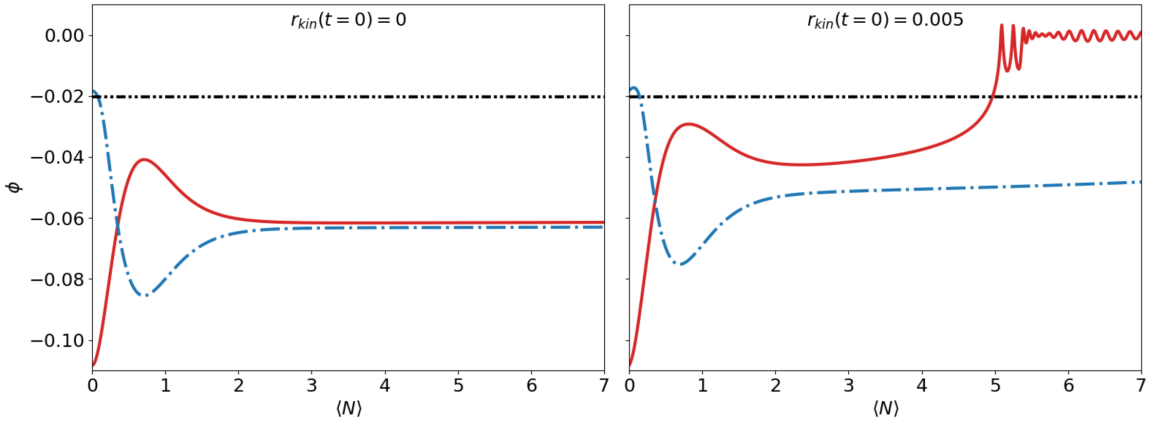

Figure 4.2: The evolution of the scalar-field with average number of e-folds at the corner (red) and centre (blue) of our numerical domain, corresponding to the initial minimum and maximum values respectively. The black dash-dotted line shows ϕ_f i.e. the value of the field for which the slow-roll parameter of the potential $\epsilon = 1$. The first and second plots show runs with constant initial scalar-field momentum $\Pi_{\rm init} = \Pi_0$ such that the initial kinetic-to-potential energy ratio $r_{kin}(t = 0) = 0$ and 0.005 respectively.

The left plot shows the trivial $r_{kin}(t = 0) = 0$ case. Here we see the field homogenise to $\sim \phi_0$ as a result of gradient pressure, as discussed in previous work [190, 192, 196]. Crucially, the minimum of the field gets pulled up the potential, away from the slow-roll violating ($\epsilon > 1$) regions of the potential (the boundary being the black dashed line). In the right plot - with $r_{kin}(t = 0) = 0.005$ - we see that very little kinetic energy is necessary to send part of the field into the potential minimum. Perhaps surprisingly, its the initial minimum of the field that ends up at the bottom of the potential. The reason for this is two-fold. Firstly, the initial gradient pressure at the maximum is far too strong to be undermined by the initial boost. Consider the ratio of the average gradient and potential energies

$$r_{grad} = \langle \rho_{grad} \rangle / \langle \rho_{pot} \rangle \,, \tag{4.61}$$

which for our $\Delta\phi$ is initially $r_{grad}(t = 0) \approx 0.06 \gg r_{kin}(t = 0)$ for all runs considered. Thus it is not surprising that initially the spatial gradients dominate the dynamics

Secondly, the minimum is disadvantaged by the boost and the gradient pressure, both of which are directed towards the bottom of the potential. One may observe that this is still not enough to directly send the field into the potential minimum. Rather, the field is pulled back up the minimum at $\langle N \rangle = 1$, and then rolls back down in a few e-folds. Subsequently, the field oscillates about the potential minimum.

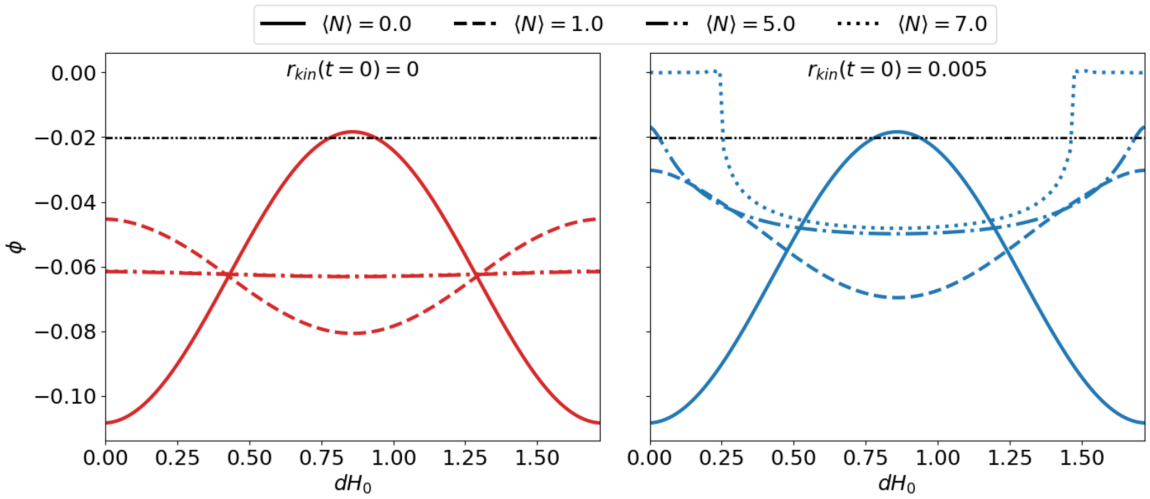

Figure 4.3: Profiles of the scalar-field across the largest diagonal of our numerical domain (corner to far-corner) for several e-folds. The first and second plots show runs with initial kinetic-to-potential energy ratio $r_{kin}(t=0) = 0$ and 0.005 respectively. Here dH_0 is the fraction of the co-moving distance to the initial Hubble scale.

In Fig. 4.3, we further illustrate the evolution of the scalar-field profile across the main diagonal of our grid for all three runs. Here one can see the gradient pressure in effect, with the first plot showing the initial perturbed profile rapidly flattening out. In the second plot, one observes the "wings" of the profile being drawn past the $\epsilon = 1$ boundary and into the potential minimum. As we have a cubic grid, we therefore see eight non-inflating corner regions surrounding an inflating centre. Once part of the field has fallen into the potential minimum, one can see from the right plot that the subsequent development of significant gradients begins to pull-down the rest of the field. Unfortunately, as the gradients are so sharp we could not resolve them fully (many levels of AMR would be required). The lack of resolution results in constraint violation in these regions, which spreads out to the rest of our domain. Thus, we only evolve a couple of e-folds after they develop, and check the convergence of the minimum and maximum of the field (see Appendix D for details of the constraint evolution and convergence). One is then left to speculate about the fate of the field (and the spacetime) as a whole in the second case. It is clear that one will expect less than 100 e-folds of inflation given that the (late-time) minimum of the field has already fallen below ϕ_0 in only a few e-folds(comparing the blue dashed-dotted lines of Fig. 4.2). Furthermore, the drag-down effect due to the gradient pressure of the field in the potential minimum will remain substantial until several more e-folds dilute it significantly. Therefore we predict that the maximum number of e-folds in this case - corresponding to the central region of the domain - will still be $\ll 100$ and thus designate as a "failure".

Inhomogeneous initial scalar-field momentum

We will now consider cases for which the scalar-field momentum has a non-trivial initial profile given by (4.33). Setting the background value $\Pi_0 = 0$, we vary $\Delta\Pi$, N_Π and θ. As a consequence of our periodic boundary conditions, certain integrability conditions are placed on the initial data such that for $N_\Pi = N_\phi$

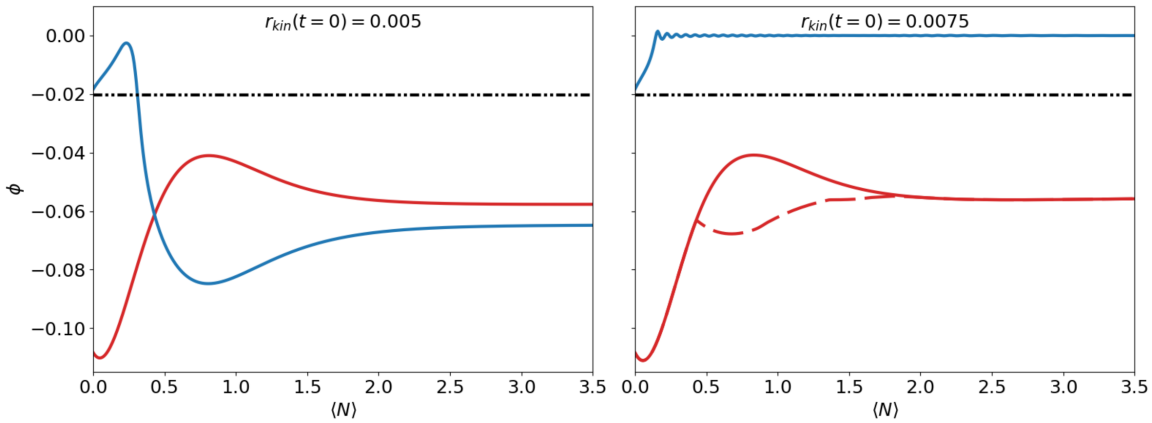

Figure 4.4: The evolution of the scalar-field with average number of e-folds at the corner (solid red) and centre (blue) of our numerical domain, corresponding to the initial minimum and maximum values respectively. The dashed red line in the second plot shows the global minimum value, which becomes distinct from the corner value at roughly 0.5 e-folds. The left and right plots show runs with initial kinetic-to-potential energy ratio $r_{kin}(t=0) = 0.005$ and 0.0075 respectively.

we can only set $\theta = 0$ or π [201].

$N_\Pi = 1$, $\theta = 0$

Here we consider the case of the initial ϕ and Π profiles being in-phase. As illustrated in Fig 4.4, it's now the initial maximum of the field that falls into the potential minimum. Despite this, one observes that for at least $r_{kin}(t=0) \leq 0.005$ the field does not fail in this region, as it is quickly pulled back up the potential by the gradient pressure (left plot). One may be surprised that the maximum even falls into the bottom of the potential, given that this does not occur for the same energy in the $\Pi_{\text{init}} = \Pi_0$ case. However, we must bear in mind that it is the average kinetic energy being considered, and so it is concentrated at the maximum (the momentum will be greater there than Π_0 of the constant case for the same energy). On the other hand, it is also this concentration of the kinetic energy that prevents failure - the neighbouring regions will have lower initial momenta, causing the field to stretch at the maximum, leading to a pinching effect that will subsequently sling-shot the field back up the potential. This is illustrated in the first plot of Fig. 4.5 showing the evolution of the (diagonal) field profiles.

The second plot of Fig 4.4 demonstrates that this pinching effect is nullified for a higher $r_{kin}(t=0)$, with the field in the central region remaining in the potential minimum. One can see from the right plot of Fig. 4.5 that this is due to a critical amount of the neighbouring field being boosted into the potential minimum. Consequently, not enough of the field gets pulled back before the gradient pressure is diluted by the expansion and the potential gradient begins to dominate. On the other hand, from the red lines of Fig 4.4 we see that trajectory of the corner field (the initial minimum) remains essentially unchanged by the energy increase. Until $\langle N \rangle = 0.5$ it seems that the field here will also fall into the potential minimum. However, this is prevented by the field in the region between the corner and centre for which $\Pi_{\text{init}} \approx 0$

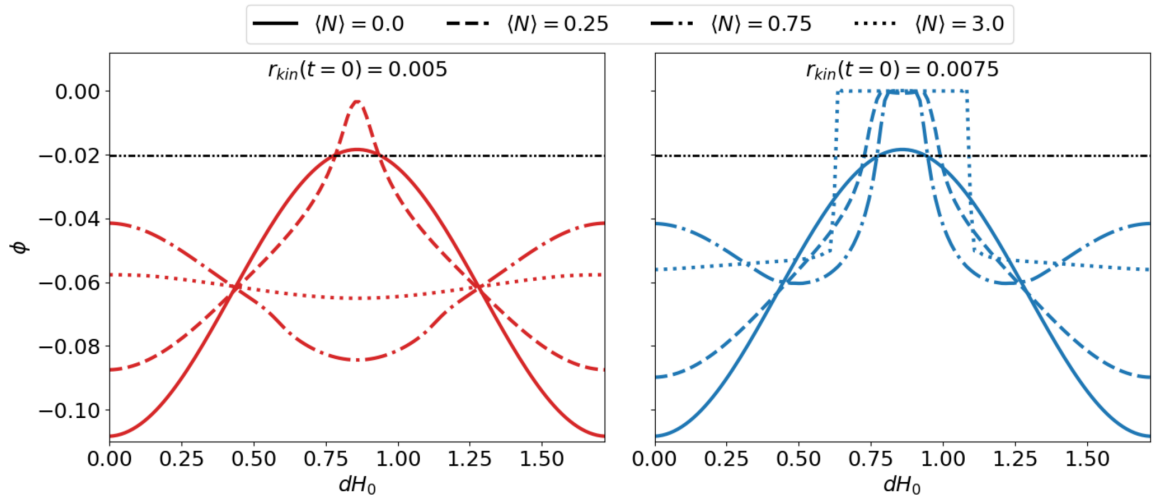

Figure 4.5: Profiles of the scalar-field across the largest diagonal of our numerical domain (corner to far-corner) for several e-folds. The left and right plots show runs with initial kinetic-to-potential energy ratio $r_{kin}(t=0) = 0.005$ and 0.0075 respectively.

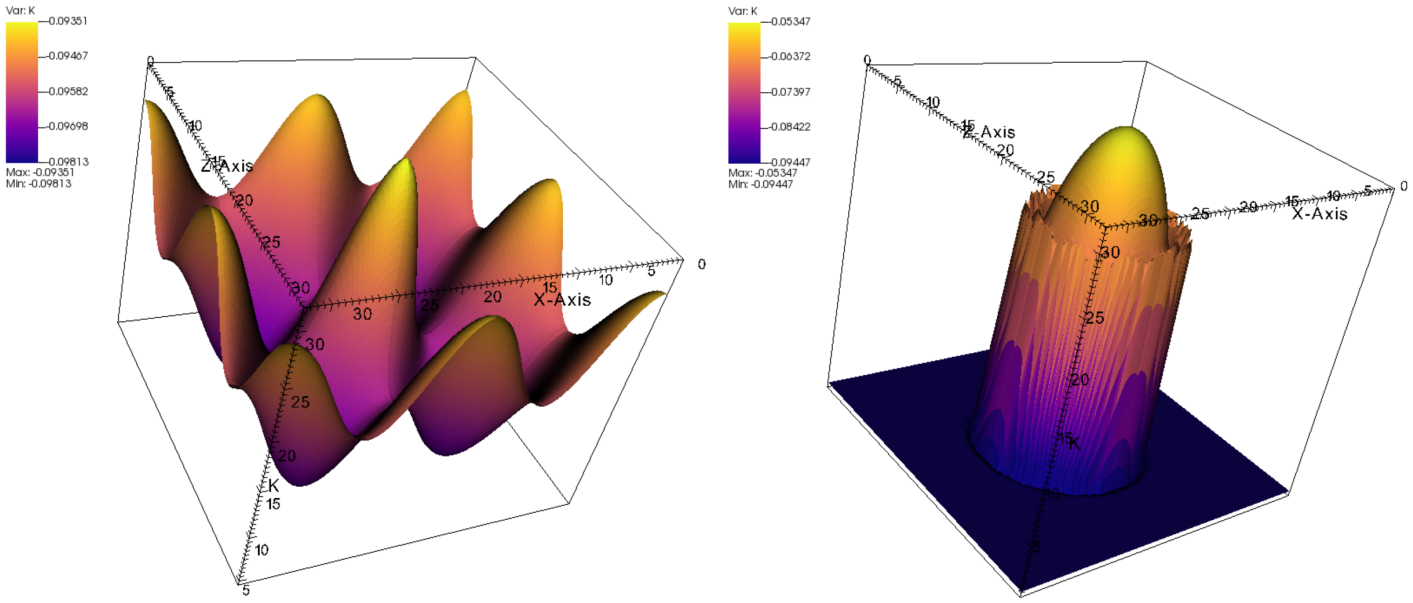

Figure 4.6: The variation of the mean curvature K on the $y = 0.5H_0$ slice at $\langle N \rangle = 0$ (left) and $\langle N \rangle = 1.5$ (right) for the case with initial kinetic-to-potential energy ratio $r_{kin}(t=0) = 0.0075$. Yellow and magenta regions indicate (negative) mean curvatures of low and high magnitudes, respectively. The 3D depth of the images are included to help visualise the relative magnitudes of the expansion.

(around $dH_0 = 0.5$ and 1.25 in Fig. 4.5). The field in this region becomes the global maximum (as indicated by the dashed red line of Fig 4.4) and pulls the neighbouring field back up the plateau.

We are therefore left with a domain that consists of a non-inflating central bubble surrounded by an inflating spacetime for which the scalar-field is high up the plateau (though slightly lower than ϕ_0). These two regions are separated by a sharp field gradient that is very difficult to resolve. This is seen in 4.6,

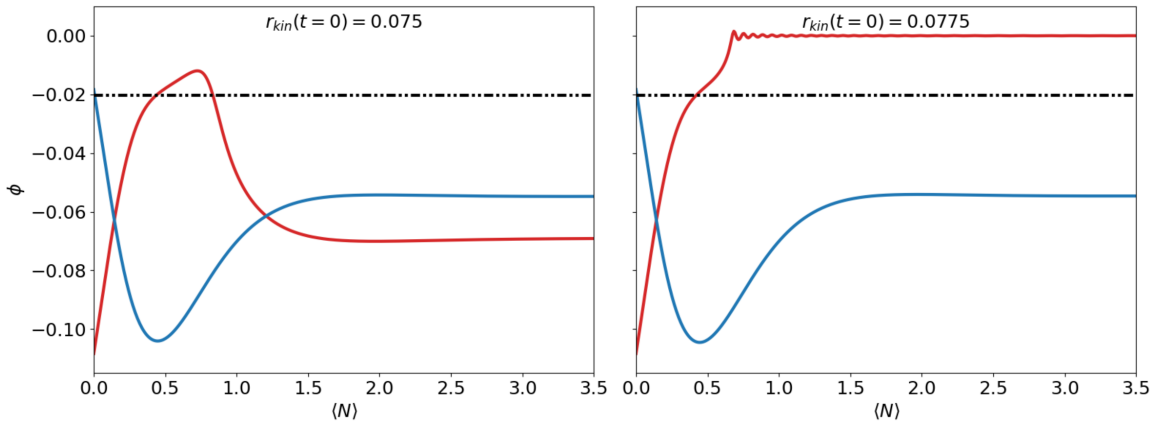

Figure 4.7: The evolution of the scalar-field with average number of e-folds at the corner (solid red) and centre (blue) of our numerical domain, corresponding to the initial minimum and maximum values respectively. Here $N_\Pi = 1$ and $\theta = \pi$ so that Π_{init} is in anti-phase with ϕ_{init}. The left and right plots show runs with initial kinetic-to-potential energy ratio $r_{kin}(t=0) = 0.075$ and 0.0775 respectively.

which illustrates the variation of the mean curvature K on the $y = 0.5H_0$ (central) slice at $\langle N \rangle = 0$ and 1.5. We observe the undulating initial K profile on the left, a consequence of CCTK (though the variations are minimal given the low energy densities involved). The right image shows our late-time non-inflating (less-negative K) bubble surrounded by inflating space. Under the assumption that they are essentially "separate universes", one can conclude that inflation survives, though the maximum number of e-folds will likely be somewhat less than 100.

$N_\Pi = 1$, $\theta = \pi$

For the case in which Π_{init} is in anti-phase with ϕ_{init}, significantly higher kinetic energy is necessary to induce failure in a region of the spacetime. We see in the evolution plots Fig. 4.7 that one requires $r_{kin}(t=0) > 0.075$, now higher than the initial gradient energy $r_{grad}(t=0) \approx 0.06$. In the left plot, the trajectory of the initial minimum (red line) - which was the cause of failure for the constant momentum case - is deflected away from the potential minimum by gradients arising from neighbouring regions with opposite field momenta. Curiously, for $\langle N \rangle \leq 0.5$ the trajectories shown in Fig. 4.7 and profiles illustrated in Fig. 4.8 almost remain the same as $r_{kin}(t=0)$ is increased. This suggests that we have identified the borderline case before failure occurs. One can see that the resulting spacetime for the $r_{kin}(t=0) = 0.0775$ scenario is the direct opposite of the in-phase $r_{kin}(t=0) = 0.0075$ case addressed previously: we now have an inflating central bubble surrounded by non-inflating spacetime. Thus the 'survival' of ≈ 100 e-folds of inflation is possible in this central region, given they are sufficiently disconnected (which is to be expected given the exponential expansion of the intervening spacetime).

$N_\Pi = 2$, $\theta = (0, \pi/2, \pi)$

For our final three cases we set $N_\Pi = 2$ and vary the phase. We illustrate the initial field and momentum

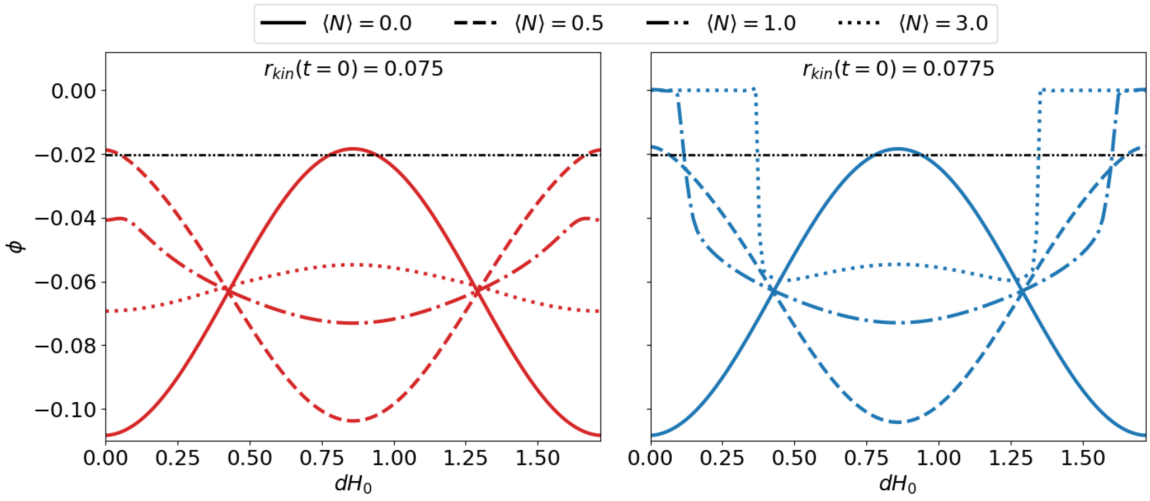

Figure 4.8: Profiles of the scalar-field across the largest diagonal of our numerical domain (corner to far-corner) for several e-folds. We have set $N_\Pi = 1$ and $\theta = \pi$ so that $\Pi_{\rm init}$ is in anti-phase with $\phi_{\rm init}$. The left and right plots show runs with initial kinetic-to-potential energy ratio $r_{kin}(t = 0) = 0.075$ and 0.0775 respectively.

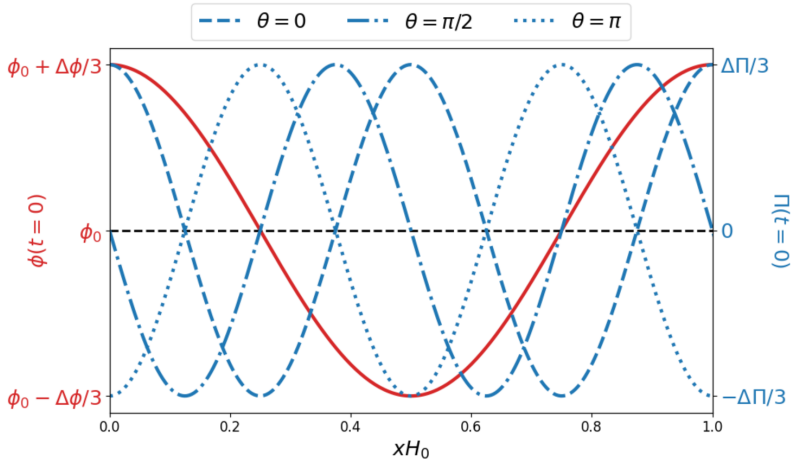

Figure 4.9: Initial profiles of the scalar-field (red) and its momentum (blue) along the x-axis for the cases with $N_\Pi = 2$ and varying phase θ.

profiles in Fig. 4.9 for visual assistance of the initial set-up. For each case, we increased the initial kinetic energy until failure (in some region) is induced. All three evolution plots for the initial minima/maxima are shown in Fig. 4.10, and the corresponding profile evolutions are illustrated in Fig. 4.11.

For the $\theta = 0$ case, we observe similar results as for the $N_\Pi = 1$, $\theta = 0$ study - the initial maximum falls to the bottom of the potential, but the initial minimum is pulled away from a failure trajectory by the surrounding field. However, slightly more kinetic energy is required (about an order of magnitude) and we observe that the size of the non-inflating bubble at $\langle N \rangle = 3$ is larger (dotted red line in the left plot of Fig. 4.11). This is because one must also boost the field around the maximum sufficiently (as the velocity fluctuation falls off much faster for shorter wavelengths) such that a larger region falls into the potential minimum rather than pull the field-maximum back up.

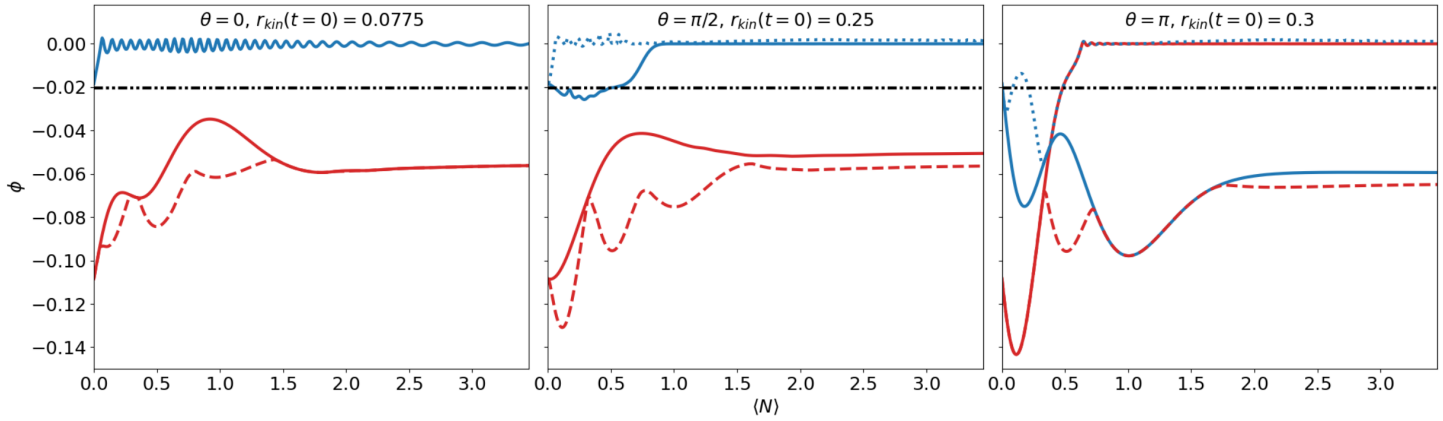

Figure 4.10: The evolution of the scalar-field with average number of e-folds at the corner (solid red) and centre (solid blue) of our numerical domain, corresponding to the initial minimum and maximum values respectively. The dashed red and dotted blue lines show the global minimum and maximum field values, if these differ from their initial positions. The left, centre and right plots are for the cases with initial phase $\theta = 0, \pi/2, \pi$ and initial kinetic energies $r_{kin}(t = 0) = 0.0775, 0.25, 0.3$ which result in failure at some location in the domain.

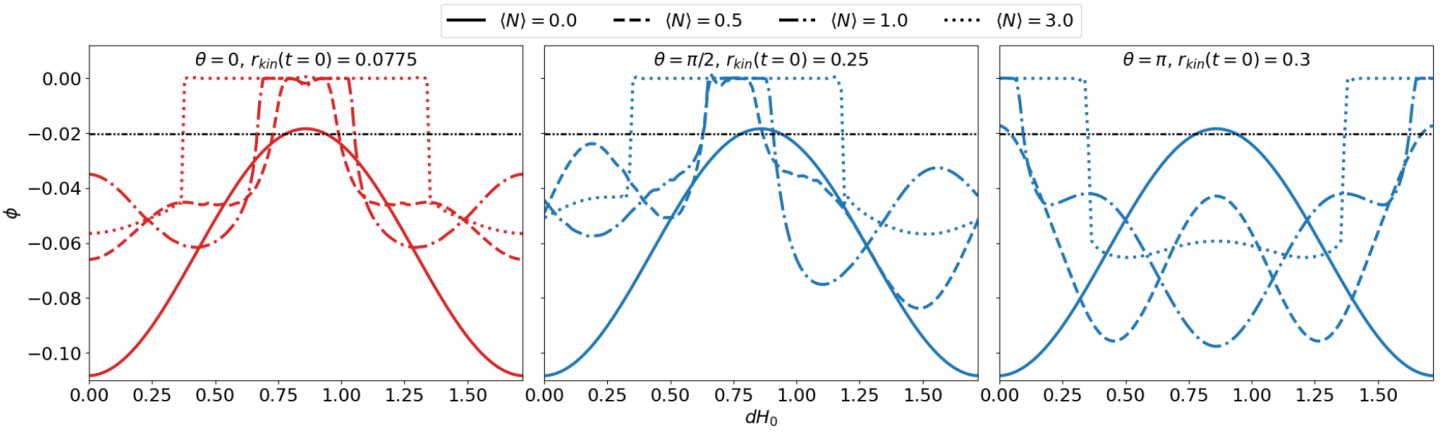

Figure 4.11: Profiles of the scalar-field across the largest diagonal of our numerical domain (corner to far-corner) for several e-folds. The left, centre and right plots are for the cases with initial phase $\theta = 0, \pi/2, \pi$ and initial kinetic energies $r_{kin}(t = 0) = 0.0775, 0.25, 0.3$ which result in failure at some location in the domain.

One obtains a significantly different evolution for the $\theta = \pi/2$ boost. This clearly spoils the symmetry of the simulation, and is arguably a more realistic configuration than our previous considerations i.e. alignment of the two profiles. Failure occurs in regions displaced from the initial maximum, where the peaks of the initial momentum profile are located. This quickly drags the rest of the field down (including the maximum), resulting in a lopsided non-inflating bubble. However, a substantial initial kinetic energy is necessary to induce such a failure (now only an order of magnitude smaller than the potential), again a consequence of how smaller wavelength momentum stretch the field, creating large gradients that prevent further inhomogeneity developing.

Symmetry is restored for the final $\theta = \pi$ scenario. Curiously, we observe that failure occurs at the initial

minimum, despite the fact that it is initially boosted up the potential plateau. We see that regions where the initial momentum takes its highest value - coinciding with the regions of greatest gradient energy (see Fig. 4.9) - are prevented from falling into the minimum by the gradient pressure, even with such high initial velocity. As seen in the third plot of Fig. 4.11, the field in the central, inflating regions then begins large oscillations before dying down to a final value of roughly ϕ_0.

4.2.5 Discussion

We have used numerical relativity to simulate the early stages of small-field inflation with inhomogeneities in both the initial scalar-field and its velocity profile. This required the implementation of the new initial data solver CCTK [201], as well as a modified form of the moving puncture gauge. Specifically, we considered an α-attractor model (4.28) with a fixed initial sinusoidal field profile (4.32) and a varying initial sinusoidal momentum profile (4.33). We find that the necessary average kinetic energy to end inflation in at least some regions of the spacetime (or the entire spacetime, in the case of a uniform boost) is less than that of the potential for all cases considered. It should be pointed out that this model would naturally be more robust against field momenta if one were to shift the field further up along the plateau (though the size of the plateau is rather limited in small-field cases) as Hubble friction would play a more significant role. We performed this investigation not to test all the possible initial states, but rather to identify the main causes of inflationary failure as a result of the presence of the initial momentum.

To summarise, it is clear that the introduction of a low-energy initial field momentum generally reduces the robustness of small-field inflation (unless it is directed up the plateau only, which is likely quite a unique configuration subset). As in the case of ϕ perturbations [190], decreasing the wavelength of the momentum modes reduces their impact, requiring more energy to cause failure. This a consequence of the fact that shorter-wavelength Π modes act to inhomogenise the field, causing large gradients that slow the peaks down (and even reverse their trajectories). Moreover, the relative phase of the initial ϕ and Π profiles greatly impact the likeliness of failure, with maxima-aligned modes needing less energy to induce failure than initial Π modes that have maxima aligned with the minima of ϕ. This should not be too obvious, given that gradient pressure helps to shoot the initial minima down the potential. Nevertheless, such regions on failure trajectories are rescued by the gradients of the surrounding field, a phenomenon we find ubiquitous in our set-ups.

Indeed, with the exception of a uniform momentum, we find that only certain regions of the spacetime fall to the potential minimum. The location of these regions depend on the relative phase of the initial ϕ and Π profiles, leading either to a non-inflating bubble surrounded by inflating spacetime, or an inflating bubble surrounded by a non-inflating spacetime. Unfortunately, the gradients between these regions are too sharp to simulate accurately. However, if the inflating bubble/surroundings are of sufficiently large physical volume that they can be considered their own (effectively seperate) quadi-de Sitter spacetime, then one concludes that inflation has succeeded despite certain regions falling into the minimum. Otherwise, the field in the inflating regions will inevitably be dragged down into the minimum by the gradient pressure and

inflation ends with $\langle N \rangle \ll 100$ (or even $\ll 60$) e-folds. This leads us to potential avenues for future work. Modifications of the evolution code are required in order for us to run simulations for the entire inflationary period, which would allow us to observe the fate of the aforementioned bubbles. Morever, we also aim to repeat the investigation for large-field models, though preliminary tests suggest they are remarkably robust to large momentum perturbations (succeeding despite kinetic energies of many orders of magnitude larger than the potential). Lastly, recent work [203] has used novel gauge-independent diagnostics to claim that inflation does not truly occur under (physically valid) inhomogeneous initial conditions. This is a statement that we soon aim to address.

Chapter 5

Summary and future work

We have explored how the tools of NR can be used to investigate two rather distinct phenomena - one astrophysical and the other cosmological. We will now summarise our conclusions, and offer ideas for possible future projects.

Modified gravity

Our first topic centered on using NR in modified gravity. Specifically, it involved simulating binary black holes within quadratic scalar Gauss-Bonnet gravity. In this theory, it is possible for BHs to develop scalar hair. Whether this occurs depends on the mass and spin of the BH in question, as well as the (scalar-curvature) coupling strength. Consequently, one can obtain a variety of unscalarized/scalarized configurations of binary black hole evolutions. For a positive coupling, only one type transition is likely to occur - the formation of a descalarized remnant from scalarized progenitors (either or both can be scalarized). This is because for a positive coupling, it is the BH mass which generates positive (Gauss-bonnet) curvature, which triggers the (tachyonic) transition between states. Since the remnant will naturally have a large mass than its components, then only this dynamical descalarization process will occur. Demonstrating this process was the main result of our paper [5].
On the other hand, when the coupling is negative, the BH spin becomes the dominant factor. Through the generation of negative curvature, large spins (dimensionless spin $\chi > 0.5$) can trigger the tachyonic instability. Thus, given the variability in magnitude of BH spin during a binary merger, both (spin-induced) dynamical descalarization and scalarization are feasible.
The possibility of detecting one of these transitions is another question entirely. For descalarization cases, the presence of dipole or quadrupole scalar radiation during the inspiral and merger causes the inspiral to accelerate, culminating in a dephasing of the gravitational waveform. This is the most significant effect in regards to observation, and has been used for the shift-symmetric sGB to forecast constraints on the coupling [35]. Unfortunately, the possibility of observing the descalarization effect itself is less clear, given that it occurs on the same timescale as the merger/ringdown and thus a significant signal-to-noise ratio is necessary to identify the imprint it has on the waveform. Regarding spin-induced scalarization, the

prospect of observing the transition is even more remote (at least from work so far). This is because there is a prolonged delay between the merger and the generation of a consequential field magnitude. Thus, it is likely that the field growth will have no impact on the ringdown waveform.
This however, brings us to considering avenues of future work. Our projects involved simulating the scalar dynamics on a GR background, without any backreaction. If one were to include backreaction, so that the field stabilises to a stationary state, it is possible for a second - possibly observable - gravitational wave to be emitted via the relaxation process. Thus we see the importance of evolving these system within the full theory, to fully grasp the potential consequences. We therefore arrive at possibly the most important direction for future work - constructing well-posed formulations of modified gravity theories. Without such reconstructions, one cannot successfully evolve systems within the theory reliably (if at all). Fortunately, great strides have been made on this front. For example, there have been successful simulations of binary black hole mergers in sGB gravity using recently developed well-posed formulations [102, 204], though these have been restricted to the small-coupling regime. Ultimately though, we are a long way off from generating gravitational template banks in the vast plethora of modified gravity theories currently on offer. So, on the bright side, there is plenty more work to be done.

Inflation

The status of inflation is a somewhat contentious issues. It provides a simple and elegant solution to many problems that seized earlier models of the young universe. It also provides a natural mechanism for seeding structure formation. Nevertheless, it also subject to much criticism. Some of this criticism is caused by the ambiguous nature of inflation's initial state. Given the unknown form of quantum gravity, one should assume that inflation occurs from a generic initial state. As part of a growing collection of NR work on this subject, we attempted to help verify this assumption. Fixing an inhomogeneous inflaton field, we used a novel initial conditions solver [201] to simulate how a non-uniform initial momentum profile impacts the beginning of small-field inflation.
Overall, the inclusion of field momentum tended to stymie inflation in some regions of our domain, regardless of the shape of the profile. However, the energy required to end inflation in these regions varied greatly on the wavelength of the mode and its relative phase with the initial field fluctuation. Namely, shorter-wavelength modes needed more energy than their long-wavelength counterparts, and the necessary energy was minimised when the peaks of the field and its momentum were aligned. When the maxima of the momentum was aligned with minimum of the field, significant energies were required for inflationary failure (almost the energy of the potential itself for the second mode) despite the "sling-shot" effect of the gradient pressure. We attribute this to the combined effect of nearby, lower-velocity fields deflecting the trajectory as well as Hubble friction slowing the field down as it traverses the plateau.
However, the fate of inflation is not necessarily sealed once a regions fall into the potential minimum. In fact, rather than seeing the gradual pulling down of the rest of the field, we observe the formation of two distinct regions separated by a sharp gradient. These regions consist of either a non-inflating bubble surrounded by inflating spacetime, or the exact opposite (depending on the initial momentum profile).

Thus we speculate that such regions are causally disconnected, and so inflation may succeed in a restricted region of the domain.

Simulating the evolution of the aforementioned inflating regions throughout until the maximum number of e-folds has be attained is definitely a prospect for a future project. In fact there are many possibilities: investigating the effects of non-uniform momentum profiles on other models of inflation (such as large-field models); abandoning assumptions such as conformal flatness in the initial data for greater generality and simulating inflation in modified gravity theories. Most of these, however, will likely require significant (and novel) changes to the initial data solvers and evolution codes we employ. This is not entirely unexpected: for NR to fully grasp its potential in a wider (i.e. cosmological) setting, such developments are an absolute necessity and are certain to push the boundaries of possibility within the field.

Appendix A

Horndeski's theory

Horndeski's theory is the most general second-order, four dimensional scalar-tensor theory [21]. It's given by the Lagrangian [13]

$$\begin{aligned}\mathcal{L}_H =&\delta^{\alpha\beta\gamma}_{\mu\nu\sigma}\Big[\kappa_1\nabla^\mu\nabla_\alpha\phi R_{\beta\gamma}{}^{\nu\sigma} - \frac{4}{3}\partial_X\kappa_1\nabla^\mu\nabla_\alpha\phi\nabla^\nu\nabla_\beta\phi\nabla^\sigma\nabla_\gamma\phi \\ &+ \kappa_3\nabla_\alpha\phi\nabla^\mu\phi R_{\beta\gamma}{}^{\nu\sigma} - 4\partial_X\kappa_3\nabla_\alpha\phi\nabla^\mu\phi\nabla^\nu\nabla_\beta\phi\nabla^\sigma\nabla_\gamma\phi\Big] \\ &+ \delta^{\alpha\beta}_{\mu\nu}\Big[(F+2W)R_{\alpha\beta}{}^{\mu\nu} - 4\partial_X F\nabla^\mu\nabla_\alpha\phi\nabla^\nu\nabla_\beta\phi + 2\kappa_8\nabla_\alpha\phi\nabla^\mu\phi\nabla^\nu\nabla_\beta\phi\Big] \\ &- 3\Big[2\partial_\phi(F+2W) + X\kappa_8\Big]\nabla_\mu\nabla^\mu\phi + \kappa_9\,, \end{aligned} \tag{A.1}$$

where the arbitrary functions κ_i and F are both dependent on the scalar-field ϕ and $X = \nabla_\mu\nabla^\mu\phi$, the latter being constrained by $\partial_X F = \partial_\phi\kappa_1 - \kappa_3 - 2X\partial_X\kappa_3$.

Appendix B

Research work I

We assess the discretization error of our simulations by exemplarily running the head-on collision of equal-mass black holes that initially carry a bound-state scalar field with coupling parameter $\beta_2 = 0.36281$ at three different resolutions $\mathrm{d}x_\mathrm{c} = 1.0M$, $\mathrm{d}x_\mathrm{m} = 0.9M$ and $\mathrm{d}x_\mathrm{f} = 0.8M$. Here M is the system's total mass, which we set to unit. This setup corresponds to case (c) in Fig. 3.2 of the main text. Focusing on the scalar field monopole (Φ_{00}) and the gravitational quadrupole ($\Psi_{4,20}$) we compute the differences between the course and medium, and medium and high resolution runs. For Φ_{00}, we rescaled the latter difference by the convergence factor $Q_2 = 1.12$, as shown in the left panel in Fig. B.1, indicating second-order convergence. For $\Psi_{4,20}$, we rescaled the latter difference by $Q_4 = 1.39$, as shown in the right panel, indicating fourth-order convergence. Computing the relative difference $\Delta\Phi_{00}/\Phi_{00}$ between the coarsest resolution simulation with $\mathrm{d}x_\mathrm{c} = 1.0M$ and the second-order Richardson extrapolation, we find a numerical error of $\Delta\Phi_{00}/\Phi_{00} \lesssim 0.5\%$ as stated in the main text.

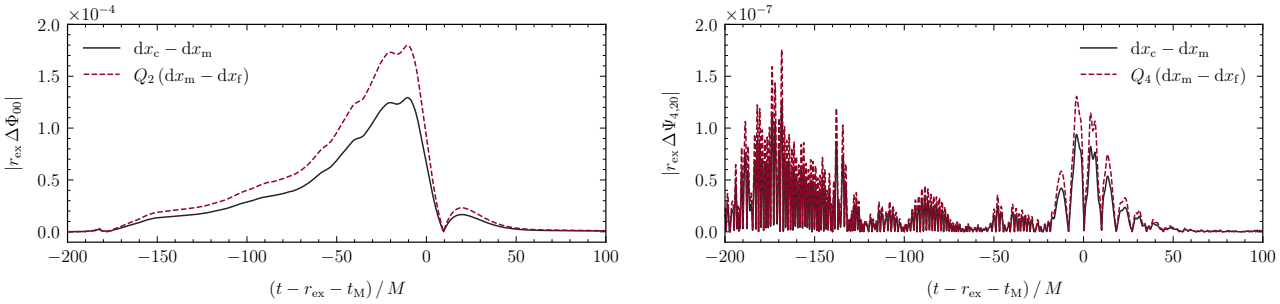

Figure B.1: Convergence plot for case (b) in Fig. 3.2 of the main text. We show the scalar field monopole (left panel) and the gravitational quadrupole (right panel) extracted at $r_\mathrm{ex} = 100M$ and shifted in time such that $(t - r_\mathrm{ex} - t_\mathrm{M})/M = 0$ corresponds to the BHs' merger. We calculate the differences between the coarse and medium resolutions, $\mathrm{d}x_\mathrm{c} = 1.0M$ and $\mathrm{d}x_\mathrm{m} = 0.9M$ (solid line), and medium and high resolutions, $\mathrm{d}x_\mathrm{m} = 0.9M$ and $\mathrm{d}x_\mathrm{f} = 0.8M$. For the scalar field monopole we rescale the latter by $Q_2 = 1.12$ (dashed line), indicating second-order convergence. For the gravitational quadrupole we rescale by $Q_4 = 1.39$ (dashed line), indicating fourth-order convergence, as stated in the main text.

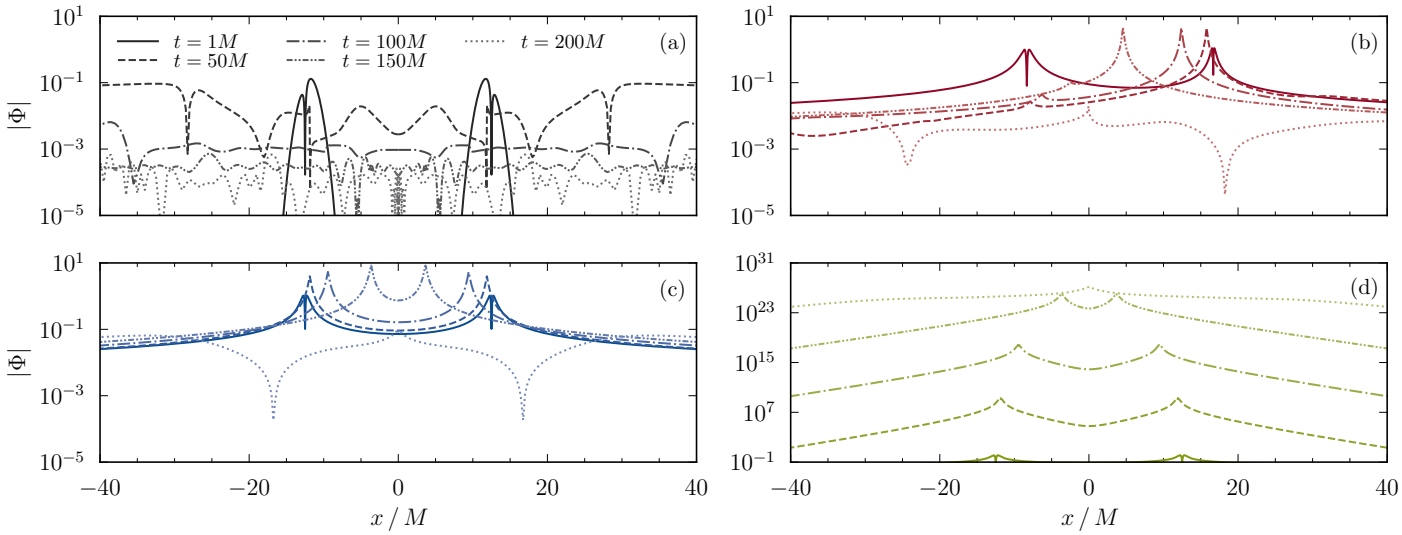

Figure B.2: Scalar field's profile along the collision axis x/M at different instances in time before, during and after the BH head-on collision for cases (a)–(d) defined in Fig. 3.2. The merger happens at $t_{\rm M} \sim 179.5M$.

Figure B.2 presents the scalar field profile along the collision axis x/M at different instances throughout the evolution before, near and after the merger of the BHs. In case (a), the scalar field is below the critical value to form any bound state configurations and, indeed, after a brief interaction at early times it decays already before the BHs collide. In cases (b) and (c), the scalar field forms a bound state that is anchored around the individual ($q = 1$) or smaller-mass BH ($q = 1/2$). As the BHs approach each other, the scalar field follows their dynamics and moves along the collision course with only small adjustments to its spatial configuration. After the BHs merge, the critical value $\beta_{2,\rm c}$ to form a bound state increases, i.e., the BH can no longer support a scalar bound state. Consequently, the configuration becomes subcritical and the scalar field is depleted, indicating dynamical descalarization of the BH binary. Finally, case (d) is set up such that the final configuration is near critical to form a bound state, always leading to a supercritical setup before merger. Indeed, we observe that the scalar field grows (exponentially), before settling to a constant-in-time radial profile after the merger. This rapid growth is due to the fact that $\beta_2 \sim 1.45123$ is four times larger than the critical scalarization value for the initial BHs.

Appendix C

Research work II

Setup	d/M	χ_1	χ_2	χ_f	β	β_c^i	β_c^f	process
A	10	0	0	0.68	-14.30	–	-12.96	$\bar{s} + \bar{s} \to s_\uparrow$
A1	6	0	0	0.68	-1000	–	-12.96	$\bar{s} + \bar{s} \to s_\uparrow$
A2	10	0.6	0.6	0.85	-2.9	-10.55	-3.01	$\bar{s}_\uparrow + \bar{s}_\uparrow \to s_\uparrow$
A3	10	0.6	0.6	0.85	-12.0	-10.55	-3.01	$s_\uparrow + s_\uparrow \to s_\uparrow$
A4	10	0.0	0.6	0.77	-12.0	-10.55	-5.59	$\bar{s} + s_\uparrow \to s_\uparrow$
B	10	-0.6	-0.6	0.48	-11.50	-10.55	–	$s_\downarrow + s_\downarrow \to \bar{s}_\uparrow$
B2	10	0.4	-0.6	0.64	-12.0	-10.55	-21.50	$\bar{s}_\uparrow + s_\downarrow \to \bar{s}_\uparrow$

Table C.1: List of our complete series of simulations. We denote the initial separation d/M with M being the total mass, $\chi_{i,1}$ and $\chi_{i,2}$ are the initial dimensionless spin parameters of each BH, and χ_f is the final dimensionless spin parameter of the remnant. We use $\bar{s}$ and s to denote unscalarized and scalarized states, respectively, and the subscript $\uparrow$ ($\downarrow$) indicates spin aligned (anti-aligned) with the orbital angular momentum. The coupling chosen for each simulation is given by β, whereas β_c^i and β_c^f denote the critical couplings for the component/remnant BHs respectively.

We ran a larger series of simulations, listed in Table C.1, of equal-mass BH binaries with varying initial spin that show a qualitatively same behaviour as the runs presented in the main text. In particular, we simulated a series of initially spinning, unscalarized black holes that formed a scalarized remnant with larger spin. We also list example simulations in which one or both initial BHs are scalarized and they merge into an unscalarized remnant.

C.1 Validation tests

To validate our code, we performed a suite of convergence tests. We ran Setup B, our numerically most demanding setup, at a lower resolution of $\mathrm{d}x_{\mathrm{low}} = 0.8M$ and a higher resolution of $\mathrm{d}x_{\mathrm{high}} = 0.625M$. The

runs in the main text use a medium resolution of $\mathrm{d}x_{\mathrm{med}} = 0.7M$. The grid setup is the same across all simulations. We estimated the order of convergence n and its associated convergence factor Q_n,

$$Q_n = \frac{(\mathrm{d}x_{\mathrm{low}})^n - (\mathrm{d}x_{\mathrm{med}})^n}{(\mathrm{d}x_{\mathrm{med}})^n - (\mathrm{d}x_{\mathrm{high}})^n} \,. \tag{C.1}$$

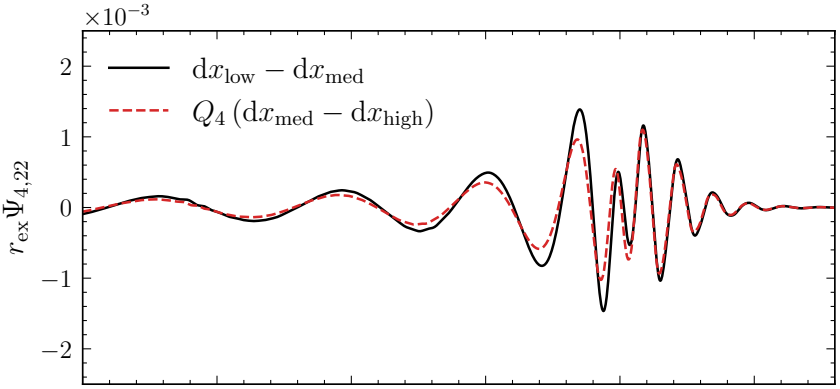

Figure C.1: Convergence plots for the $\ell = m = 0$ mode of the scalar field. We show the difference between the low and medium resolution run (solid line) and the medium and high resolution run (dashed line). The latter is rescaled by $Q_4 = 1.94$, indicating fourth order convergence. The lines are shifted in time such that $(t - r_{\mathrm{ex}} - t_{\mathrm{M}})/M = 0$ indicates the time of merger and they are rescaled by the extraction radius $r_{\mathrm{ex}} = 100M$.

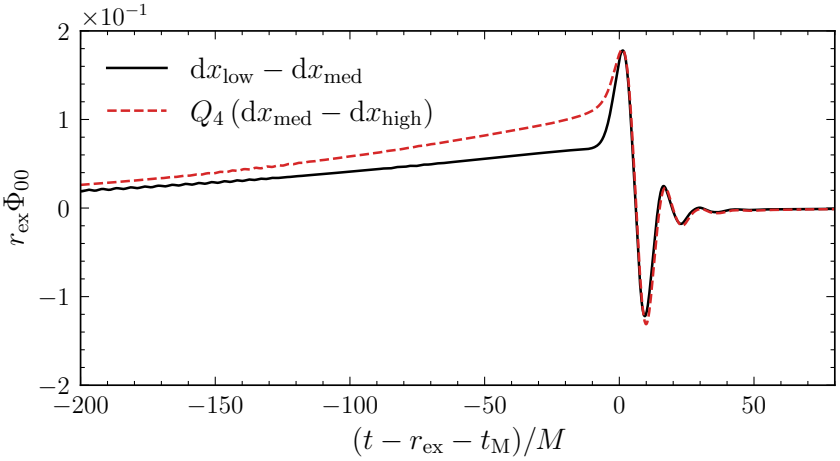

Figure C.2: Convergence plots for the $\ell = m = 2$ mode of the gravitational waveform. We show the difference between the low and medium resolution run (solid line) and the medium and high resolution run (dashed line). The latter is rescaled by $Q_4 = 1.94$, indicating fourth order convergence. The lines are shifted in time such that $(t - r_{\mathrm{ex}} - t_{\mathrm{M}})/M = 0$ indicates the time of merger and they are rescaled by the extraction radius $r_{\mathrm{ex}} = 100M$.

We computed the n and Q_n for the gravitational waveform, $\Psi_{4,22}$, of the background spacetime and for the scalar charge. We show the corresponding convergence plots in Fig. C.1. For $\Psi_{4,22}$ we find fourth order convergence, and we estimate the numerical (truncation) error to be $\Psi_{4,22}/\Psi_{4,22} \leqslant 0.8\%$. For the scalar

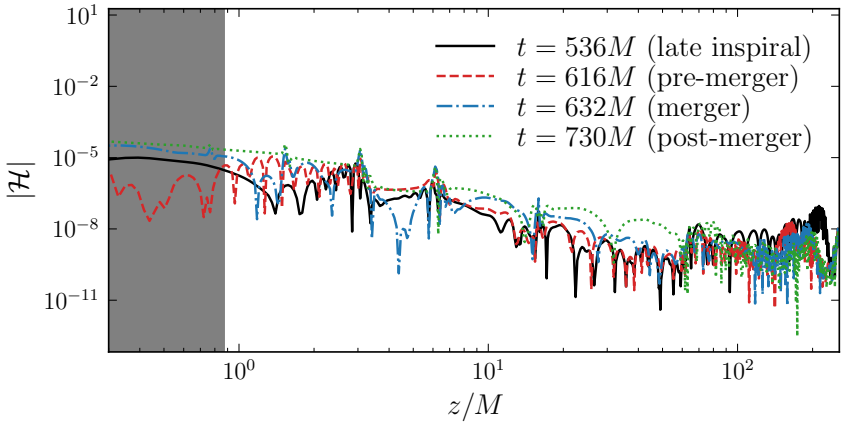

Figure C.3: Hamiltonian constraint along the z-axis during the late-inspiral (solid black), half an orbit before merger (dashed red), at the time of merger from the peak of the gravitational waveform (dash-dot blue) and $100M$ after merger (dotted green). The shaded region indicates the CAH, shown $100M$ after merger.

field charge, Φ_{00}, we also find fourth order convergence. performed a convergence test on its $\ell = m = 0$ multipole. We show our result in the right panel of Fig. C.1.

We find a cumulative error $\Delta\Phi_{00}/\Phi_{00} \leqslant 30\%$ in the late inspiral. The numerical error in the merger and ringdown is $\Delta\Phi_{00}/\Phi_{00} \leqslant 15\%$. As we restrict this work to a qualitative analysis, this error does not affect the main results of the paper. Further quantitative work, such as forecasting constraints on the theory would require this issue to be addressed.

Finally, in Fig. C.3, we show the Hamiltonian constraint $\mathcal{H}$ along the z-axis for Setup B at different time instants. The constraint violation remains below 10^{-5} outside the BH horizon through the simulation.

Appendix D

Research work III

To verify the validity of our results, we illustrate the evolution of the Hamiltonian and momentum constraints (Fig. D.1) for the $r_{kin}(t=0) = 0.005$ constant-momentum case. For the former, we calculate the average of the absolute value of the constraints over the entire numerical domain (black line), as well on specific spatial slices (red lines). We see a sharp increase in the violation of both constraints at $\langle N \rangle = 5$ on the face slice ($x = 0.0H_0$). This is a consequence of the field at the corners falling into the potential minimum, resulting in sharp poorly-resolved field gradients. As the constraint-violating models spread across the domain, we see that the central slice ($x = 0.5H_0$) begins to become contaminated at around $\langle N \rangle = 7$.

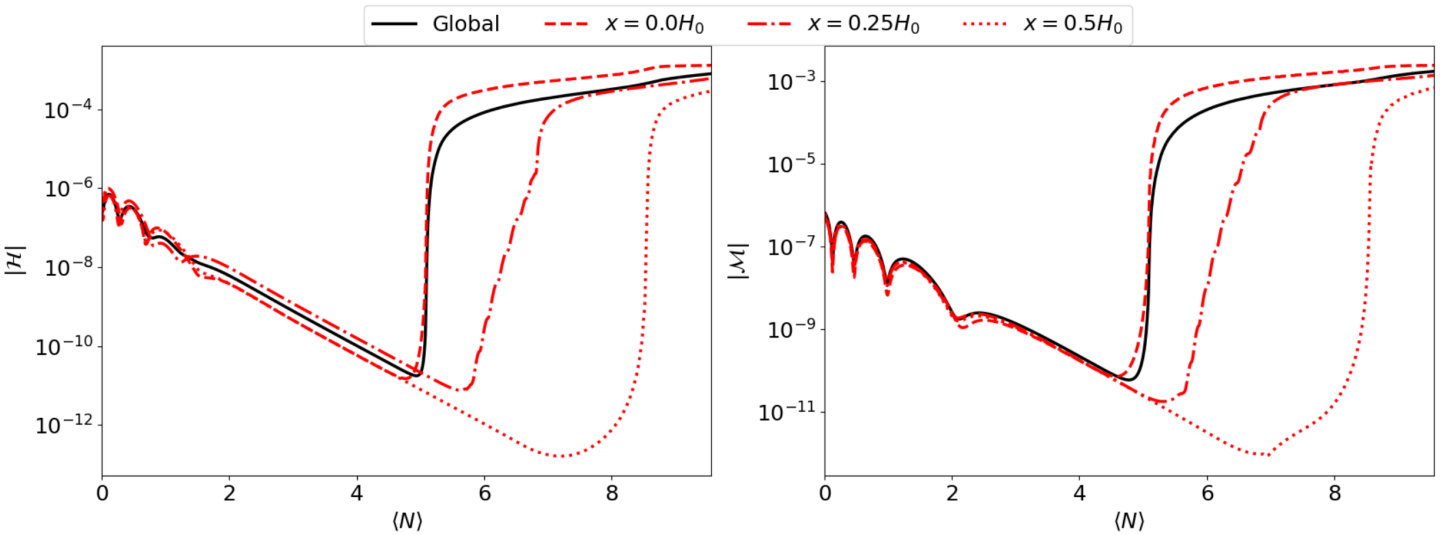

Figure D.1: Change in the absolute value of the Hamiltonian (left) and Momentum (right) constraints with the average number of e-folds for the $r_{kin}(t=0) = 0.005$ constant-momentum case. The black line illustrates the constraints averaged over the entire numerical domain, whereas the red lines show the constraints averaged on specific slices of $x = const$.

However, we also perform convergence tests on the scalar-field minimum and maximum , as shown in Fig. D.2. We observe exact second-order convergence at the minimum until $\langle N \rangle = 5$. More importantly,

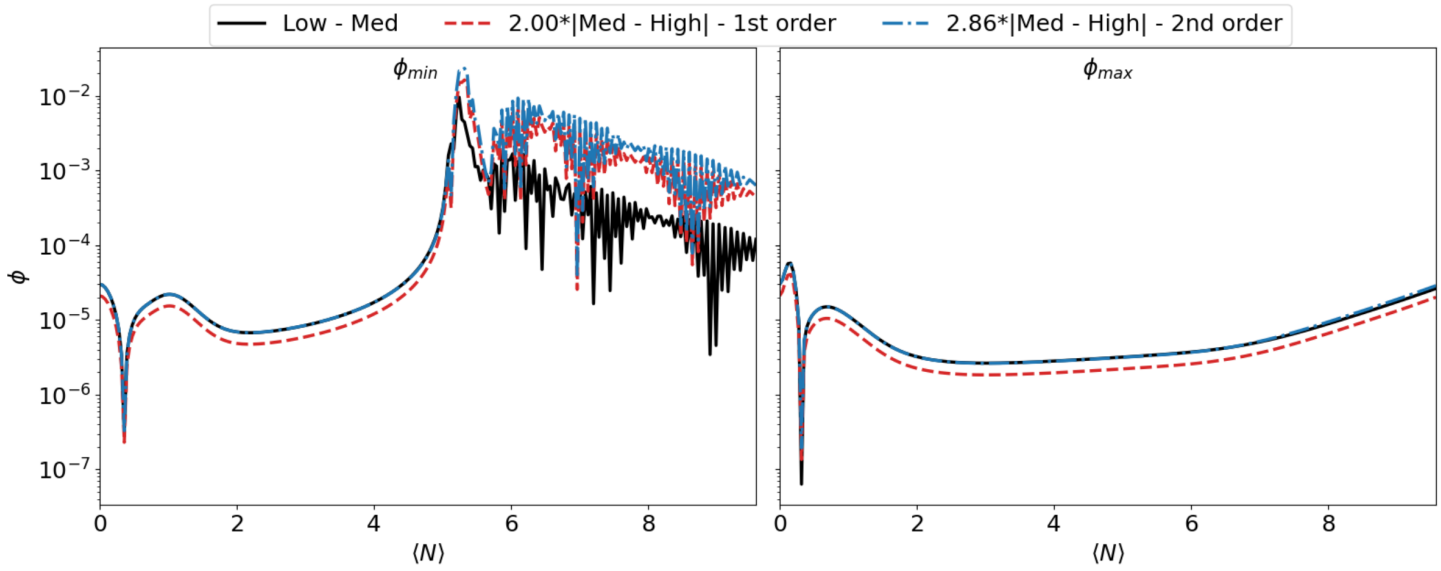

Figure D.2: Convergence plots of the scalar-field minimum (left) and maximum (right) for the $r_{kin}(t = 0) = 0.005$ constant-momentum case. The black line shows the absolute difference between field of the low ($\mathrm{d}x = 0.5$) and medium ($\mathrm{d}x = 0.33$) resolution runs. The red dashed and blue dash-dotted lines shows the absolute difference between field of the medium ($\mathrm{d}x = 0.5$) and high ($\mathrm{d}x = 0.25$) resolution runs, re-scaled by the 1st and 2nd order convergence factors respectively.

we also see excellent second-order convergence at the maximum until the end of the simulation. Thus, the evolution of the maximum remains trustworthy despite the constraint violations on that slice (which likely have not reached the very centre of the domain where the maximum field lies). We expect the minimum to simply oscillate about the potential, thus we are not too concerned about its behaviour once it has fallen down the potential.

Bibliography

[1] Thomas W. Baumgarte and Stuart L. Shapiro. *Numerical Relativity: Solving Einstein's Equations on the Computer*. Cambridge University Press, 2010.

[2] Miguel Alcubierre. *Introduction to 3+1 numerical relativity*. International series of monographs on physics. Oxford Univ. Press, Oxford, 2008.

[3] Jose María Ezquiaga and Miguel Zumalacárregui. Dark Energy in light of Multi-Messenger Gravitational-Wave astronomy. *Front. Astron. Space Sci.*, 5:44, 2018.

[4] Carlos A. R. Herdeiro, Eugen Radu, Hector O. Silva, Thomas P. Sotiriou, and Nicolás Yunes. Spin-induced scalarized black holes. *Phys. Rev. Lett.*, 126(1):011103, 2021.

[5] Hector O. Silva, Helvi Witek, Matthew Elley, and Nicolás Yunes. Dynamical Descalarization in Binary Black Hole Mergers. *Phys. Rev. Lett.*, 127(3):031101, 2021.

[6] Matthew Elley, Hector O. Silva, Helvi Witek, and Nicolás Yunes. Spin-induced dynamical scalarization, descalarization, and stealthness in scalar-Gauss-Bonnet gravity during a black hole coalescence. *Phys. Rev. D*, 106(4):044018, 2022.

[7] Masaru Shibata. *Numerical Relativity*. World Scientific Publishing Co. Pte. Ltd., 2016.

[8] Miguel Alcubierre. *Introduction to 3+1 numerical relativity*. International Series of Monographs on Physics. Oxford Univ. Press, Oxford, 2008.

[9] Masaru Shibata and Takashi Nakamura. Evolution of three-dimensional gravitational waves: Harmonic slicing case. *Phys.Rev.*, D52:5428–5444, 1995.

[10] Thomas W. Baumgarte and Stuart L. Shapiro. On the numerical integration of Einstein's field equations. *Phys. Rev.*, D59:024007, 1999.

[11] Katy Clough. *Scalar Fields in Numerical General Relativity*. PhD thesis, 2017.

[12] Clifford M. Will. The Confrontation between General Relativity and Experiment. *Living Rev. Rel.*, 17:4, 2014.

[13] Timothy Clifton, Pedro G. Ferreira, Antonio Padilla, and Constantinos Skordis. Modified Gravity and Cosmology. *Phys. Rept.*, 513:1–189, 2012.

[14] Thibault Damour and Kenneth Nordtvedt. General relativity as a cosmological attractor of tensor scalar theories. *Phys. Rev. Lett.*, 70:2217–2219, 1993.

[15] John D. Barrow and Kei-ichi Maeda. Extended inflationary universes. *Nucl. Phys. B*, 341:294–308, 1990.

[16] J. Garcia-Bellido and M. Quiros. Extended Inflation in Scalar - Tensor Theories of Gravity. *Phys. Lett. B*, 243:45–51, 1990.

[17] Francesca Perrotta, Carlo Baccigalupi, and Sabino Matarrese. Extended quintessence. *Phys. Rev. D*, 61:023507, 1999.

[18] Carlo Baccigalupi, Sabino Matarrese, and Francesca Perrotta. Tracking extended quintessence. *Phys. Rev. D*, 62:123510, 2000.

[19] Jose María Ezquiaga and Miguel Zumalacárregui. Dark Energy After GW170817: Dead Ends and the Road Ahead. *Phys. Rev. Lett.*, 119(25):251304, 2017.

[20] K. S. Stelle. Classical Gravity with Higher Derivatives. *Gen. Rel. Grav.*, 9:353–371, 1978.

[21] Gregory Walter Horndeski. Second-order scalar-tensor field equations in a four-dimensional space. *Int. J. Theor. Phys.*, 10:363–384, 1974.

[22] Pedro G. S. Fernandes, Pedro Carrilho, Timothy Clifton, and David J. Mulryne. The 4D Einstein–Gauss–Bonnet theory of gravity: a review. *Class. Quant. Grav.*, 39(6):063001, 2022.

[23] Sean M. Carroll. *Spacetime and Geometry*. Cambridge University Press, 7 2019.

[24] S. W. Hawking. Black holes in the Brans-Dicke theory of gravitation. *Commun. Math. Phys.*, 25:167–171, 1972.

[25] J. D. Bekenstein. Novel "no-scalar-hair" theorem for black holes. *Phys. Rev. D*, 51(12):R6608, 1995.

[26] Thomas P. Sotiriou and Valerio Faraoni. Black holes in scalar-tensor gravity. *Phys. Rev. Lett.*, 108:081103, 2012.

[27] Lam Hui and Alberto Nicolis. No-Hair Theorem for the Galileon. *Phys. Rev. Lett.*, 110:241104, 2013.

[28] Thomas P. Sotiriou and Shuang-Yong Zhou. Black hole hair in generalized scalar-tensor gravity. *Phys. Rev. Lett.*, 112:251102, 2014.

[29] Thomas P. Sotiriou. Black Holes and Scalar Fields. *Class. Quant. Grav.*, 32(21):214002, 2015.

[30] Thomas P. Sotiriou and Shuang-Yong Zhou. Black hole hair in generalized scalar-tensor gravity: An explicit example. *Phys. Rev. D*, 90:124063, 2014.

[31] P. Kanti, N. E. Mavromatos, J. Rizos, K. Tamvakis, and E. Winstanley. Dilatonic black holes in higher curvature string gravity. *Phys. Rev. D*, 54:5049–5058, 1996.

[32] Hector O. Silva, Jeremy Sakstein, Leonardo Gualtieri, Thomas P. Sotiriou, and Emanuele Berti. Spontaneous scalarization of black holes and compact stars from a Gauss-Bonnet coupling. *Phys. Rev. Lett.*, 120(13):131104, 2018.

[33] Daniela D. Doneva and Stoytcho S. Yazadjiev. New Gauss-Bonnet Black Holes with Curvature-Induced Scalarization in Extended Scalar-Tensor Theories. *Phys. Rev. Lett.*, 120(13):131103, 2018.

[34] Thibault Damour and Gilles Esposito-Farese. Nonperturbative strong field effects in tensor - scalar theories of gravitation. *Phys. Rev. Lett.*, 70:2220–2223, 1993.

[35] Helvi Witek, Leonardo Gualtieri, Paolo Pani, and Thomas P. Sotiriou. Black holes and binary mergers in scalar Gauss-Bonnet gravity: scalar field dynamics. *Phys. Rev. D*, 99(6):064035, 2019.

[36] Emanuele Berti et al. Testing General Relativity with Present and Future Astrophysical Observations. *Class. Quant. Grav.*, 32:243001, 2015.

[37] B.P. Abbott et al. GWTC-1: A Gravitational-Wave Transient Catalog of Compact Binary Mergers Observed by LIGO and Virgo during the First and Second Observing Runs. *Phys. Rev. X*, 9(3):031040, 2019.

[38] R. Abbott et al. GWTC-2: Compact Binary Coalescences Observed by LIGO and Virgo During the First Half of the Third Observing Run. *Phys. Rev. X*, 11:021053, 2021.

[39] Nicolás Yunes and Xavier Siemens. Gravitational-Wave Tests of General Relativity with Ground-Based Detectors and Pulsar Timing-Arrays. *Living Rev. Rel.*, 16:9, 2013.

[40] Kent Yagi and Leo C. Stein. Black Hole Based Tests of General Relativity. *Class. Quant. Grav.*, 33(5):054001, 2016.

[41] B.P. Abbott et al. Tests of General Relativity with the Binary Black Hole Signals from the LIGO-Virgo Catalog GWTC-1. *Phys. Rev. D*, 100(10):104036, 2019.

[42] R. Abbott et al. Tests of general relativity with binary black holes from the second LIGO-Virgo gravitational-wave transient catalog. *Phys. Rev. D*, 103(12):122002, 2021.

[43] Nicolas Yunes, Kent Yagi, and Frans Pretorius. Theoretical Physics Implications of the Binary Black-Hole Mergers GW150914 and GW151226. *Phys. Rev.*, D94(8):084002, 2016.

[44] Remya Nair, Scott Perkins, Hector O. Silva, and Nicolás Yunes. Fundamental Physics Implications for Higher-Curvature Theories from Binary Black Hole Signals in the LIGO-Virgo Catalog GWTC-1. *Phys. Rev. Lett.*, 123(19):191101, 2019.

[45] Zack Carson and Kent Yagi. Testing General Relativity with Gravitational Waves. 11 2020.

[46] R.R. Metsaev and Arkady A. Tseytlin. Order α' (Two Loop) Equivalence of the String Equations of Motion and the Sigma Model Weyl Invariance Conditions: Dependence on the Dilaton and the Antisymmetric Tensor. *Nucl. Phys. B*, 293:385–419, 1987.

[47] Christos Charmousis. From Lovelock to Horndeski's Generalized Scalar Tensor Theory. *Lect. Notes Phys.*, 892:25–56, 2015.

[48] S. Mignemi and N.R. Stewart. Charged black holes in effective string theory. *Phys. Rev. D*, 47:5259–5269, 1993.

[49] Takashi Torii, Hiroki Yajima, and Kei-ichi Maeda. Dilatonic black holes with Gauss-Bonnet term. *Phys. Rev. D*, 55:739–753, 1997.

[50] Nicolas Yunes and Leo C. Stein. Non-Spinning Black Holes in Alternative Theories of Gravity. *Phys. Rev. D*, 83:104002, 2011.

[51] Kartik Prabhu and Leo C. Stein. Black hole scalar charge from a topological horizon integral in Einstein-dilaton-Gauss-Bonnet gravity. *Phys. Rev. D*, 98(2):021503, 2018.

[52] Thibault Damour and Gilles Esposito-Farèse. Tensor-scalar gravity and binary pulsar experiments. *Phys. Rev. D*, 54:1474–1491, 1996.

[53] Tomohiro Harada. Stability analysis of spherically symmetric star in scalar - tensor theories of gravity. *Prog. Theor. Phys.*, 98:359–379, 1997.

[54] Enrico Barausse, Carlos Palenzuela, Marcelo Ponce, and Luis Lehner. Neutron-star mergers in scalar-tensor theories of gravity. *Phys. Rev. D*, 87:081506, 2013.

[55] Carlos Palenzuela, Enrico Barausse, Marcelo Ponce, and Luis Lehner. Dynamical scalarization of neutron stars in scalar-tensor gravity theories. *Phys. Rev. D*, 89(4):044024, 2014.

[56] Masaru Shibata, Keisuke Taniguchi, Hirotada Okawa, and Alessandra Buonanno. Coalescence of binary neutron stars in a scalar-tensor theory of gravity. *Phys. Rev. D*, 89(8):084005, 2014.

[57] Noah Sennett, Lijing Shao, and Jan Steinhoff. Effective action model of dynamically scalarizing binary neutron stars. *Phys. Rev. D*, 96(8):084019, 2017.

[58] G. Antoniou, A. Bakopoulos, and P. Kanti. Evasion of No-Hair Theorems and Novel Black-Hole Solutions in Gauss-Bonnet Theories. *Phys. Rev. Lett.*, 120(13):131102, 2018.

[59] G. Antoniou, A. Bakopoulos, and P. Kanti. Black-Hole Solutions with Scalar Hair in Einstein-Scalar-Gauss-Bonnet Theories. *Phys. Rev. D*, 97(8):084037, 2018.

[60] Andrea Maselli, Paolo Pani, Leonardo Gualtieri, and Valeria Ferrari. Rotating black holes in Einstein-Dilaton-Gauss-Bonnet gravity with finite coupling. *Phys. Rev. D*, 92(8):083014, 2015.

[61] Kent Yagi, Leo C. Stein, and Nicolas Yunes. Challenging the Presence of Scalar Charge and Dipolar Radiation in Binary Pulsars. *Phys. Rev. D*, 93(2):024010, 2016.

[62] Caio F.B. Macedo, Jeremy Sakstein, Emanuele Berti, Leonardo Gualtieri, Hector O. Silva, and Thomas P. Sotiriou. Self-interactions and Spontaneous Black Hole Scalarization. *Phys. Rev. D*, 99(10):104041, 2019.

[63] Caio F.B. Macedo. Scalar modes, spontaneous scalarization and circular null-geodesics of black holes in scalar-Gauss–Bonnet gravity. *Int. J. Mod. Phys. D*, 29(11):2041006, 2020.

[64] Justin L. Ripley and Frans Pretorius. Dynamics of a $\mathbb{Z}_2$ symmetric EdGB gravity in spherical symmetry. *Class. Quant. Grav.*, 37(15):155003, 2020.

[65] Alexandru Dima, Enrico Barausse, Nicola Franchini, and Thomas P. Sotiriou. Spin-induced black hole spontaneous scalarization. *Phys. Rev. Lett.*, 125(23):231101, 2020.

[66] Shahar Hod. Onset of spontaneous scalarization in spinning Gauss-Bonnet black holes. *Phys. Rev. D*, 102(8):084060, 2020.

[67] Daniela D. Doneva, Lucas G. Collodel, Christian J. Krüger, and Stoytcho S. Yazadjiev. Black hole scalarization induced by the spin: 2+1 time evolution. *Phys. Rev. D*, 102(10):104027, 2020.

[68] Daniela D. Doneva and Stoytcho S. Yazadjiev. On the dynamics of the nonrotating and rotating black hole scalarization. 1 2021.

[69] Pedro V.P. Cunha, Carlos A.R. Herdeiro, and Eugen Radu. Spontaneously Scalarized Kerr Black Holes in Extended Scalar-Tensor–Gauss-Bonnet Gravity. *Phys. Rev. Lett.*, 123(1):011101, 2019.

[70] Lucas G. Collodel, Burkhard Kleihaus, Jutta Kunz, and Emanuele Berti. Spinning and excited black holes in Einstein-scalar-Gauss–Bonnet theory. *Class. Quant. Grav.*, 37(7):075018, 2020.

[71] Emanuele Berti, Lucas G. Collodel, Burkhard Kleihaus, and Jutta Kunz. Spin-induced black-hole scalarization in Einstein-scalar-Gauss-Bonnet theory. *Phys. Rev. Lett.*, 126(1):011104, 2021.

[72] Manuela Campanelli, C.O. Lousto, P. Marronetti, and Y. Zlochower. Accurate evolutions of orbiting black-hole binaries without excision. *Phys. Rev. Lett.*, 96:111101, 2006.

[73] John G. Baker, Joan Centrella, Dae-Il Choi, Michael Koppitz, and James van Meter. Gravitational wave extraction from an inspiraling configuration of merging black holes. *Phys. Rev. Lett.*, 96:111102, 2006.

[74] Dieter R. Brill and Richard W. Lindquist. Interaction energy in geometrostatics. *Phys. Rev.*, 131:471–476, 1963.

[75] Richard W. Lindquist. Initial-Value Problem on Einstein-Rosen Manifolds. *Journal of Mathematical Physics*, 4(7):938–950, 1963.

[76] Jeffrey M. Bowen and Jr. York, James W. Time asymmetric initial data for black holes and black hole collisions. *Phys. Rev. D*, 21:2047–2056, 1980.

[77] Steven Brandt and Bernd Bruegmann. A Simple construction of initial data for multiple black holes. *Phys. Rev. Lett.*, 78:3606–3609, 1997.

[78] Helvi Witek, Miguel Zilhão, Giuseppe Ficarra, and Matthew Elley. Canuda: a public numerical relativity library to probe fundamental physics, May 2020.

[79] Robert Benkel, Thomas P. Sotiriou, and Helvi Witek. Dynamical scalar hair formation around a Schwarzschild black hole. *Phys. Rev. D*, 94(12):121503, 2016.

[80] Robert Benkel, Thomas P. Sotiriou, and Helvi Witek. Black hole hair formation in shift-symmetric generalised scalar-tensor gravity. *Class. Quant. Grav.*, 34(6):064001, 2017.

[81] Steven R. Brandt et al. The Einstein Toolkit, May 2020. To find out more, visit http://einsteintoolkit.org.

[82] Frank Löffler et al. The Einstein Toolkit: A Community Computational Infrastructure for Relativistic Astrophysics. *Class. Quant. Grav.*, 29:115001, 2012.

[83] Erik Schnetter, Scott H. Hawley, and Ian Hawke. Evolutions in 3-D numerical relativity using fixed mesh refinement. *Class. Quant. Grav.*, 21:1465–1488, 2004.

[84] C.O. Lousto and Richard H. Price. Radiation content of conformally flat initial data. *Phys. Rev. D*, 69:087503, 2004.

[85] Ulrich Sperhake, Vitor Cardoso, Christian D. Ott, Erik Schnetter, and Helvi Witek. Extreme black hole simulations: collisions of unequal mass black holes and the point particle limit. *Phys. Rev. D*, 84:084038, 2011.

[86] Alessandra Buonanno, Gregory B. Cook, and Frans Pretorius. Inspiral, merger and ring-down of equal-mass black-hole binaries. *Phys. Rev. D*, 75:124018, 2007.

[87] Mohammed Khalil, Noah Sennett, Jan Steinhoff, and Alessandra Buonanno. Theory-agnostic framework for dynamical scalarization of compact binaries. *Phys. Rev. D*, 100(12):124013, 2019.

[88] Kent Yagi, Leo C. Stein, Nicolás Yunes, and Takahiro Tanaka. Post-Newtonian, Quasi-Circular Binary Inspirals in Quadratic Modified Gravity. *Phys. Rev. D*, 85:064022, 2012. [Erratum: Phys.Rev.D 93, 029902 (2016)].

[89] Félix-Louis Julié and Emanuele Berti. Post-Newtonian dynamics and black hole thermodynamics in Einstein-scalar-Gauss-Bonnet gravity. *Phys. Rev. D*, 100(10):104061, 2019.

[90] Banafsheh Shiralilou, Tanja Hinderer, Samaya Nissanke, Néstor Ortiz, and Helvi Witek. Nonlinear curvature effects in gravitational waves from inspiralling black hole binaries. 12 2020.

[91] Pratik Wagle, Alexander Saffer, and Nicolas Yunes. Polarization modes of gravitational waves in quadratic gravity. *Phys. Rev. D*, 100(12):124007, 2019.

[92] Maria Okounkova. Numerical relativity simulation of GW150914 in Einstein dilaton Gauss-Bonnet gravity. *Phys. Rev. D*, 102(8):084046, 2020.

[93] Áron D. Kovács and Harvey S. Reall. Well-posed formulation of Lovelock and Horndeski theories. *Phys. Rev. D*, 101(12):124003, 2020.

[94] Áron D. Kovács and Harvey S. Reall. Well-Posed Formulation of Scalar-Tensor Effective Field Theory. *Phys. Rev. Lett.*, 124(22):221101, 2020.

[95] Justin L. Ripley and Frans Pretorius. Hyperbolicity in Spherical Gravitational Collapse in a Horndeski Theory. *Phys. Rev. D*, 99(8):084014, 2019.

[96] Justin Ripley and Frans Pretorius. Gravitational collapse in Einstein dilaton-Gauss–Bonnet gravity. *Class. Quant. Grav.*, 36(13):134001, 2019.

[97] Justin L. Ripley and Frans Pretorius. Scalarized Black Hole dynamics in Einstein dilaton Gauss-Bonnet Gravity. *Phys. Rev. D*, 101(4):044015, 2020.

[98] Giuseppe Papallo and Harvey S. Reall. On the local well-posedness of Lovelock and Horndeski theories. *Phys. Rev. D*, 96(4):044019, 2017.

[99] Giuseppe Papallo. On the hyperbolicity of the most general Horndeski theory. *Phys. Rev. D*, 96(12):124036, 2017.

[100] Félix-Louis Julié and Emanuele Berti. $d + 1$ formalism in Einstein-scalar-Gauss-Bonnet gravity. *Phys. Rev. D*, 101(12):124045, 2020.

[101] Helvi Witek, Leonardo Gualtieri, and Paolo Pani. Towards numerical relativity in scalar Gauss-Bonnet gravity: $3+1$ decomposition beyond the small-coupling limit. *Phys. Rev. D*, 101(12):124055, 2020.

[102] William E. East and Justin L. Ripley. Evolution of Einstein-scalar-Gauss-Bonnet gravity using a modified harmonic formulation. 11 2020.

[103] R. Abbott et al. GWTC-3: Compact Binary Coalescences Observed by LIGO and Virgo During the Second Part of the Third Observing Run, 11 2021.

[104] Emanuele Berti, Kent Yagi, and Nicolás Yunes. Extreme Gravity Tests with Gravitational Waves from Compact Binary Coalescences: (I) Inspiral-Merger. *Gen. Rel. Grav.*, 50(4):46, 2018.

[105] Emanuele Berti, Kent Yagi, Huan Yang, and Nicolás Yunes. Extreme Gravity Tests with Gravitational Waves from Compact Binary Coalescences: (II) Ringdown. *Gen. Rel. Grav.*, 50(5):49, 2018.

[106] B. P. Abbott et al. Tests of general relativity with GW150914. *Phys. Rev. Lett.*, 116(22):221101, 2016. [Erratum: Phys.Rev.Lett. 121, 129902 (2018)].

[107] B. P. Abbott et al. Tests of General Relativity with GW170817. *Phys. Rev. Lett.*, 123(1):011102, 2019.

[108] Alejandro Cardenas-Avendano, Sourabh Nampalliwar, and Nicolas Yunes. Gravitational-wave versus X-ray tests of strong-field gravity. *Class. Quant. Grav.*, 37(13):135008, 2020.

[109] Hector O. Silva, A. Miguel Holgado, Alejandro Cárdenas-Avendaño, and Nicolás Yunes. Astrophysical and theoretical physics implications from multimessenger neutron star observations. *Phys. Rev. Lett.*, 126(18):181101, 2021.

[110] R. Abbott et al. Tests of General Relativity with GWTC-3, 12 2021.

[111] Abhirup Ghosh, Richard Brito, and Alessandra Buonanno. Constraints on quasinormal-mode frequencies with LIGO-Virgo binary–black-hole observations. *Phys. Rev. D*, 103(12):124041, 2021.

[112] Gregorio Carullo. Enhancing modified gravity detection from gravitational-wave observations using the parametrized ringdown spin expansion coeffcients formalism. *Phys. Rev. D*, 103(12):124043, 2021.

[113] Noah Sennett, Richard Brito, Alessandra Buonanno, Victor Gorbenko, and Leonardo Senatore. Gravitational-Wave Constraints on an Effective Field-Theory Extension of General Relativity. *Phys. Rev. D*, 102(4):044056, 2020.

[114] Ajit Kumar Mehta, Alessandra Buonanno, Roberto Cotesta, Abhirup Ghosh, Noah Sennett, and Jan Steinhoff. Tests of General Relativity with Gravitational-Wave Observations using a Flexible-Theory-Independent Method, 3 2022.

[115] Junjie Zhao, Lijing Shao, Zhoujian Cao, and Bo-Qiang Ma. Reduced-order surrogate models for scalar-tensor gravity in the strong field regime and applications to binary pulsars and GW170817. *Phys. Rev. D*, 100(6):064034, 2019.

[116] Leong Khim Wong, Carlos A. R. Herdeiro, and Eugen Radu. Constraining spontaneous black hole scalarization in scalar-tensor-Gauss-Bonnet theories with current gravitational-wave data, 4 2022.

[117] Kei Yamada, Tatsuya Narikawa, and Takahiro Tanaka. Testing massive-field modifications of gravity via gravitational waves. *PTEP*, 2019(10):103E01, 2019.

[118] Scott E. Perkins, Remya Nair, Hector O. Silva, and Nicolas Yunes. Improved gravitational-wave constraints on higher-order curvature theories of gravity. *Phys. Rev. D*, 104(2):024060, 2021.

[119] Zhenwei Lyu, Nan Jiang, and Kent Yagi. Constraints on Einstein-dilation-Gauss-Bonnet gravity from black hole-neutron star gravitational wave events. *Phys. Rev. D*, 105(6):064001, 2022.

[120] Hector O. Silva, Abhirup Ghosh, and Alessandra Buonanno. Black-hole ringdown as a probe of higher-curvature gravity theories, 5 2022.

[121] P. Kanti and K. Tamvakis. Classical moduli O(α') hair. *Phys. Rev. D*, 52:3506–3511, 1995.

[122] Pablo A. Cano and Alejandro Ruipérez. String gravity in $D = 4$. *Phys. Rev. D*, 105(4):044022, 2022.

[123] Tsutomu Kobayashi, Masahide Yamaguchi, and Jun'ichi Yokoyama. Generalized G-inflation: Inflation with the most general second-order field equations. *Prog. Theor. Phys.*, 126:511–529, 2011.

[124] Tsutomu Kobayashi. Horndeski theory and beyond: a review. *Rept. Prog. Phys.*, 82(8):086901, 2019.

[125] Kent Yagi, Nicolas Yunes, and Takahiro Tanaka. Gravitational Waves from Quasi-Circular Black Hole Binaries in Dynamical Chern-Simons Gravity. *Phys. Rev. Lett.*, 109:251105, 2012. [Erratum: Phys.Rev.Lett. 116, 169902 (2016), Erratum: Phys.Rev.Lett. 124, 029901 (2020)].

[126] Kent Yagi, Leo C. Stein, Nicolas Yunes, and Takahiro Tanaka. Isolated and Binary Neutron Stars in Dynamical Chern-Simons Gravity. *Phys. Rev. D*, 87:084058, 2013. [Erratum: Phys.Rev.D 93, 089909 (2016)].

[127] Banafsheh Shiralilou, Tanja Hinderer, Samaya M. Nissanke, Néstor Ortiz, and Helvi Witek. Post-Newtonian gravitational and scalar waves in scalar-Gauss–Bonnet gravity. *Class. Quant. Grav.*, 39(3):035002, 2022.

[128] Félix-Louis Julié, Hector O. Silva, Emanuele Berti, and Nicolás Yunes. Black hole sensitivities in Einstein-scalar-Gauss-Bonnet gravity, 2 2022.

[129] William E. East and Justin L. Ripley. Dynamics of Spontaneous Black Hole Scalarization and Mergers in Einstein-Scalar-Gauss-Bonnet Gravity. *Phys. Rev. Lett.*, 127(10):101102, 2021.

[130] Daniela D. Doneva, Alex Vañó Viñuales, and Stoytcho S. Yazadjiev. Dynamical descalarization with a jump during black hole merger, 4 2022.

[131] Paolo Pani and Vitor Cardoso. Are black holes in alternative theories serious astrophysical candidates? The Case for Einstein-Dilaton-Gauss-Bonnet black holes. *Phys. Rev.*, D79:084031, 2009.

[132] Jose Luis Blázquez-Salcedo, Caio F. B. Macedo, Vitor Cardoso, Valeria Ferrari, Leonardo Gualtieri, Fech Scen Khoo, Jutta Kunz, and Paolo Pani. Perturbed black holes in Einstein-dilaton-Gauss-Bonnet gravity: Stability, ringdown, and gravitational-wave emission. *Phys. Rev. D*, 94(10):104024, 2016.

[133] Jose Luis Blázquez-Salcedo, Daniela D. Doneva, Sarah Kahlen, Jutta Kunz, Petya Nedkova, and Stoytcho S. Yazadjiev. Axial perturbations of the scalarized Einstein-Gauss-Bonnet black holes. *Phys. Rev. D*, 101(10):104006, 2020.

[134] Jose Luis Blázquez-Salcedo, Daniela D. Doneva, Sarah Kahlen, Jutta Kunz, Petya Nedkova, and Stoytcho S. Yazadjiev. Polar quasinormal modes of the scalarized Einstein-Gauss-Bonnet black holes. *Phys. Rev. D*, 102(2):024086, 2020.

[135] Lorenzo Pierini and Leonardo Gualtieri. Quasi-normal modes of rotating black holes in Einstein-dilaton Gauss-Bonnet gravity: the first order in rotation. *Phys. Rev. D*, 103:124017, 2021.

[136] Albert Bryant, Hector O. Silva, Kent Yagi, and Kostas Glampedakis. Eikonal quasinormal modes of black holes beyond general relativity. III. Scalar Gauss-Bonnet gravity. *Phys. Rev. D*, 104(4):044051, 2021.

[137] Bruce A. Campbell, Nemanja Kaloper, and Keith A. Olive. Classical hair for Kerr-Newman black holes in string gravity. *Phys. Lett. B*, 285:199–205, 1992.

[138] Zong-Kuan Guo, Nobuyoshi Ohta, and Takashi Torii. Black Holes in the Dilatonic Einstein-Gauss-Bonnet Theory in Various Dimensions. I. Asymptotically Flat Black Holes. *Prog. Theor. Phys.*, 120:581–607, 2008.

[139] Mehdi Saravani and Thomas P. Sotiriou. Classification of shift-symmetric Horndeski theories and hairy black holes. *Phys. Rev. D*, 99(12):124004, 2019.

[140] Abhishek Hegade K. R., Elias R. Most, Jorge Noronha, Helvi Witek, and Nicolas Yunes. How do spherical black holes grow monopole hair? *Phys. Rev. D*, 105(6):064041, 2022.

[141] Shahar Hod. Spin-induced black hole spontaneous scalarization: Analytic treatment in the large-coupling regime. *Phys. Rev. D*, 105(2):024074, 2022.

[142] Hector O. Silva, Caio F. B. Macedo, Emanuele Berti, and Luís C. B. Crispino. Slowly rotating anisotropic neutron stars in general relativity and scalar–tensor theory. *Class. Quant. Grav.*, 32:145008, 2015.

[143] Christian Cherubini, Donato Bini, Salvatore Capozziello, and Remo Ruffini. Second order scalar invariants of the Riemann tensor: Applications to black hole space-times. *Int. J. Mod. Phys. D*, 11:827–841, 2002.

[144] Jose Luis Blázquez-Salcedo, Daniela D. Doneva, Jutta Kunz, and Stoytcho S. Yazadjiev. Radial perturbations of the scalarized Einstein-Gauss-Bonnet black holes. *Phys. Rev. D*, 98(8):084011, 2018.

[145] Masato Minamitsuji and Taishi Ikeda. Scalarized black holes in the presence of the coupling to Gauss-Bonnet gravity. *Phys. Rev. D*, 99(4):044017, 2019.

[146] Hector O. Silva, Caio F.B. Macedo, Thomas P. Sotiriou, Leonardo Gualtieri, Jeremy Sakstein, and Emanuele Berti. Stability of scalarized black hole solutions in scalar-Gauss-Bonnet gravity. *Phys. Rev. D*, 99(6):064011, 2019.

[147] Georgios Antoniou, Antoine Lehébel, Giulia Ventagli, and Thomas P. Sotiriou. Black hole scalarization with Gauss-Bonnet and Ricci scalar couplings. *Phys. Rev. D*, 104(4):044002, 2021.

[148] Georgios Antoniou, Caio F. B. Macedo, Ryan McManus, and Thomas P. Sotiriou. Stable spontaneously-scalarized black holes in generalized scalar-tensor theories, 4 2022.

[149] Helvi Witek, Miguel Zilhao, Gabriele Bozzola, Matthew Elley, Giuseppe Ficarra, Taishi Ikeda, Nicolas Sanchis-Gual, and Hector Silva. Canuda: a public numerical relativity library to probe fundamental physics, October 2021.

[150] Hirotada Okawa, Helvi Witek, and Vitor Cardoso. Black holes and fundamental fields in Numerical Relativity: initial data construction and evolution of bound states. *Phys. Rev. D*, 89(10):104032, 2014.

[151] Miguel Zilhão, Helvi Witek, and Vitor Cardoso. Nonlinear interactions between black holes and Proca fields. *Class. Quant. Grav.*, 32:234003, 2015.

[152] Steven R. Brandt, Gabriele Bozzola, Cheng-Hsin Cheng, Peter Diener, Alexandru Dima, William E. Gabella, Miguel Gracia-Linares, Roland Haas, Yosef Zlochower, Miguel Alcubierre, Daniela Alic, Gabrielle Allen, Marcus Ansorg, Maria Babiuc-Hamilton, Luca Baiotti, Werner Benger, Eloisa Bentivegna, Sebastiano Bernuzzi, Tanja Bode, Brockton Brendal, Bernd Bruegmann, Manuela Campanelli, Federico Cipolletta, Giovanni Corvino, Samuel Cupp, Roberto De Pietri, Harry Dimmelmeier,

Rion Dooley, Nils Dorband, Matthew Elley, Yaakoub El Khamra, Zachariah Etienne, Joshua Faber, Toni Font, Joachim Frieben, Bruno Giacomazzo, Tom Goodale, Carsten Gundlach, Ian Hawke, Scott Hawley, Ian Hinder, E. A. Huerta, Sascha Husa, Sai Iyer, Daniel Johnson, Abhishek V. Joshi, Wolfgang Kastaun, Thorsten Kellermann, Andrew Knapp, Michael Koppitz, Pablo Laguna, Gerd Lanferman, Frank Löffler, Joan Masso, Lars Menger, Andre Merzky, Jonah Maxwell Miller, Mark Miller, Philipp Moesta, Pedro Montero, Bruno Mundim, Andrea Nerozzi, Scott C. Noble, Christian Ott, Ravi Paruchuri, Denis Pollney, David Radice, Thomas Radke, Christian Reisswig, Luciano Rezzolla, David Rideout, Matei Ripeanu, Lorenzo Sala, Jascha A Schewtschenko, Erik Schnetter, Bernard Schutz, Ed Seidel, Eric Seidel, John Shalf, Ken Sible, Ulrich Sperhake, Nikolaos Stergioulas, Wai-Mo Suen, Bela Szilagyi, Ryoji Takahashi, Michael Thomas, Jonathan Thornburg, Malcolm Tobias, Aaryn Tonita, Paul Walker, Mew-Bing Wan, Barry Wardell, Leonardo Werneck, Helvi Witek, Miguel Zilhão, and Burkhard Zink. The Einstein Toolkit, December 2021. To find out more, visit `http://einsteintoolkit.org`.

[153] Miguel Zilhão and Frank Löffler. An Introduction to the Einstein Toolkit. *Int. J. Mod. Phys. A*, 28:1340014, 2013.

[154] Tom Goodale, Gabrielle Allen, Gerd Lanfermann, Joan Massó, Thomas Radke, Edward Seidel, and John Shalf. The Cactus framework and toolkit: Design and applications. In *Vector and Parallel Processing – VECPAR'2002, 5th International Conference, Lecture Notes in Computer Science*, Berlin, 2003. Springer.

[155] Cactus Computational Toolkit.

[156] Carpet: Adaptive Mesh Refinement for the Cactus Framework.

[157] Marcus Ansorg, Bernd Brügmann, and Wolfgang Tichy. A Single-domain spectral method for black hole puncture data. *Phys. Rev. D*, 70:064011, 2004.

[158] Ulrich Sperhake. Binary black-hole evolutions of excision and puncture data. *Phys. Rev. D*, 76:104015, 2007.

[159] Olaf Dreyer, Badri Krishnan, Deirdre Shoemaker, and Erik Schnetter. Introduction to isolated horizons in numerical relativity. *Phys. Rev. D*, 67:024018, 2003.

[160] Jonathan Thornburg. Finding apparent horizons in numerical relativity. *Phys. Rev. D*, 54:4899–4918, 1996.

[161] Jonathan Thornburg. A Fast apparent horizon finder for three-dimensional Cartesian grids in numerical relativity. *Class. Quant. Grav.*, 21:743–766, 2004.

[162] Yakov Shlapentokh-Rothman. Exponentially growing finite energy solutions for the Klein-Gordon equation on sub-extremal Kerr spacetimes. *Commun. Math. Phys.*, 329:859–891, 2014.

[163] Richard Brito, Vitor Cardoso, and Paolo Pani. Superradiance: New Frontiers in Black Hole Physics. *Lect. Notes Phys.*, 906:pp.1–237, 2015.

[164] Georgios Moschidis. Superradiant instabilities for short-range non-negative potentials on Kerr spacetimes and applications, 8 2016.

[165] Sam R. Dolan. Instability of the massive Klein-Gordon field on the Kerr spacetime. *Phys. Rev. D*, 76:084001, 2007.

[166] Sam R. Dolan. Superradiant instabilities of rotating black holes in the time domain. *Phys. Rev. D*, 87(12):124026, 2013.

[167] Emanuele Berti, Vitor Cardoso, and Andrei O. Starinets. Quasinormal modes of black holes and black branes. *Class. Quant. Grav.*, 26:163001, 2009.

[168] Zack Carson, Brian C. Seymour, and Kent Yagi. Future prospects for probing scalar–tensor theories with gravitational waves from mixed binaries. *Class. Quant. Grav.*, 37(6):065008, 2020.

[169] Scott E. Perkins, Nicolás Yunes, and Emanuele Berti. Probing Fundamental Physics with Gravitational Waves: The Next Generation. 10 2020.

[170] Nicolas Yunes and Frans Pretorius. Fundamental Theoretical Bias in Gravitational Wave Astrophysics and the Parameterized Post-Einsteinian Framework. *Phys. Rev. D*, 80:122003, 2009.

[171] Neil Cornish, Laura Sampson, Nicolas Yunes, and Frans Pretorius. Gravitational Wave Tests of General Relativity with the Parameterized Post-Einsteinian Framework. *Phys. Rev. D*, 84:062003, 2011.

[172] Sharaban Tahura and Kent Yagi. Parameterized Post-Einsteinian Gravitational Waveforms in Various Modified Theories of Gravity. *Phys. Rev. D*, 98(8):084042, 2018. [Erratum: Phys.Rev.D 101, 109902 (2020)].

[173] Scott Perkins and Nicolas Yunes. Are Parametrized Tests of General Relativity with Gravitational Waves Robust to Unknown Higher Post-Newtonian Order Effects?, 1 2022.

[174] R. Abbott et al. GW190814: Gravitational Waves from the Coalescence of a 23 Solar Mass Black Hole with a 2.6 Solar Mass Compact Object. *Astrophys. J. Lett.*, 896(2):L44, 2020.

[175] Daniel Baumann. *Cosmology*. Cambridge University Press, 7 2022.

[176] Andrei D. Linde. Inflationary Cosmology. *Lect. Notes Phys.*, 738:1–54, 2008.

[177] Damien A. Easson and Ruth Gregory. Circumventing the eta problem. *Phys. Rev. D*, 80:083518, 2009.

[178] Jerome Martin and Robert H. Brandenberger. The TransPlanckian problem of inflationary cosmology. *Phys. Rev. D*, 63:123501, 2001.

[179] Robert H. Brandenberger and Jerome Martin. The Robustness of inflation to changes in superPlanck scale physics. *Mod. Phys. Lett. A*, 16:999–1006, 2001.

[180] Alek Bedroya and Cumrun Vafa. Trans-Planckian Censorship and the Swampland. *JHEP*, 09:123, 2020.

[181] Alan H. Guth. The Inflationary Universe: A Possible Solution to the Horizon and Flatness Problems. *Phys. Rev.*, D23:347–356, 1981.

[182] Alexei A. Starobinsky. A New Type of Isotropic Cosmological Models Without Singularity. *Phys. Lett.*, B91:99–102, 1980.

[183] Andrei D. Linde. A New Inflationary Universe Scenario: A Possible Solution of the Horizon, Flatness, Homogeneity, Isotropy and Primordial Monopole Problems. *Phys. Lett.*, B108:389–393, 1982.

[184] Andreas Albrecht and Paul J. Steinhardt. Cosmology for Grand Unified Theories with Radiatively Induced Symmetry Breaking. *Phys. Rev. Lett.*, 48:1220–1223, 1982.

[185] Andrei D. Linde. Chaotic Inflation. *Phys. Lett.*, B129:177–181, 1983.

[186] Y. Akrami et al. Planck 2018 results. X. Constraints on inflation. 2018.

[187] Andrei D. Linde. The Inflationary Universe. *Rept. Prog. Phys.*, 47:925–986, 1984.

[188] Andrei D. Linde. INITIAL CONDITIONS FOR INFLATION. *Phys. Lett.*, B162:281–286, 1985.

[189] Andrei Linde. Inflationary Cosmology after Planck 2013. In *Proceedings, 100th Les Houches Summer School: Post-Planck Cosmology: Les Houches, France, July 8 - August 2, 2013*, pages 231–316, 2015.

[190] Katy Clough, Eugene A. Lim, Brandon S. DiNunno, Willy Fischler, Raphael Flauger, and Sonia Paban. Robustness of Inflation to Inhomogeneous Initial Conditions. 2016.

[191] Katy Clough, Raphael Flauger, and Eugene A. Lim. Robustness of Inflation to Large Tensor Perturbations. *JCAP*, 1805(05):065, 2018.

[192] Josu C. Aurrekoetxea, Katy Clough, Raphael Flauger, and Eugene A. Lim. The Effects of Potential Shape on Inhomogeneous Inflation. *JCAP*, 05:030, 2020.

[193] Maxence Corman and William E. East. Starting inflation from inhomogeneous initial conditions with momentum. 12 2022.

[194] Y. Akrami et al. Planck 2018 results. X. Constraints on inflation. *Astron. Astrophys.*, 641:A10, 2020.

[195] P. A. R. Ade et al. Improved Constraints on Primordial Gravitational Waves using Planck, WMAP, and BICEP/Keck Observations through the 2018 Observing Season. *Phys. Rev. Lett.*, 127(15):151301, 2021.

[196] William E. East, Matthew Kleban, Andrei Linde, and Leonardo Senatore. Beginning inflation in an inhomogeneous universe. *JCAP*, 1609(09):010, 2016.

[197] Cristian Joana and Sébastien Clesse. Inhomogeneous preinflation across Hubble scales in full general relativity. *Phys. Rev. D*, 103(8):083501, 2021.

[198] Renata Kallosh and Andrei Linde. Universality Class in Conformal Inflation. *JCAP*, 1307:002, 2013.

[199] Renata Kallosh, Andrei Linde, and Diederik Roest. Superconformal Inflationary α-Attractors. *JHEP*, 11:198, 2013.

[200] Tomas Andrade et al. GRChombo: An adaptable numerical relativity code for fundamental physics. *J. Open Source Softw.*, 6(68):3703, 2021.

[201] Josu C. Aurrekoetxea, Katy Clough, and Eugene A. Lim. CTTK: a new method to solve the initial data constraints in numerical relativity. *Class. Quant. Grav.*, 40(7):075003, 2023.

[202] Masaru Shibata and Takashi Nakamura. Evolution of three-dimensional gravitational waves: Harmonic slicing case. *Phys. Rev. D*, 52:5428–5444, Nov 1995.

[203] David Garfinkle, Anna Ijjas, and Paul J. Steinhardt. Initial conditions problem in cosmological inflation revisited. *Phys. Lett. B*, 843:138028, 2023.

[204] Llibert Aresté Saló, Katy Clough, and Pau Figueras. Well-Posedness of the Four-Derivative Scalar-Tensor Theory of Gravity in Singularity Avoiding Coordinates. *Phys. Rev. Lett.*, 129(26):261104, 2022.